Growth and Structure of Complex Oxide Thin Films

Promotion Committee

Chairman and secretary	
prof. dr. M.J. Peters	University of Twente
Promotor	
prof. dr. H. Rogalla	University of Twente
Assistant promotors	
dr. ir. H. Graafsma	European Synchrotron Radiation Facility, France
dr. S. Harkema	University of Twente
Members	
prof. dr. ing. D.H.A. Blank	University of Twente
prof. dr. T.T.M. Palstra	University of Groningen
prof. dr. I.K. Robinson	University College London
prof. dr. J.F. van der Veen	Paul Scherrer Institute, Switzerland
prof. dr. E. Vlieg	Radboud University Nijmegen
prof. dr. ir. H.J.W. Zandvliet	University of Twente

The work described in this thesis was performed in a collaboration between the European Synchrotron Radiation Facility in Grenoble, France and the Low Temperature Division of the University of Twente in Enschede, The Netherlands. The research was partially supported by the Netherlands Organization for Scientific Research (NWO).

ISBN 9036523834

GROWTH AND STRUCTURE OF COMPLEX OXIDE THIN FILMS

PROEFSCHRIFT

ter verkrijging van
de graad van doctor aan de Universiteit Twente,
op gezag van de rector magnificus,
prof. dr. W. H. M. Zijm,
volgens besluit van het College voor Promoties
in het openbaar te verdedigen
op woensdag 7 juni 2006 om 15.00 uur

door

Vedran Vonk

geboren op 14 juli 1976
te Koper (Slovenië)

Dit proefschrift is goedgekeurd door de promotor:

prof. dr. H. Rogalla

en de assistent-promotoren:

dr. ir. H. Graafsma
dr. S. Harkema

Contents

Chapter 1

General Introduction

1.1 Motivation

Complex transition metal oxides are an important class of materials due to the wealth of physical properties they comprise. These compounds can show itinerant and local ferromagnetism, magnetoresistance, ferroelectricity, semi-conductivity, half-metallic magnetism, non-conductivity and superconductivity, making them very interesting for technological applications, like thin film electronics [1]. With the advance of nano-scale engineering, the need arises to understand and control thin film growth at the atomic level [2], which at the same time emphasizes the importance of a fundamental understanding of the influence of surfaces and interfaces on physical properties of materials [3]. At present it is possible to heteroepitaxially deposit atomically flat single unit cell layers. For the complex transition metal oxides, often Pulsed Laser Deposition is the growth technique [4], because it can be used with the appropriate thermodynamic growth parameters. Growth control has two aspects: obtaining the wanted phase, or more particular the wanted atomic (interface) stacking and control over the morphology. The first aspect is mainly a question of chemistry and is concerned with control over the atomic termination of the substrate surface and thermodynamic parameters during growth. The second aspect concerns controlling the kinetics during deposition enabling to grow atomically flat unit cell layers. The growth dynamics during PLD have been extensively studied using Reflection High Energy Electron Diffraction (RHEED) [5], even at high background pressure [6]. Due to the strong interaction of the electrons with the crystal, mainly information about the surface morphology can be extracted with RHEED. Structural information of the grown films is mainly obtained ex situ in a sort of archaeological way, and often not

at deposition conditions, which may have a large influence on the atomic and micro structure. Obtaining information on the atomic and micro structure during growth requires another technique and for this purpose in situ Surface X-ray Diffraction is suited. By use of X-rays, the quantitative interpretation of the scattering patterns is much facilitated compared with electrons, because the so-called kinematical scattering approximation is valid. The less interacting X-rays penetrate more into the material, enabling to follow the structure evolution of the complete film during growth. At the same time, also with X-rays the surface roughness can be probed, which allows to follow the dynamics. It was not until recently, that the very first in situ surface sensitive X-ray diffraction measurements during PLD were reported [7, 8, 9].

Once the growth is controlled, the physical properties of the thin films may be improved. Often the transition metal oxides show very complex phase diagrams. As a function of a thermodynamic variable or the composition, particularly the oxygen content, the properties may change drastically. An example is given by the High-T_c superconductors [10, 11, 12], that lose their electrical resistance completely upon cooling through the critical transition temperature but that can become metallic or even insulating by changing their oxygen content. Understanding the underlying physical processes responsible for these properties is very important for manipulation and application in real devices of these materials. One pathway to achieve this goal, is to study the crystal structure, because in general this is closely related to the physical properties. In many cases, a change in properties of a particular compound is accompanied by a structural phase transition. By studying the structure of the complex oxides, insight may be gained in the fundamental physics involved. The nature of the atomic bonds is of crucial importance[13, 14]: electronic properties are determined by the electronic configuration [15] and for instance ferro-electricity manifests itself by atomic displacements within the crystal lattice, resulting in a polarization [16].

1.2 Perovskites

Named after the Russian mineralogist count Perovski, the mineral $CaTiO_3$ gave the name to the whole structural family of the perovskites, having the general structural formula ABO_3. Closely related to the perovskites are the spinel family (AB_2O_4) and the corundum family (A_2O_3), both of which are the trivial names of the minerals

$MgAl_2O_4$ and Al_2O_3 respectively. Another oxide family is formed by the Rudlesden-Popper phases [17]. The general structure $A_{n+1}B_nO_{3n+1}$ with $n = 0, 1, 2..$, becomes equivalent to the perovskite structure for $n \to \infty$. For finite values of n, the Ruddlesden-Popper phases can be seen as a stacking of ABO_3 layers, seperated by a "stacking fault" AO-AO every n layers [1]. In the following paragraphs, the structure of bulk perovskites will be discussed in more detail, after which the structure of thin film perovskites will be discussed.

1.2.1 Bulk materials

The structure of the perovskites can be seen as a network of corner-sharing oxygen octahedra, which surround the B-cations. The cavities formed in between the octahedra leave space for the A-cations. The upper left part of figure 1.1 shows the ideal, cubic crystal structure. Two common distortions from the ideal structure, elongation and tilting of the oxygen octahedra, are shown in the lower left and lower right parts of fig 1.1 respectively. Elongation of the oxygen octahedra along one of its tetrad axes, for example by the Jahn-Teller effect [18], results in a tetragonal structure. Tilting of the oxygen octahedra about one (or more) of its tetrad axes, can result in tetragonal, orthorhombic or hexagonal structures. The right hand side of figure 1.1 shows the projections along one of the principal axes of a perovskite structure in the undistorted (top) and tilted (bottom) case. For the perfect, cubic structure (top) the oxygen octahedra fall on top of each other. For the particular tilt-system shown here, two neighbouring octahedra rotate by the same angle from the undistorted position, only in opposite directions. This particular configuration, consisting of strings of oxygen octahedra tilting alternately clock- and anti-clockwise, results in a tetragonal structure. A more complete overview of phase transitions in perovskite crystallography based on group-theory is given by Howard and Stokes[19].

The resulting crystal system of any perovskite, will depend of course on which elements occupy the A and B sites in the lattice. A simplified but comprehensive manner to describe the atomic stacking and resulting crystal structure, is by considering the ionic radii of the elements involved. For instance, would the atom inserted

[1] By "stacking fault" the following is understood. Consider an infinite stack of unit cell layers ABO_3, which is cut along one of its principal axes and subsequently one part is displaced by the vector $(\frac{1}{2}, \frac{1}{2}, \frac{1}{2})$ with respect to the other. This leaves two crystals, one terminated by an AO layer and the other by BO_2. The stacking fault is now formed by placing an additional AO layer in the gap in such a way that on the BO_2-terminated side the stacking is again like in the bulk.

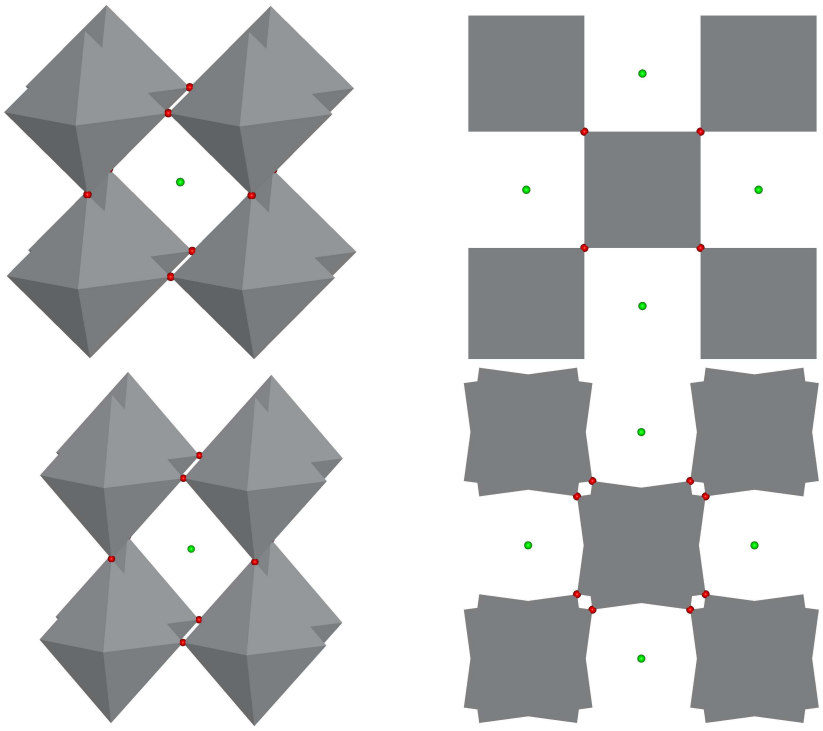

Figure 1.1: The perovskite crystal structure, drawn as a network of oxygen octahedra that surround the B-cation, and the cavities that leave space for the A-cation. Shown are the ideal cubic structure (top left), and the projection along a principal axis (top right). Two common distortions from the cubic structure, elongation and tilting of the octahedra as described in the text, are shown on the bottom left (3D view) and right (projection), respectively.

in the A-site of a certain structure be too small for the pocket, the oxygen octahedra surrounding the B-site will tilt in order to reduce some of the inter-atomic distances [20].

1.2.2 Thin Films

The structure of thin epitaxial films differs in general from the bulk, which can influence their physical properties. First of all, in one dimension the crystal size is reduced, sometimes down to only a few unit cell layers. In general this results in the physical properties manifesting themselves 2-dimensionally. For instance a fundamental issue like how small a ferro-electric domain can be before losing its properties

[21], can be addressed. This issue is of extreme importance with the recent advancements in nanotechnology. Second, strain that is introduced in the film by the lattice mismatch with the substrate can have drastic effects on the properties, not necessarily degrading them. For example, for superconductors it is well known that the transition temperature can be increased by applying hydrostatic pressure [22]. For thin films this would mean that by proper choice of the substrate, the film can be strained compressively, thereby increasing T_c. A doubling of T_c compared with the bulk value has been found for $La_{1.9}Sr_{0.1}CuO_4$ on $SrLaO_4$ substrates [23]. Third, thin films contain in general many defects, like dislocations, ionic disorder and surface roughness. From materials science it is well-known that the microstructure has a large influence on the physical properties. All the aformentioned effects will manifest themselves simultaneously in thin films, making it a very challenging task to improve or tailor the physical properties of thin films for applications. Again, detailed knowledge of the crystal structure of thin films is very important for understanding their properties.

By application of complex oxides in thin film technology, several of the abovementioned aspects come into play. One can alter the composition by fabrication of so-called artificial lattices [24], which consist of layers of different materials, each with a thickness in the order of a few unit cells. Recent developments in superlattices, have shown that physical properties may be significantly different, e.g enhancement of ferroelectricity [25, 26] or interface conductivity from individually isolating compounds [27]. From both examples it becomes obvious that it is extremely important for interface and interfacial strain engineering to not only control the composition, but also the morphology, in order to obtain well-defined layers. Another aspect is strain which may be introduced, which is equivalent with changing the thermodynamic pressure. Again, for application in real devices optimal properties are pursued. From a fundamental point of view, the resulting properties of complex oxide thin films are very interesting.

1.3 Growth of complex oxide thin films

As mentioned in the previous paragraph, it is indispensible to have a very accurate control of thin film growth of the complex oxides. Several aspects play an important role in thin film growth and determine the boundary conditions for high quality films.

First of all, the thermodynamic deposition conditions are fixed by the chemistry of phase-formation and chemical stability of the particular compound. Thin film growth takes usually place at high temperatures, because then the kinetics, which often govern the growth, are enhanced. As mentioned before, complex oxides have in general a very rich phase-diagram, which sometimes makes it a meticulous task optimizing the deposition conditions. Second, the growth mode of the particlar system determines to a great extent the morphology of the grown films, which has to be controlled very accurately, especially for mulilayer systems. Third, the microstructure of the resulting film is not only dependent on the growth mode but also on the handling of the sample after deposition, i.e. during cool-down to room temperature. Again, by cooling down special care has to be taken in order to arrive at the desired point in the sometimes complicated phase-diagrams.

1.3.1 Pulsed Laser Deposition

In Pulsed Laser Deposition (PLD) [4], a high intensity laser with an appropriate wavelength is used to create off a target material a plasma, through which the particle transfer to a heated substrate is established. The reason for using a pulsed laser is two-fold. First of all, due to the short laser pulses, the plasma can be formed. The plasma consists of charged clusters [28] with a high kinetic energy, which in turn allows to maintain a relatively high background pressure in the chamber. Especially for the growth of complex oxides, it is important to deposit in an oxygen environment up to 1 mbar, in order to obtain the desired phase of the films. Second, the particles do not arrive continuously at the substrate, which allows the freshly deposited material to relax in between the pulses. This is important, because due to the extreme supersaturation in the plasma, the nucleation rate is high during the time that the plasma is present. In between the laser pulses, the growth is then governed by kinetics. This last aspect makes PLD rather different from conventional Molecular Beam Epitaxy (MBE) techniques, resulting in a different morphology during growth [29, 30, 31, 32]. It has been found that for certain systems, the surfaces of PLD-grown films are much smoother than when using more traditional forms of MBE, like evaporation [33].

1.3.2 Growth Modes

The morphology of thin films during growth will depend on several factors, especially on the substrate temperature. In a simplified way, three different growth modes as function of temperature can be distinguished, which will be discussed hereafter. Recently deposited ad-atoms or clusters, will diffuse over the surface, i.e. they hop from lattice site to lattice site if their thermal energy is large enough to overcome the diffusion energy barrier. Nucleation will take place when either the thermal energy is not sufficient anymore to hop from site to site, when they collide with other diffusing species[2] or at surface defects, which introduce an additional energy barrier. Well-known is the so-called Ehrlich-Schwöbel barrier [34, 35] which introduces an additional diffusion barrier at step edges. This can be understood by considering the co-ordination difference at the lower and upper step edge: more bonds are formed at the lower step edge. With most of the defects on a surface consisting of steps, a distinction between three growth modes can be made. At high enough temperatures, the diffusion length of the ad-atoms or clusters is larger than the average distance between steps. Therefore, nucleation will only take place at step edges, resulting in so-called step flow. Since all the terraces evolve in the same manner, the morphology of the surface does not really change, it appears as if only the step edges flow, but the average terrace widths and heights do not change. At intermediate temperatures, the diffusion length of the species is not larger than the average terrace width, and therefore nucleation will take place *on* the terraces, thereby forming islands. The diffusion length is however large enough, for new ad-atoms or clusters arriving on top of the previously formed islands to reach their edges. Therefore, there is no so-called second layer nucleation and the growth proceeds by the island becoming larger untill neighbourhing islands coalesce and a complete unit cell high layer is grown before the next layer starts to nucleate. Hence the name layer-by-layer growth. Finally, at very low temperatures, the diffusion length is so small that second layer (and third and fourth and so on) nucleation does occur, resulting in island formation. This type is called 3D island or Poisson growth. Schematically, all the three aformentioned growth modes are shown in figure 1.2.

In a real system, a combination of the three growth modes is possible. For example, in heteroepitaxial growth, the in-plane lattice parameters of film and substrate

[2]Collision with other diffusing species can lead to the formation of a cluster, having a larger mass and therefore a larger chance of nucleating.

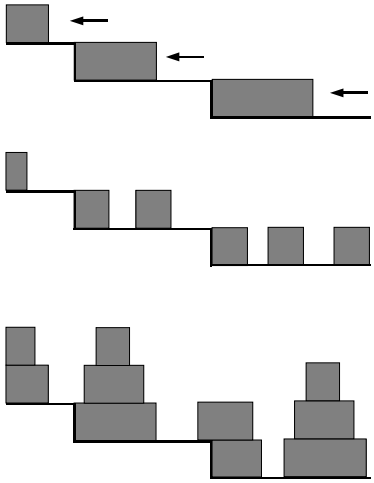

Figure 1.2: Schematic representation of a stepped surface and the morphology of the added layer (grey) for the three growth modes: stepflow (top), layer-by-layer (middle) and 3D-island growth (bottom). The arrows indicate the direction in which the added material moves until reaching a step edge to nucleate. The step edges seem to flow in the direction opposite of the arrows. From the 3D-island growth picture (bottom) where three layers are forming simultaneously, the term multilayer growth becomes clear.

will not be the same, resulting in a strained film. The strain energy will increase with increasing film thickness, and at a certain moment it will become favorable to introduce defects in the film. These defects can be either dislocations, twin domains, surface roughness or a combination of them and will finally result in the formation of islands and subsequently island growth. This type of growth which first proceeds in a layer-by-layer fashion and at a certain thickness changes to island formation is often called Stranski-Krastanov growth [36]. Furthermore, there will in general not be a distinct seperation between the different growth modes as a function of temperature. First of all, ideal layer-by-layer growth will not occur, because it is note very likely that a layer will be completely formed, before second layer nucleation occurs. With increasing coverage, the distance between the islands decreases until they coalesce, thereby increasing the distance to the next nucleation site, which can be now seen as a 'hole' in the surface. This explains why second layer nucleation always occurs before

completion of the underlying layer. Another example illustrating that real systems do not always behave strictly according to the aforementioned growth modes is that of re-entrant layer-by-layer growth. For some systems it was observed that after an initial transition from layer-by-layer to island growth, upon lowering the temperature even more, the growth changed to layer-by-layer again [37]. The explanation was found to be in the shape of the step-ledges; at a straight ledge the energy barrier to descend is larger than at a kink. Lowering the temperature results for certain systems in the step ledges to become more dendritic, thereby lowering the energy barrier for diffusion.

Lowering the Ehrlich-Schwöbel barrier by adding so-called surfactants, can lead to layer-by-layer growth at much lower temperatures as well. This method has been applied successfully to the homoepitaxial growth of Ag by adding Sb [38] and has been explored further for other metals [39]. For the complex oxides discussed here, so far no successful surfactant has been found. However, in the case of Pt growth, it was found that an important role for the enhancement of the interlayer mass transport was played by oxygen [40], which is the common background gas in PLD.

Non-destructive in situ monitoring the growth process is performed mainly using diffraction techniques. Since these techniques are sensitive to the surface roughness, the layer-by-layer growth regime, manifesting itself as an alternating smooth and rough surface during the deposition, is ideal for controlling the thickness. For any probe, i.e. electrons, ions or photons, the scattered intensity of surface sensitive reflections will decrease compared to scattering from the same smooth surface. Therefore, layer-by-layer growth results in so-called intensity growth oscillations (see chapter 2), which are extremely useful for an accurate film thickness control, which in turn is essential for e.g. multilayer fabrication. Due to the special circumstances during the PLD process, which result in a high nucleation rate compared with other deposition techniques, layer-by-layer growth is enhanced in the case of growth of complex oxide thin films.

1.4 Outline

In the remainder of this thesis the following is described. Chapter 2 gives an overview of some aspects of X-ray diffraction, and in particular the difference between using electrons and X-rays to study epitaxial thin film growth. The description of sur-

face X-ray diffraction in the same chapter, illustrates the boundary conditions for experimental access to this technique. Next, in chapter 3, a study on the atomic surface structure of the widely used substrate material $SrTiO_3(001)$ is presented. There the results of a SXRD study are presented and discussed in view of previously reported literature models. Chapter 4 describes the design of the PLD chamber which was used for the in situ growth studies. The results of in situ PLD growth studies of $YBa_2Cu_3O_{7-x}$ (YBCO) are presented in Chapter 5, after which the structure of YBCO thin films at high temperatures and as a function of film thickness are presented in chapters 6 and 7, respectively. Finally, a study on the high temperature interface structure of $SrTiO_3/LaAlO_3$ is presented in chapter 8.

References

[1] S. B. Ogale (Ed.), *Thin Films and Heterostructures for Oxide Electronics*, Springer Science + Business Media, New York, 2005.

[2] J. V. Barth, G. Costantini, K. Kern, Nature **437** (2005) 671–679.

[3] D. L. Allara, Nature **437** (2005) 638–639.

[4] D. B. Chrisey, G. K. Hubler (Eds.), *Pulsed Laser Deposition of Thin Films*, John Wiley and Sons, New York, 1994.

[5] H. Karl, B. Stritzker, Phys. Rev. Lett. **69** (1992) 2939.

[6] A. J. H. M. Rijnders, G. Koster, D. H. A. Blank, H. Rogalla, Appl. Phys. Lett. **70** (1997) 1888.

[7] G. Eres, J. Z. Tischler, M. Yoon, B. C. Larson, C. M. Rouleau, D. H. Lowndes, P. Zschack, Appl. Phys. Lett. **80** (2002) 3379.

[8] A. Fleet, D. Dale, Y. Suzuki, J. D. Brock, Phys. Rev. Lett. **94** (2002) 036102.

[9] H. H. Wang, A. Fleet, J. D. Brock, D. Dale, Y. Suzuki, J. Appl. Phys **96** (2004) 5324–5328.

[10] J. G. Bednorz, K. A. Müller, Rev. Mod. Phys. **60** (1988) 585–600.

[11] R. J. Cava, J. Am. Ceram. Soc. **83** (2000) 5–28.

[12] K. Yvon, M. François, Z. Phys. B **76** (1989) 413–444.

[13] J. B. Goodenough, *Magnetism and Chemical Bond*, Interscience, New York, 1963.

[14] D. I. Khomskii, G. A. Sawatzky, Solid State Comm. **102** (1997) 87–99.

[15] M. Imada, A. Fujimoro, Y. Tokura, Rev. Mod. Phys. **70** (1998) 1039–1263.

[16] F. Jona, G. Shirane, *Ferroelectric Crystals*, Dover Publicatitions, New York, 1993.

[17] S. N. Ruddlesden, P. Popper, Acta Cryst. **10** (1957) 538; Acta Cryst. **11** (1958) 54.

[18] H. A. Jahn, E. Teller, Proc. R. Soc. London Sect. A **276** (1937) 238.

[19] C. J. Howard, H. T. Stokes, Acta Crystallogr. A **61** (2005) 93.

[20] H. D. Megaw, *Crystal Structures: A Working Approach*, W.B. Saunders Company, Philadelphia, 1973.

[21] D. D. Fong, G. B. Stephenson, S. K. Streiffer, J. A. Eastman, O. Auciello, P. H. Fuoss, C. Thompson, Science **304** (2004) 1650; C. Lichtensteiger, J.-M. Triscone, J. Junquera, P. Ghosez, Phys. Rev.Lett. **94** (2005) 047603; N. Sai, A. M. Kolpak, A. M. Rappe, Phys. Rev. **B72** (2005) 020101.

[22] R. Wijngaarden, R. Griessen, *Studies of High Temperature Superconductors*, Nova Science, New York, 1989.

[23] J.-P. Locquet, J. Perret, J. Fompeyrine, E. Mächler, J. W. Seo, G. van Tendeloo, Nature **394** (1998) 453.

[24] G. Koster, *Artificially Layered Oxides by Pulsed Laser Deposition*, Ph.D. thesis, University of Twente (1999).

[25] H. N. Lee, H. M. Christen, M. F. Chisholm, C. M. Rouleau, D. H. Lowndes, Nature **433** (2005) 395–399.

[26] G. Rijnders, D. H. A. Blank, Nature **433** (2005) 369–370.

[27] A. Ohtomo, H. Y. Hwang, Nature **427** (2004) 423–426.

[28] T. Venkatesan, X. D. Wu, A. Inam, Y. Jeon, M. Croft, E. W. Chase, C. C. Chang, J. B. Wachtman, R. W. Odom, R. R. di Brozolo, C. A. Magee, Appl. Phys. Lett. **53** (1988) 1431.

[29] B. Hinnemann, H. Hinrichsen, D. E. Wolf, Phys. Rev. **E67** (2003) 011602.

[30] P.-M. Lam, S. J. Liu, C. H. Woo, Phys. Rev. **B66** (2002) 045408.

[31] B. Hinnemann, H. Hinrichsen, D. E. Wolf, Phys. Rev. Lett. **87** (2001) 135701.

[32] R. D. Narhe, M. D. Khandkar, K. P. Adhi, A. V. Limaye, Phys. Rev. Lett. **86** (2001) 1570.

[33] H. Jenniches, M. Klaua, H. Höche, J. Kirschner, Appl. Phys. Lett. **69** (1996) 3339.

[34] R. L. Schwöbel, E. J. Shipsey, J. Appl. Phys. **37** (1966) 3682.

[35] G. Ehrlich, F. G.Hudda, J. Chem. Phys. **44** (1966) 1030.

[36] I. V. Markov, *Crystal Growth for Beginners*, World Scientific, Singapore, 1994.

[37] R. Kunkel, B. Poelsema, L. K. Verheij, G.Comsa, Phys. Rev. Lett. **65** (1990) 733.

[38] H. A. van der Vegt, H. M. van Pinxteren, M. Lohmeier, E. Vlieg, J. M. C. Thornton, Phys. Rev. Lett. **68** (1992) 3335.

[39] H. A. van der Vegt, *Surfactants in Homoepitaxial Metal Growth*, Ph.D. thesis, University of Amsterdam (1995).

[40] B. Poelsema, R. Kunkel, N. Nagel, A. F. Becker, G. Rosenfeld, G. Comsa, Appl. Phys. A **53** (1991) 369.

Figure 1.3: The X-ray transmission image of the hand of Mrs. Röntgen.

Chapter 2

X-rays for Crystal Growth Studies

2.1 Introduction

Soon after the discovery of X-rays by Wilhelm Conrad Röntgen in 1895 [1], the transmission image of the hand of Mrs. Röntgen, shown in figure 1.3, became famous all over the world. It took several years however, before the true potential of this initial curiosity was fully appreciated. The discovery by Friedrich and Knipping in 1912 [2] that crystals scatter X-rays to form a pattern consisting of regularly placed well defined spots, as proposed by Max von Laue, was the beginning of a new technique to solve the atomic structure of crystals called X-ray diffraction. Later in 1913, H.J.G. Moseley found that, when illuminating metals with X-rays, radiation consisting of wavelengths different from the incident one were emitted. The dependence of emitted X-ray wavelengths on the atomic number of the particular metal, proved chemical selectivity, which forms the basis of X-ray fluorescence analyses. Nowadays X-rays are used in all kinds of fields like medicine, chemistry, physics, astronomy, art and archaeology, to name just a few. The way in which X-rays can be useful for each of these fields depends on the properties of the interactions of X-rays with matter: absorption, refraction and scattering. In general, a distinction between the following techniques is made: imaging, spectroscopy and scattering, each giving a specific kind of information about the structure or composition of the material under investigation. The experiments that are described in this thesis all make use of scattering of X-rays by crystals.

Modern state-of-the-art X-ray diffraction (XRD) measurements are used to determine for instance the electron density in small micron-sized crystalline compounds, the crystal structure of proteins [3], which consist of up to thousands of atoms in the

unit cell or measure the orientation of single grains in metals during deformation [4]. Furthermore, XRD has become an invaluable tool for fast non-destructive analysis of the crystalline structure in any materials science laboratory. In recent years there is a trend towards using X-ray diffraction to follow chemical and/or physical processes while they occur. Insight in these processes is important for industrial applications, but also from a fundamental point of view. An example is given by time-resolved studies of chemical reactions, where at different stages of the reaction a "snapshot" of the structure is taken. In this way, for example, the photosensitivity of the carbon monoxide complex of myoglobin was studied using pulsed Laue diffraction [5]. Since these kind of processes occur on very short timescales (ps-ns), it is obvious that these measurements put severe demands on the X-ray sources used. Synchrotron Radiation (SR) of third generation sources provides brilliant enough and time-modulated X-ray beams that allow these kind of experiments to be carried out.

Also in the field of structure determination of surfaces, X-rays have become an invaluable tool [6]. Besides the fact that the magnetic structure can be addressed, the weak interaction of X-rays with matter, offers unique possibilities compared to other surface sensitive techniques. First of all, use of X-rays does not require Ultra High Vacuum (UHV) conditions, which is commonly the case for other probes like electrons. Second, due to the high penetration depth of X-rays, it is possible to study buried interfaces. And third, since the X-rays interact only weakly with matter, diffracted X-rays will, in general, have been scattered only once by the sample, making a simple quantitative interpretation of the data possible. This, in turn, enables modeling of the surface structure with a very high resolution of the atomic positions. Furthermore, the use of X-rays is non-destructive, unlike in the case for transmission electron microscopy (TEM). All these factors together make Surface X-ray Diffraction (SXRD) a unique tool to study crystal growth, often because of the non-ambient conditions that are required [7]. Another process that can be studied by SXRD is for instance oxidation [8], which is a reaction that also occurs at the surface [9]. The present thesis is concerned with the use of SXRD to study the process of Pulsed Laser Deposition. So far mainly Reflection High Energy Electron Diffraction [10] has been used for this purpose, even at relatively high pressure up to 100 Pa [11], which enables to study the kinetics through the morphology during growth. However, determining the atomic structure from electron diffraction is severely hampered by multiple scattering. Here is where the main advantage from using X-rays becomes clear: the possibility to study the atomic stacking during thin film growth by PLD.

In this chapter scattering of X-rays by crystals is described. By starting from a basic level up to its use for studying epitaxial deposition, the goal is twofold. First of all, the fundamental difference between electron and X-ray diffraction is put forward. This is needed to understand and compare the results obtained in previous RHEED and the present SXRD studies. Second, the introduction of the crystal shape into the basic scattering equations, results directly in the description of surface roughness, its influence on the crystal truncation rods and finally the X-ray intensity growth oscillations. In the following paragraphs some basic concepts and vocabulary are introduced, which are used in later chapters. A more complete description of the topics described here are found in text books in both optics and X-ray physics [12, 13, 14, 15, 16].

2.2 X-ray scattering

When light interacts with matter, three distinct phenomena occur: absorption, refraction and scattering. All these processes can be described by the interaction of the electromagnetic waves with the electrons in the solid, i.e. the electric component of the wave interacts with the charge. In some special cases the nuclei are involved as well in the scattering process (nuclear scattering), or the magnetic interaction has to be taken into account, but all are left out of consideration here. The formal quantum mechanical description, as given by 'Fermi's golden rule' (see e.g. [17]), is an adequate description of both absorption and scattering of photons by electrons. However, a classical and therefore more intuitive description can be used as well, giving basically the same results. Visualizing the electrons as point charges, bound to the atomic nuclei with a certain strength, the problem of absorption and scattering can be solved using classical mechanics. Under the influence of the incoming electromagnetic wave, the electrons will start to oscillate. The direction of polarization of the incoming beam defines the plane of oscillation of the electrons. Far from resonance the electrons in the crystal just follow the incoming wave, either in or out of phase, and will therefore act as point sources of secondary waves, emitted at the same frequency. This describes elastic scattering. Close to resonance, also waves with a frequency different from the incident one will be emitted. Therefore, the intensity of the elastically scattered part decreases: absorption takes place.

The picture of a negatively charged electron that oscillates with respect to a pos-

itively charged nucleus, is just that of the classical dipole. The analogy with a point mass, hanging from a spring in a gravitational field is easily made. However, the nature of the eigenfrequencies and damping in the case of bound electrons is purely quantum-mechanical, and therefore has no classical analogon. Elaborate overviews on the topic of classical scattering can be found elsewhere [18, 19].

2.2.1 Scattering by an electron density

In the previous section, the principle of classical scattering by an electron was described. Here, this will be extended to the scattering of an electron density by application of the formal theory of elastic scattering. Without losing generality, the following descriptions can be used for electrons and X-rays. This is understood by recalling that the mathematical description of electrons and photons is basically identical. The solutions to the electromagnetic wave equation are identical to those of the Schrödinger equation, namely of the plane wave form:

$$\psi = \psi_0 e^{i(\omega t - \mathbf{k}\cdot\mathbf{r})} \tag{2.1}$$

where ψ_0 is the amplitude, ω the frequency, t the time, $\mathbf{k}$ the wave vector and $\mathbf{r}$ the position in space where the wave ψ is evaluated. Though the mathematical waveform is identical for X-rays and electrons, the relationships between wavelength λ and energy E are not. For electromagnetic waves we have:

$$\lambda[\text{Å}] = \frac{1}{\sqrt{\epsilon\mu}}\frac{2\pi}{\omega} = \frac{hc}{E} \approx \frac{12.4}{E[\text{keV}]} \tag{2.2}$$

with ϵ the electric permittivity, μ the magnetic permeability, h Planck's constant and c the speed of light. In case of non-relativistic electrons the relation becomes:

$$\lambda[\text{Å}] = \sqrt{\frac{h^2}{2m_0 E}} \approx \sqrt{\frac{150}{E[\text{eV}]}} \tag{2.3}$$

with h Planck's constant and m_0 the electron rest mass. Besides the relation between wavelength and energy also the interaction with matter is different for electrons and X-rays, which will be discussed later on.

In the case of elastic scattering the following expression for the total wave field is obtained:

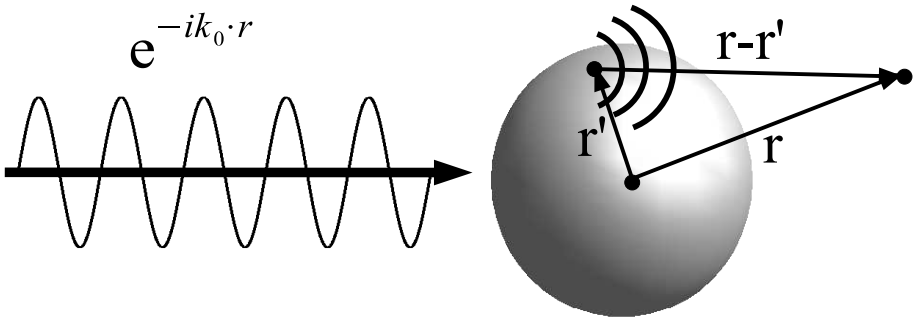

Figure 2.1: Schematic overview of the scattering problem. Due to the incoming plane wave , $e^{-i\mathbf{k_0}\cdot\mathbf{r}}$, a secondary, spherical wave is emitted at point r'. Then as the scattered wave propagates, its amplitude is evaluated at point r. The total scattered wave is obtained by integrating over the whole volume (grey) containing a non-zero scattering potential, which consists of the electron density and possibly the nuclei.

$$\psi(\mathbf{r}) = \psi^{(0)}(\mathbf{r}) + \int G(\mathbf{r},\mathbf{r}')V(\mathbf{r}')\psi(\mathbf{r}')d\mathbf{r}', \tag{2.4}$$

which is the generalized integral form of either the wave or Schrödinger equation [12], with $\psi^{(0)}(\mathbf{r})$ the incoming wave, $G(\mathbf{r},\mathbf{r}')$ the Green's function and $V(\mathbf{r}')$ the scattering potential. In case of X-rays the scattering potential is just the electron density $\rho(\mathbf{r}')$, with which the interaction takes place. For electrons also the nuclei contribute to the scattering potential. In figure 2.1 a schematic view of the problem is illustrated, showing the definitions of $\mathbf{r}$ and $\mathbf{r}'$. The incoming wave ($e^{-i\mathbf{k_0}\cdot\mathbf{r}}$) falls on an object with a non-zero scattering potential and the resulting wave $\psi(\mathbf{r})$, consisting of the incoming and scattered wave, in point $\mathbf{r}$ is regarded. Equation 2.4 basically shows Huygens' principle: each point that is excited by the wave field, acts as a point source in it self, emitting spherical radiation given by the Green's function:

$$G(\mathbf{r},\mathbf{r}') = \frac{e^{-ik|\mathbf{r}-\mathbf{r}'|}}{4\pi|\mathbf{r}-\mathbf{r}'|}. \tag{2.5}$$

The strength with which each point scatters, depends on the scattering potential $V(\mathbf{r}')$, which is different for electrons and X-rays and on the wave field $\psi(\mathbf{r}')$. This last point is rather tricky, because it shows that the scattered wave depends on the scattered wave itself. In other words, if the excited scattering field is very strong,

it can act as a new field, exciting a second and so on. This results in recursive expressions for all the wave fields, and complicates the solution enormeously. If the scattered wave is assumed to be much smaller than the incoming wave, the description becomes much simpler. If only the incoming beam is assumed to excite the individual point scatterers, the term $\psi(\mathbf{r}')$ in eq. 2.4 may be replaced by $\psi^{(0)}(\mathbf{r}') = e^{-i\mathbf{k_0}\cdot\mathbf{r}'}$. This means that the strength of the waves emitted by the individual scatterers depends only on the incoming wave, and the secondary (or higher order) excitation is negligible, i.e. single scattering. This description is called the kinematical or first Born approximation and is valid in the case that the interaction between probe and scatterers is small, as is typically the case for the interaction between X-rays and electrons. Using this approximation together with the assumption that $\mathbf{r} = \mathbf{R} \gg \mathbf{r}'$, the definition $\mathbf{q} = \mathbf{k} - \mathbf{k_0}$, where $\mathbf{k}$ points in the direction of $\mathbf{r} - \mathbf{r}'$, and regarding elastic scattering, that is $|\mathbf{k_0}| = |\mathbf{k}|$, leads to:

$$\psi(\mathbf{r}) = e^{-i\mathbf{k_0}\cdot\mathbf{R}} + \frac{e^{-ik_0R}}{R}\int \rho(\mathbf{r}')e^{i\mathbf{q}\cdot\mathbf{r}'}d\mathbf{r}'. \tag{2.6}$$

The mathematical form of the resulting scattered wave is now very easily interpreted. It consists of the multiplication of the incoming beam with the Fourier transform of the electron density of the object $\Omega(\mathbf{q})$. Equation 2.6 deals with the amplitude of the wave, therefore intensity is obtained by squaring the modulus. Since the term representing the incoming beam is constant throughout an experiment, the scattered intensity results in:

$$I \propto |\Omega(\mathbf{q})|^2. \tag{2.7}$$

This is an important result, because as will be explained in more detail in section 2.3 the function $\Omega(\mathbf{q})$ contains information on the atomic positions within and shape of the scattering object.

2.2.2 Scattering by an atom

As shown in the previous section, the scattering by an object is given by the Fourier transform of its electron density. Picturing the electron density as a collection of individual atoms, is a convenient way for arriving at a description of its scattering, as will be shown in section 2.3. Before dealing with the extension to a whole crystal lattice, here a single atom will be regarded. Using the results of the previous section,

the Fourier transform of the electron density of a single atom can be expressed as:

$$f_a(\mathbf{q}) = \int \rho_a(\mathbf{r}) e^{i\mathbf{q}\cdot\mathbf{r}} d\mathbf{r} \tag{2.8}$$

with f_a the so-called atomic scattering factor, ρ_a the atomic electron density and $\mathbf{r}$ and $\mathbf{q}$ the real and reciprocal space variable respectively. In the case of isolated atoms, that is in absence of chemical bonds, the atomic scattering factor is usually expressed as:

$$f = f_0(\theta) + f'(\omega) + if''(\omega) \tag{2.9}$$

with θ the scattering angle and ω the oscillation frequency of the electrons which is given by the incoming wave. The terms f' and f'' are the dispersion and absorption corrections respectively. At frequencies far from resonance, i.e. far from an absorption edge, $f' \approx f'' \approx 0$ and $f \approx f_0$. Here it is assumed that only f_0 is angle-dependent and f' and f'' are constant as function of scattering angle. One might expect that this is not necessarily true, an example of which is described by James [18], with the mentioning that the effect should be smaller than the experimental error. More recent experiments, described in reference [20], have shown that an angle dependence of f' and f'' is indeed not measurable within the experimental accuracy. For the sake of completeness, it has to be mentioned that small deviations due to anisotropic effects [21], like the influence of polarization of the incoming X-ray beam are also left out of consideration here.

In the absence of chemical bonds, values of the scattering factor are listed for all atoms in the *International Tables* [20], together with values for f' and f'', which can be used as correction factors in case an experiment is carried out near to the absorption edge of a certain atom. Though these scattering factors are given for isolated atoms, they give a very good approximation for most crystallographic measurements, mostly beacuse only the outer electrons participate in chemical bonding. Throughout this thesis, this approximation is used.

2.3 Bulk X-ray Diffraction

In the previous sections it is shown that the scattered X-ray intensity is proportional to the squared modulus of the Fourier transform of the electron density. Here, with

certain assumptions on how the electron density in crystalline materials can be described, this will be used to arrive at an expression for the diffracted intensity by a bulk crystal. The most important aspect of the structure of crystals is *translational symmetry*. A crystal can be thought to consist of periodically placed atoms in three dimensions. The smallest configuration of atoms, that after translation in the three directions **a**, **b** and **c**, by amounts a, b and c, builds the whole crystal lattice throughout space, is the so-called unit cell. This is an important property of the structure, since it implies that the electron density is a function that is periodic in space, with so-called lattice parameters (a, b, c). A convenient expression for the periodic electron density distribution is then given by a sum of convolution integrals:

$$\rho(\mathbf{r}) = \sum_i \rho_{u.c.}(\mathbf{r}) * \delta(\mathbf{r} - \mathbf{r}_i) \tag{2.10}$$

with $\rho_{u.c.}$ the electron density of the unit cell and $\mathbf{r}_i$ the positions of the unit cells throughout space, given in the following notation by:

$$\mathbf{r}_{uvw} = (u\mathbf{a}, v\mathbf{b}, w\mathbf{c}) \tag{2.11}$$

with u, v, w integers and $(\mathbf{a}, \mathbf{b}, \mathbf{c})$ the direct lattice parameters, which define the unit cell. Combining this with equations 2.6 and 2.7, where the Fourier transform of the electron density has to be taken, results in:

$$\Omega(\mathbf{q}) = \sum_u \sum_v \sum_w F(\mathbf{q}) e^{i\mathbf{q}\cdot\mathbf{r}_{uvw}} \tag{2.12}$$

with $F(\mathbf{q})$ the so-called structure factor, the Fourier transform of the electron density of the unit cell. The electron density within the unit cell consists of the contribution by different atoms. Under the assumption that each electron can be attributed to an atom, the structure factor can be expressed as a simple sum over the different atoms by:

$$F(\mathbf{q}) = \sum_j f_j(\mathbf{q}) e^{i\mathbf{q}\cdot\mathbf{r}_j} T_j \tag{2.13}$$

where f_j is the Fourier transform of the electron density of the j-th atom at position $\mathbf{r}_j$, i.e. the atomic scattering factor discussed in section 2.2.2, values of which are listed in the *International Tables* [20]. The term T_j is the so-called temperature

factor of the j-th atom which accounts for intensity changes due to atomic displacements around equilibrium positions like thermal motion. It should be realized that atoms in a lattice are never static, even at T=0 K due to zero-point motion, which is a quantum mechanical consequence. The expression for the structure factor given here represents a time-average, resulting in the atomic positions to be defined as the equilibrium positions around which the atoms vibrate.
Because a crystal structure is homogeneous, the structure factor is the same throughout the crystal volume. Therefore, the sum in equation 2.12 can be written as:

$$\Omega(\mathbf{q}) = F(\mathbf{q}) \sum_{uvw} e^{i\mathbf{q}\mathbf{r}_{uvw}} = F(\mathbf{q})S(\mathbf{q}) \tag{2.14}$$

where $S(\mathbf{q})$ is referred to as the shape function. Because a real crystal does not extend over the whole space, the sum over the exponents is finite, and by using the form of a geometric progression the resulting intensity is written as:

$$I(\mathbf{q}) \propto |F(\mathbf{q})|^2 \frac{\sin^2(N_a\mathbf{q}\cdot\mathbf{a}/2)}{\sin^2(\mathbf{q}\cdot\mathbf{a}/2)} \frac{\sin^2(N_b\mathbf{q}\cdot\mathbf{b}/2)}{\sin^2(\mathbf{q}\cdot\mathbf{b}/2)} \frac{\sin^2(N_c\mathbf{q}\cdot\mathbf{c}/2)}{\sin^2(\mathbf{q}\cdot\mathbf{c}/2)} \tag{2.15}$$

with N_a, N_b, N_c the number of unit cells in the three crystallographic directions. The intensity is a function that is sharply peaked when each of the denominators of the interference functions equal zero, which is often called the three Laue conditions being simultaneously fulfilled. In fact this is nothing else than the Bragg law, which is given by:

$$2d_{hkl}\sin(\theta) = n\lambda \tag{2.16}$$

with θ half the scattering angle and n an integer (usually 1) and,

$$\frac{1}{d_{hkl}} = |\mathbf{H}_{hkl}| = |h\mathbf{a}^* + k\mathbf{b}^* + l\mathbf{c}^*| \tag{2.17}$$

the so-called d-spacing where hkl are the Miller indices, $\mathbf{H}_{hkl}$ is the scattering vector and $(\mathbf{a}^*, \mathbf{b}^*, \mathbf{c}^*)$ the reciprocal lattice vectors. The relation between the incoming and outgoing wavevectors and the scattering angle is established by using

$$|\mathbf{k} - \mathbf{k_0}| = |\mathbf{q}| = 4\pi\frac{\sin(\theta)}{\lambda} \tag{2.18}$$

It is seen that the interference function goes to a maximum when the Bragg condition is fulfilled, which means that there is positive interference between X-rays

scattered by consecutive lattice planes. The points where this happens are therefore determined by the translational symmetry in the crystal. The peak intensity at these points is proportional to $N^2|F_{hkl}|^2$, from which two things become clear. First of all, the crystal volume determined by the number of unit cells N appears squared, which is a sign of interference. It is not merely a sum over all unit cells, which would imply $I \propto N$. In a typical experiment however, a crystal is often rotated after which the so-called integrated intensity is obtained [22]. Since the width of the interference function is proportional to $1/N$, the integrated intensity is proportional to N. Second, the intensity is proportional to the squared modulus of the structure factor, and can therefore be zero! This will depend on the symmetry of the electron density within the unit cell. So far only translational symmetry was considered, but in fact there are many more possible symmetry relations within the crystal lattice, which can be found in the *International Tables* [23]. Each structure factor is a Fourier component of the crystal's electron density, and by measuring many structure factors, the electron density can be determined. It follows directly from Bragg's law that the structure factor most distant from the origin in reciprocal space accessible in an experiment is given by the maximum reciprocal lattice spacing:

$$d^*_{max} = \frac{2}{\lambda} = |ha^* + kb^* + lc^*|_{max} \tag{2.19}$$

which shows that in principle the number of Fourier components that can be measured is limited. Furthermore, the total number of Fourier components that can be measured is limited by the noise becoming more important for high scattering angles. The last point is closely related to the crystal quality: good crystals scatter up to high angles.

Summarizing: the scattering pattern of crystalline materials will have very sharp maxima as function of angle of the X-ray beam with respect to the crystal lattice. The positions of these peaks are determined by the translational symmetry of the lattice, hence materials without this property will not give rise to Bragg diffraction. The height of the maxima is determined by the structure factor, which is given by the positions of the atoms in the unit cell. The symmetry of the electron density can also give rise to zero intensities, which is known as systematic absences.

2.4 Surface X-ray Diffraction

In the previous section, kinematical X-ray diffraction by a bulk crystal was discussed. From the resulting expression of the diffracted intensity given by eq. 2.15, it is seen that when the crystal becomes very large ($N \to \infty$), the interference functions approach δ peaks. In reality, however, crystals are often not as perfect as would be required to reach a δ shape. The kinematical theory of diffraction applies to many so-called ideally imperfect crystals, which are described by a mosaic of many small crystals. Here the kinematical theory will be extended to include the influence of a surface on the scattered intensities. Since crystals do not extend over the whole space, there is an abrupt termination of the electron density at the faces of the crystal. Besides the truncation of the crystal, the influence of surface roughness on the scattering will be briefly touched upon as well.

2.4.1 Truncation

If a step function is used to describe one of the faces of the crystal, this corresponds to multiplying the electron density with this step function, by convention in the crystallographic **c**-direction. The effect in reciprocal space will then be a convolution of the Bragg δ peaks, with a $1/\mathbf{q}$ function, the Fourier transform of the step function. This results in each Bragg peak having $1/\Delta\mathbf{q}^2$ tails in the l direction, with $\Delta\mathbf{q}$ measured from the peak position. Hence, the Bragg peaks are interconnected by these non-zero intensity tails along l. These diffraction features, the so-called Crystal Truncation Rods (CTR's), are at the heart of Surface X-ray Diffraction (SXRD) [24]. The effect of truncation is usually modified by the fact that due to absorption of the X-ray beam, only a finite number of atomic layers participate in the scattering process. To enhance this effect even more, the typical scattering geometry in a SXRD set up is in grazing incidence, because this enhances the surface sensitivity. Hence, an expression for the scattered intensity is found by summing over unit cell layers by:

$$F_{bulk}(\mathbf{q}) = \sum_{j=-\infty}^{0} F_{bulk\ u.c.}(\mathbf{q}) e^{i\mathbf{q}\cdot\mathbf{c}j} e^{-j\alpha}, \tag{2.20}$$

with $F_{bulk\ u.c.}$ the structure factor of the bulk unit cell (eq. 2.13) and α is the attenuation length per unit cell layer. The diffracted intensity is then expressed as:

$$I_{bulk}(\mathbf{q}) \propto |F_{bulk\ u.c.}(\mathbf{q})|^2 \frac{\sin^2(N_a\mathbf{q}\cdot\mathbf{a}/2)}{\sin^2(\mathbf{q}\cdot\mathbf{a}/2)} \frac{\sin^2(N_b\mathbf{q}\cdot\mathbf{b}/2)}{\sin^2(\mathbf{q}\cdot\mathbf{b}/2)} \times \frac{1}{4e^{-\alpha}\left(\sin^2(\mathbf{q}\cdot\mathbf{c}/2)+\sinh^2(\alpha/2)\right)} \tag{2.21}$$

The CTR, I_{bulk}, has maxima when the Laue conditions are met, i.e. for (some) integer values of h, k and l, just like in the bulk diffraction case (section 2.3). In between two Bragg peaks, the monotonically decreasing tails along l meet in one global minimum.

When structural changes, like atomic relaxations, occur in the surface region, equation 2.21 has to be modified. This leads to simply adding a surface term to the sum in equation 2.20:

$$I(\mathbf{q}) \propto |F_{bulk}(\mathbf{q}) + F_{surf}(\mathbf{q})|^2 \tag{2.22}$$

where for F_{surf} one sums over all atoms in the surface unit cell. The Fourier transform of the surface region, F_{surf}, is a function that is again peaked for certain values of h and k but will in general not show maxima as a function of l, because it is not periodic in this direction. For a so-called bulk-terminated crystal, obviously the two terms F_{surf} and F_{bulk} are equal and the sum of eq. 2.22 reverts to the expression of equation 2.21. In case of surface reconstructions or relaxations, the contribution F_{surf} differs from $F_{bulk\ u.c.}$ and the shape of the CTR is modified with respect to the bulk CTR's. Since the scattered intensity is the interference sum of the bulk and surface contributions, the latter will affect the intensity along a CTR mainly for non-integer values of l.

2.4.2 Surface roughness

Real surfaces will in general have some roughness, which alters the shape of the crystal truncation rods. One aspect of roughness is that it is the *random* distribution of atoms. Surface atoms that are ordered either by well defined and regularly placed islands (quantum dots) or as in the case of surface reconstructions are not referred to as roughness. Therefore, including roughness in the calculation of the CTR's, reduces the problem to knowing the normalized electron density along the z-direction. In equation 2.20 this means that each layer of unit cells is no longer fully occupied. A

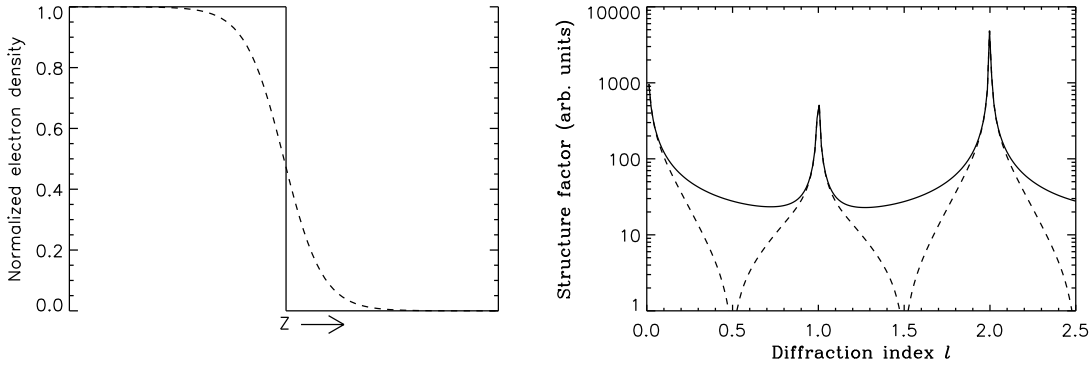

Figure 2.2: Influence of surface roughness on the shape of CTR's. Shown are (left) a normalized electron density in the z-direction, which is parallel to the surface normal. The step function in case of a perfect surface (solid) and when roughness is present (dashed). The corresponding specular CTR's of bulk terminated $SrTiO_3(001)$ (right) are shown without (solid) and with (dashed) roughness.

simulation is shown in figure 2.2 of step functions for a perfect and rough surface. The largest proportional differences in scattered intensity are seen exactly halfway between the Bragg reflections, the so-called anti-Bragg points. These are the positions along the CTR where the scattering contributions of two consecutive unit cells in the z-direction are out of phase and therefore cancel each other. For the particular symmetric and smoothly varying function that is used here, the occupancies of two consecutive layers are practically the same. Therefore the scattering of the two layers will almost completely cancel each other and the CTR will go almost to zero at the anti-Bragg point. The resulting structure factor will depend on the particular configuration of the surface atoms. For a perfectly smooth surface covered by only one layer for example, a zero intensity is expected when half of the surface is covered. In general when roughness is present, the corresponding CTR's lie always lower in intensity than for a perfectly smooth surface. The peak intensities of the Bragg points are unaffected by surface roughness, and therefore the tails around the Bragg peaks of the CTR's are sharper than for the smooth surface [25]. This is also understood from equation 2.20. The Fourier transform of a perfectly truncated crystal, will result in the tails of the Bragg points in reciprocal space to fall of as $1/(\Delta q_z)^2$, with Δq_z measured from the Bragg point. Roughness will result in a step function that in real space is smoother than for perfect truncation, and hence the corresponding tail will be sharper than $1/(\Delta q_z)^2$ in reciprocal space.

In principle, SXRD is a very powerful technique to study the surface roughness on an atomic scale. However, one needs a good model to describe the atomic distribution at the crystal/vacuum interface adequately. A simple and often effective one is the so-called β-model [25], which assumes an occupancy β^n for the n-th unit cell layer above the bulk.

2.5 X-ray Intensity Growth Oscillations

The previously discussed features of the effect of roughness on the scattered intensities, have been extensively described already in the 1980s [26, 27] and were used to qualitatively explain Reflection High Energy Electron Diffraction (RHEED) experiments. By using X-rays to study in situ the homoepitaxial deposition of Ge, it was for the first time possible to also quantitatively explain the scattered intensities [28]. Growth of thin layers in general occurs in three regimes (see paragraph 1.3.2), which differ in the morphology evolution. The diffracted intensities during growth are adequately described by the so-called birth-death models [29], which use the occupancy as a function of time of different levels in the growth system. Before start of the deposition, all levels are unoccupied. With the arrival of material, the first level, that is the first layer on top of the substrate starts to grow, after which, depending on the growth mode, the next levels start to become occupied. In the layer-by-layer regime, where a next level starts to get occupied only after the level underneath has been completely filled, the roughness cycles between smooth and rough. As seen in paragraph 2.4.2 this will result in the diffracted intensity also cycling between a maximum and a minimum. In the kinematical approximation and by ignoring absorption this can be written as:

$$I \propto \left| \frac{F_{sub}}{1 - e^{-i\mathbf{q}\cdot\mathbf{c}}} + \sum_j \theta_j(t) F_{layer} e^{i\phi_j} \right|^2 \tag{2.23}$$

with F_{sub} and F_{layer} the structure factors of the substrate and ad-layer respectively, $\mathbf{q}$ the momentum transfer and $\mathbf{c}$ the substrate c-axis, which results in the first term being the substrate CTR (see eq. 2.21). The occupancy θ is a function of time t and goes from zero to one for each level. In the ideal case, only after layer $j-1$ has reached an occupancy of one, the j-th layer starts to become occupied. The scattering contribution of each ad-layer has its own phase ϕ_j, which for the so-called

anti-Bragg position is given by:

$$\phi_j = j\pi, \text{ with } j = 1, 2, 3... \tag{2.24}$$

In case the out-of-plane lattice parameters of the substrate and ad-layer are identical, the expected growth intensity oscillations are shown in figure 2.3 c) for homoeptitaxial ($F_{sub} = F_{layer}$) and d) for heteroepitaxial ($F_{sub} \neq F_{layer}$) growth. In case of homoepitaxial growth, the intensity returns to the initial value of the CTR upon completion of each monolayer, simply because there is no difference after adding one complete monolayer to the surface. For heteroepitaxial growth, this is not the case. Since the phase ϕ_j, given by eq. 2.24, alternates between 0 and π. This means that if the substrate is covered by an even number of completely filled unit cell layers, their scattering cancels completely, and the resulting intensity is just that of the bare substrate[1]. For a completely filled odd number of ad-layers, the intensity is different from the bare substrate. For each coverage where a non-integer number of ad-layers is filled, roughness is present, resulting in some intermediate intensity. In case of step-flow (figure 2.3 a), it was already mentioned that the morphology of the surface does not change during growth. In the idealized case, where the deposited ad-layer starts to grow on one side of the substrate and gradually covers it all the way up to the other side, i.e. one progressing step, the surface can be considered to be completely flat throughout the deposition. In this particular idealized case, the diffracted intensity[1] during deposition of the k-th layer can be written as:

$$I \propto (1 - \theta(t)) \left|F_{k-1}\right|^2 + \theta(t) \left|F_{k-1} + F_{layer} e^{i\phi_k}\right|^2 \tag{2.25}$$

with all the symbols as previous, and:

$$F_{k-1} = \frac{F_{sub}}{1 - e^{-i\mathbf{q}\cdot\mathbf{c}}} + \sum_{j=1}^{k-1} F_{layer} e^{i\phi_j} \tag{2.26}$$

the contribution of all the layers up to level $k-1$. Since in the step-flow regime only one layer grows at the time, equation 2.26 gives the scattering amplitude of a film of thickness $k-1$ unit cell layers on top of a substrate. Figure 2.3 a) shows the expected intensity for step-flow in the homo- and heteroepitaxial case. In the homoepitaxial case at each moment during growth the surface is the same, resulting in a constant

[1]Ignoring absorption of the ad-layer.

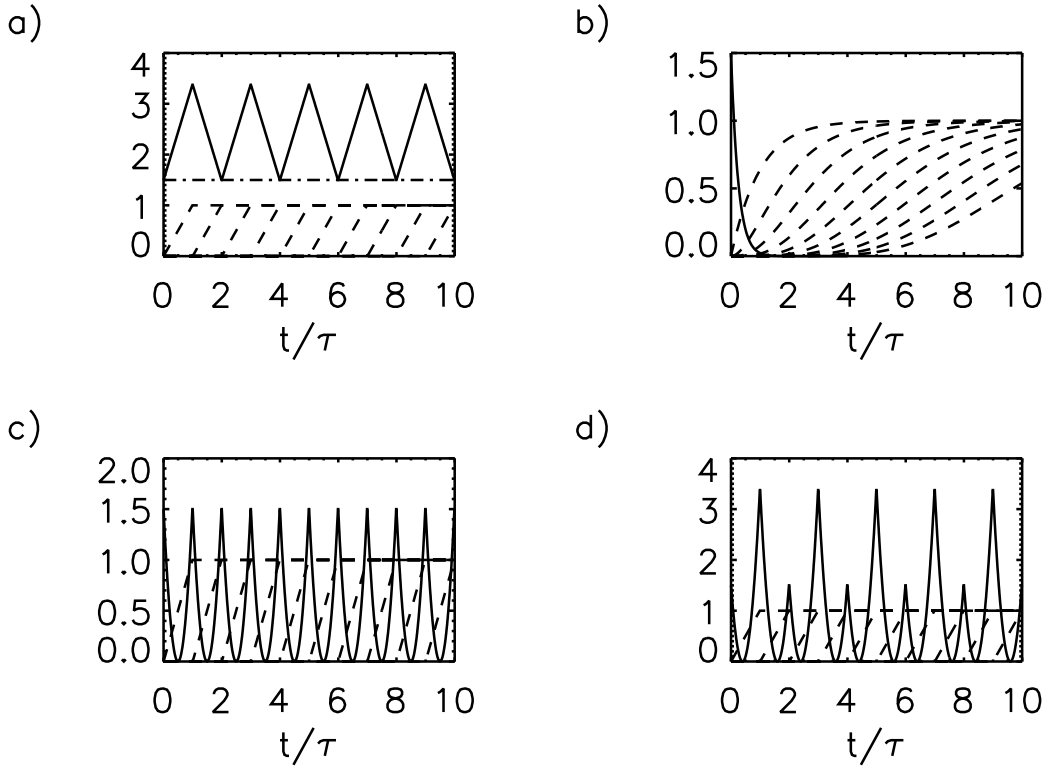

Figure 2.3: Schematic view of growth intensity oscillations for both homo- and heteroepitaxial deposition. Shown are the different growth modes a) step-flow, b) 3D-island growth and c),d) layer-by-layer growth. The dashed lines in all four figures represent the occupation for each layer as a function of the equivalent number of grown monolayers (t/τ, with t the time and τ the time neeeded to grow one monolayer). In figure a), the solid line represents the diffracted intensity during heteroepitaxial growth and the dash-dotted line, which is constant as function of the number of deposited monolayers, represents homoepitaxial growth. The solid lines in all four figures show the diffracted intensity at the anti-Bragg point ($l = \frac{1}{2}$) defined by the reciprocal lattice of the layer (see text).

intensity during growth. In the heteroepitaxial case however, the structure changes, resulting in the intensity changing. Again, the phase of each added layer alternates between 0 and π, just like in eq. 2.24 for layer-by-layer growth. Since the growth rate is taken constant as a function of time, the intensity just changes linearly from that of the bare substrate to that of the substrate and one ad-layer and then back again. Now the two terms in eq. 2.25 are easily interpreted, as like having two crystals, one is a $k-1$ unit cell layers thick film on the substrate and the other is a k unit cell layers thick film on the substrate. The intensity of the first diminishes linearly as a function of coverage and the second increases linearly with the same coverage, up to the point where the film has reached a thickness of k unit cell layers. Depending on whether k is even or odd, the final intensity is just that of the bare substrate, or that of the bare substrate and one unit cell layer[1]. The third growth mode, 3D-island growth, results in a quickly dimishing intensity, which is shown in figure 2.3 b). Immediately after start of deposition, several levels become occupied, resulting in the intensity dropping to zero. As described in the previous paragraph, the diffracted intensity in an SXRD experiment, is extremely sensitive to the surface roughness, making this technique very useful to study the thin film evolution. Depending on the growth mode, many island distributions are possible, each resulting in a different diffraction pattern. The dynamics of the growth are adequately described by the so-called birth-death models [29], which use the temporal occupancy of different levels in the growth system.

2.6 Synchrotron X-ray Sources

Gaining experimental access to the structure of surfaces or nanocrystals, puts severe demands on the X-ray source used. A simple numerical example of the expected diffracted intensity of a monolayer of atoms given by Robinson *et al.* [25], shows that the diffuse scattering is about a factor of 10^5 lower than the Bragg peaks. If one further considers that the diffracted intensity of a Bragg reflection, in case of an ideally imperfect crystal, is in general a factor $10^4 - 10^6$ lower than the intensity of the incoming beam, it follows that there are about ten orders of difference between the incoming and diffracted intensities. In order to obtain statistically relevant data, within an acceptable time frame, it is therefore needed to have a large incoming X-ray photon flux. At present, the most powerful X-ray sources available are the so-called third generation synchrotrons. The first generation synchrotrons were initially meant

only as circular accelerators for high energy physics. In those days, the loss of energy by the the charged particles due to the emission of radiation was seen only as a nuisance. However, as it became clear that the properties of the emitted radiation were very usefull for a wide range of sciences using X-rays, specially dedicated machines were built. In a circular accelerator, the charged particles are kept in a closed orbit by a magnetic field and the energy that is lost at every turn is replenished by an oscillating radio-frequency (RF) electric field. Each of the points where the trajectory of the particle beam is altered contains a so-called bending magnet. The straight section between two bending magnets can be used to insert magnets that act as even more powerful sources of radiation. In case of the third generation machines, the number of insertion devices, consisting of multiple magnets that 'wiggle' or 'undulate' the charged particle beam thereby producing even more X-rays, was optimized. Without going into too much detail about the physics of synchrotron radiation, which can be found in numerous publications [30, 14, 31], a few of the properties and their use will be described here.

If the charged particles have a velocity close to the speed of light, which is the case for a machine operating in the GeV range, relativistice effects come into play. One of the effects is that the energies of the emitted photons are Doppler-shifted over a wide range of photon energies, up to the hard X-ray regime. Most of the applications require monochromatic radiation, which results in the use of crystal optics for tailoring the beam. Another relativistic effect is that the emitted radiation is confined to a narrow cone, of which the angular divergence is proportional to $1/\gamma$, with $\gamma = \sqrt{1/(1-(v/c)^2)}$ the Lorentz transformation. This is essentially where the gain of photon flux at the sample position is coming from: the total number of created photons is not much increased in comparison to conventional X-ray sources, only they are all confined to a very small solid angle. Typically, the horizontal and vertical angular divergences for bending magnet radiation are of the order of 1 and 0.1 mrad respectively. This results already in a gain of 10^8 photons in this solid angle compared to a beam emitted through a 4π solid angle of a conventional source emitting the same number of photons [2]. A consequence of the small divergence for diffraction experi-

[2]This simplified numerical example should not be taken as a general difference in flux between synchrotron and conventional sources, but serves only as an "order of magnitude" example. There are many other factors playing a role, like the shape of the spectrum that for X-ray tubes consists of the contributions of bremsstrahlung and of photons emitted by electronic transitions that are element-specific. Furthermore, use of focused X-rays, that differs from set-up to set-up, will

ments is an increase in the signal-to-noise ratio of reflections for mosaic crystals. By making use of insertion devices, the aforementiond properties can be even improved. In case of so-called undulators, consisting of an array of N magnets, the divergence will be reduced by a factor of N, whereas due to coherent superposition of radiation emitted at different bends, the flux increases with N^2. To compare the performance of different sources the brilliance, expressed as $photons/s/mrad^2/mm^2/(0.1\%$ *of the bandwidth)* is often used. The brilliance of an X-ray tube is around 10^7 whereas typical values for different sources at the European Synchrotron Radiation Facility (storage ring 6 GeV) are $10^{14}, 10^{15}$ and 10^{20} at 200 mA ring current for a bending magnet, a wiggler and an in-vacuum undulator respectively.

References

[1] W. C. Röntgen, Nature **53** (1896) 273–276.

[2] W. Friedrich, P. Knipping, M. Laue, Proceedings of the Bavarian Academy of Sciences (1912) 303–322.

[3] See e.g. IUCR journal *Acta Crystallogr. D*.

[4] L. Margulies, G. Winther, H. F. Poulsen, Science **291** (2001) 2392.

[5] V. Šrajer, T. Teng, T. Ursby, C. Pradervand, Z. Ren, S. Adachi, W. Schildkamp, D. Bourgeois, M. Wulff, K. Moffat, Science **274** (1996) 1726.

[6] I. K. Robinson, Acta Cryst. A **54** (1998) 772–778.

[7] E. Vlieg, Surf. Sci. **500** (2002) 458–474.

[8] C. Sun, Prog. Mater. Sci. **48** (2003) 521–685.

[9] M. Ackermann, O. Robach, C. Walker, C. Quiros, H. Isern, S. Ferrer, Surf. Sci. **557** (2004) 21–30.

[10] W. Braun, *Applied RHEED: Reflection High Energy Electron Diffraction during Crystal Growth*, Springer-Verlag, Berlin, 1999.

[11] A. J. H. M. Rijnders, G. Koster, D. H. A. Blank, H. Rogalla, Appl. Phys. Lett. **70** (1997) 1888.

determine to a great extent the photon flux.

[12] J. M. Cowley, *Diffraction Physics*, North-Holland, Amsterdam, 1990.

[13] B. E. Warren, *X-ray Diffraction*, Addison-Wesley, Massachusets, 1969.

[14] E. Hecht, *Optics*, Addison-Wesley, Massachusets, 1987.

[15] J. Als-Nielsen, D. McMorrow, *Elements of Modern X-ray Physics*, John Wiley and Sons, New York, 2001.

[16] M. Krivoglaz, *X-ray and Neutron Diffraction in Non-ideal Crystals*, Springer Verlag, Berlin-Heidelberg, 1996.

[17] C. Cohen-Tannoudji, J. Dupont-Roc, G. Grynberg, *Atom-Photon Interactions: Basic Processes and Applications*, John Wiley & Sons Inc., New York, 1998.

[18] R. W. James, *The Optical Principles of the Diffraction of X-rays*, G. Bell and Sons Ltd, London, 1965.

[19] D. Feil, Cryst. Rev. **8** (2002) 95.

[20] A. J. C. Wilson (Ed.), *International Tables for Crystallography*, Vol. C : Mathematical, Physical and Chemical Tables, Kluwer academic publishers, Dordrecht, 1995.

[21] P. Carra, B. T. Thole, Rev. Mod. Phys. **66** (1994) 1509–1515, and references therein.

[22] M. M. Woolfson, *An Introduction to X-ray Crystallography*, 2nd Edition, Cambridge University Press, Cambridge, 1997, chapter 6.

[23] T. Hahn (Ed.), *International Tables for Crystallography*, Vol. A : Space-group symmetry, Kluwer academic publishers, Dordrecht, 1995.

[24] I. K. Robinson, *Handbook on Synchrotron Radiation*, Vol. **3**, North-Holland, Amsterdam, 1991, Ch. 7, pp. 221–266.

[25] I. K. Robinson, Phys. Rev. B **33** (1986) 3830.

[26] C. S. Lent, P. I. Cohen, Surf. Sci. **139** (1984) 121–154.

[27] P. R. Pukite, C. S. Lent, P. I. Cohen, Surf. Sci. **161** (1985) 39–68.

[28] E. Vlieg, A. W. D. van der Gon, J. F. van der Veen, J. E. MacDonald, C. Norris, Phys. Rev. Lett **61** (1988) 2241–2244.

[29] P. I. Cohen, G. S. Petrich, P. R. Pukite, G. J. Whaley, A. S. Arrott, Surf. Sci. **216** (1989) 222–248.

[30] P. Coppens, *Synchrotron Radiation Crystallography*, Academic Press, London, 1992, with contributions from D. Cox and E. Vlieg & I. K. Robinson.

[31] G. Margaritondo, J. Synchrotron Rad. **2** (1995) 148.

Chapter 3

The $SrTiO_3$(001) Surface

3.1 Introduction

Strontium-titanate, $SrTiO_3$ (STO), falls within the class of perovskite-type oxides, having general formula ABO_3. The A and B-sites can be occupied by elements with different valencies and different ionic radii and the properties and structures of these materials are closely related to the size of the cations and anions. Most of the perovskites show a transition from cubic to tetragonal, and with that a change in properties, upon cooling through a critical temperature [1]. Although $SrTiO_3$ undergoes a structural phase transition around 110 K, similar to $BaTiO_3$, it is not ferro-electric in the tetragonal phase [2]. This has lead to a series of publications on the structure and properties of $SrTiO_3$ [3, 4, 5, 6, 7].

Recently, $SrTiO_3$ has gained interest due to the need for high-K dielectrics in the micro-electronics industry. With the electronic patterns of e.g. transistors becoming ever smaller, the need arises for materials that do not have too high leak-currents due to tunneling effects. Furthermore, STO is used on a large scale as substrate material for the growth of thin film perovskite-type materials, like high-T_c superconductors. In the last case, which makes use of epitaxial growth, and subsequent interface engineering, the substrate surface structure and more importantly the control of this structure, is of great interest [8].

Different preparation methods and analysis techniques to elucidate the nature of the (001) surface have been employed over the past two decades, and at present single terminated surfaces can be obtained [9, 10, 11]. However, a sound model describing the atomic surface structure has not been established to date. For example, it is well known, that depending on the annealing conditions different reconstructions

occur [12, 13, 14, 15]. Most studies agree that these reconstructions are formed by oxygen vacancies, while Kubo *et al.* [16, 17] propose a model in which an ordered Sr adatom occurs on the surface. Additionally, the theoretical and experimental results concerning the (001) surface obtained so far, have found no consensus between them, and the matter is still in the course of debate.

Here, we present the results of Surface X-ray Diffraction (SXRD) experiments carried out on two different single terminated crystals. Single termination is obtained by a special treatment consisting of chemical etching and annealing [11]. The etching process takes place in an aqueous environment and the anneal step in 1 bar of flowing oxygen after which the crystals are kept at ambient conditions before being used for thin film growth. The questions that arrise from the previously mentioned treatment is what the atomic surface structure is at these conditions, if the termination can be determined and whether the surface is stable. To answer these questions, the SXRD measurements were carried out in air. In the following sections a detailed description of the crystallographic structure of STO is given. After that an overview is given of the sample preparation and details about the data collection. Next, a discussion follows in which several models proposed in the literature are compared with our data and a new model is presented.

3.2 Atomic structure of $SrTiO_3$

3.2.1 $SrTiO_3$

The atomic structure of $SrTiO_3$, given in figure 3.1, can be seen as a network of 6-fold oxygen co-ordinated titanium atoms, with strontium in the interstitial sites, leading to a stack of alternating TiO_2 and SrO layers.

This means that the (001) face of a macroscopic crystal can have three types of terminations, i.e. TiO_2, SrO or a mixture of both. In general, upon cleaving and polishing the (001) surface will consist of terraces with mixed termination. Neighbouring terraces will have alternate terminations when the step height is an odd number of half unit cells. In order to obtain single terminated surfaces, which have unit cell step heights of the terraces, further treatment is needed. This may consist of chemical etching and annealing in specific oxygen environments. Both the surface morphology, e.g. the smoothness of the terrace ledges, and the atomic structure are influenced by the treatment. As described in section 3.3, the samples used in the experiments are

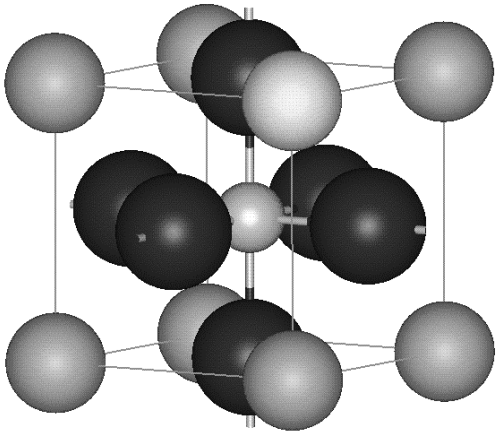

Figure 3.1: The structure of bulk $SrTiO_3$. The largest atoms are oxygens, the smallest in the body-centre is titanium and strontium occupies the corners.

single terminated.

Bulk STO has space group $Pm\bar{3}m$, with a=3.901(1) Å [18] at room temperature, and all atoms occupy special positions with fractional co-ordinates as shown in table 3.1

3.2.2 Shape of crystal truncation rods

Surface X-ray Diffraction (SXRD) is a well-established technique to obtain structural information about the crystal surface. It makes use of the diffuse scattering in between Bragg peaks, the so-called crystal truncation rod, which is present due to the non-periodicity of the crystal in the direction of the surface normal [19], i.e. the crystal ends at the surface. This sharp-boundary-effect is modified by the fact that only a finite number of atomic layers participate in the scattering process, due to absorption of the X-ray beam. Unlike electron diffraction methods, in the case of X-rays the kinematical description applies, where the diffracted intensity is proportional to the squared modulus of the structure factor. A detailed description of the calculation of the structure factors and hence the crystal truncation rods can be found in chapter

Atom	x	y	z
Sr	0	0	0
Ti	$\frac{1}{2}$	$\frac{1}{2}$	$\frac{1}{2}$
O1	$\frac{1}{2}$	$\frac{1}{2}$	0
O2	$\frac{1}{2}$	0	$\frac{1}{2}$
O3	0	$\frac{1}{2}$	$\frac{1}{2}$

Table 3.1: Atomic fractional co-ordinates in bulk $SrTiO_3$.

2 and elsewhere [19, 20]. Choosing the crystallographic directions in such a way that h and k are lying in the plane of the surface, while l points in the out-of-plane direction, the crystal truncation rods are measured along l.

Using the atomic positions from table 3.1, the bulk contribution, or equivalently the scattering from bulk terminated STO, can be examined.

It follows that the scattering contributions of $O2$ and $O3$ cancel each other when $(h + k)$ is odd. Furthermore, when disgarding the Debye-Waller parameter, crystal truncation rods (CTR's) exist with three different shapes. First, all CTR's for which $(h + k)$ is odd have identical shapes. Second, in the case of $(h + k)$ even, one can distinguish between CTR's with both h and k either even or odd. All this holds as well in case of reconstructions with the planar symmetry P4mm, which contains a four-fould rotation axis along the z-direction. This means that (x, y) of the fractional co-ordinates remains the same as in the bulk and that the z-value can change.

3.3 Experimental

Optically polished z-cut crystals (10×10 mm^2) were obtained from Surfacenet GmbH (Rheine, Germany). The angle between the optical surface-normal and the crystallographic z-direction, the so-called miscut angle, is in the order of 0.1 degrees. To obtain single termination, the as-received double terminated crystals are treated chemically in a NH_4F-buffered HF solution (BHF), with $4.5 < \text{pH} < 6.0$ [21]. It is believed that the SrO surface layers react to form a hydroxy-complex , which subsequently dissolves in water [22], thereby leaving a TiO_2-terminated surface. Finally, the surface is subjected to an annealing treatment at 950 °C in flowing oxygen for two hours.

Atomic Force Microscopy (AFM) measurements show that the terraces are 3.9 Å high, which corresponds to exactly one unit cell (3.901 Å) , and that their ledges are particularly smooth. Furthermore, this surface treatment results in sharp (1×1) Reflection High Energy Electron Diffraction (RHEED) patterns [11], indicating that no reconstructions occur.

SXRD experiments were carried out at two different beamlines at the European Synchrotron Radiation Facility (ESRF). Two different samples were used, both prepared as described above. Data for one of the crystals were collected at ID03 [23], the other crystal was measured at BM26 [24]. Both experiments were performed in air and at room temperature and resulted in the collection of several crystal truncation rods. The experiment at ID03 was carried out on a horizontal z-axis diffractometer, whereas on BM26 a vertical 2+3 type diffractometer was used. Details about the geometry of these kind of diffractometers can be found elsewhere [25].

3.4 Results

The program ANA is used to integrate and correct the data, according to the particular diffraction geometry as described elsewhere [26, 25], in this way the measured data are reduced to structure factors. Symmetry equivalent structure factors are averaged and merged using the program AVE. Like in RHEED measurements, no fractional order peaks are found for both samples, indicating that no planar reconstruction occurs. The validity of this finding will be discussed in more detail further on. This means that for both samples the planar space group P4mm is used in the merging procedure, i.e. each F_{hkl} is symmetry equivalent with $F_{\bar{h}kl}$, $F_{h\bar{k}l}$, $F_{\bar{h}\bar{k}l}$, F_{khl}, $F_{\bar{k}hl}$, $F_{k\bar{h}l}$ and $F_{\bar{k}\bar{h}l}$. This results in unique CTR's *11, 20, 21, 22, 30, 31* and *32* for crystal 1 and CTR's *11, 20, 22, 30, 31* and *32* for crystal 2. An overview of the results for the two samples is given in Table 3.2.

Although the data set of crystal 1 contains more reflections and crystal truncation rods than that of crystal 2, the overall multiplicity is close to one, meaning that of the set of eight symmetry equivalent reflections only one is measured. The resulting estimated standard deviations (e.s.d.'s), which are then only based on photon-counting statistics, are less realistic than those of the data set of crystal 2. The value R_{merge} of 6.1 % for the data set of crystal 2 is an indication that the systematic errors (e.g. alignment of the sample) are fairly small. The influence of the miscut angle on the

	crystal 1	crystal 2	crystal 1&2
termination	single	single	-
miscut (deg)	-	0.07	-
wavelength (Å)	0.725	0.778	-
incident angle (deg)	0.25	1.0	-
no. measured points	231	262	493
no. unique points	197	122	217
no. CTR's	7	6	7
$\left(\frac{sin(\theta)}{\lambda}\right)_{min}$	0.12	0.18	0.12
$\left(\frac{sin(\theta)}{\lambda}\right)_{max}$	0.63	0.59	0.63
R_{merge} (%) [a]	8.2	6.1	10.7

[a] $R_{merge} = \frac{\sum_{hkl}\sum_i ||F_i(hkl)|-\overline{|F(hkl)|}|}{\sum_{hkl}\sum_i |F_i(hkl)|}$

Table 3.2: Crystal data, experimental data and results of merging. In the last column the data sets of crystal 1 and 2 are merged by applying one scale factor between them.

positions of the reflections was not noticeable during data collection [27], therefore this effect can be neglected. A further indication of the quality of the data can be obtained by merging both data sets, using a single scale factor between them. This assumes that the two samples are identical, as well as the experimental conditions, like temperature. The value of R_{merge} of 10.7% indicates the two data sets to be comparable, and of good quality. The two data sets are nevertheless dealt with independently in the remainder of this article, because that assures the highest possible accuracy.

3.5 Discussion

In the following sections four different literature models are discussed by testing them against our data. Although the preparation methods and experimental conditions can be quite different from ours, these models are used as a starting point for comparison with our data. The models include a variety of possible distortions that have been published to date. The final goal of this rather thorough comparison is to show what the influence of these distortions is on the scattering patterns. In order to minimize the number of fit parameters, the models have not been combined. In the end, the

best fit is obtained by a new model, consisting of an oxygen overlayer on top of a TiO_2-terminated crystal.

The program ROD [28] is used to calculate structure factors and thus crystal truncation rods for a given model. ROD uses a χ^2-minimization method to determine the best fit parameters. As an indication of how well the model describes the measured data, the following commonly used parameter is calculated as well:

$$R = \frac{\sum_{hkl} ||F_{obs}(hkl)| - k|\ F_{calc}(hkl)||}{\sum_{hkl} |F_{obs}(hkl)|}. \tag{3.1}$$

In case of the literature models, the proposed numerical values of the displacements are taken and only the overall scale factor k is fitted. In this way the shapes of the calculated CTR's are investigated and compared with the data. When possible, a fit procedure of the displacement and thermal parameters is run and those results are presented as well. However, not every literature model describes the data well enough to run a least squares fit procedure, because certain fit parameters get unrealistic values.

The following assumptions are made regarding the thermal parameters and surface roughness in the model. The atoms in the bulk have isotropic thermal parameters $B_{Sr} = 0.62$ Å^2, $B_{Ti} = 0.44$ Å^2 and $B_O = 0.72$ Å^2, which are taken from Abromov *et al.* [18]. From the AFM measurements (section 3.3) it is clear that on the terraces the surface is atomically flat. Furthermore, the miscut angle is small enough that it does not influence the positions of the CTR's (section 3.4), and therefore the surface roughness is taken to be zero [27].

For those models that do not restrict distortions to occur in the first layer only, the atoms are labelled with increasing numbering starting at the surface going into the bulk.

3.5.1 Rumpling of surface

Most of the theoretical [29, 30, 31, 32, 33] and experimental [34, 35, 36, 37] studies carried out so far have assumed a model consisting of a bulk terminated surface, with slight rumpling and displacement of the topmost layers. Measurements and calculations have been performed for SrO, TiO_2 and mixed type of terminations. It is assumed that only displacements in the z-direction occur and that like in the case of

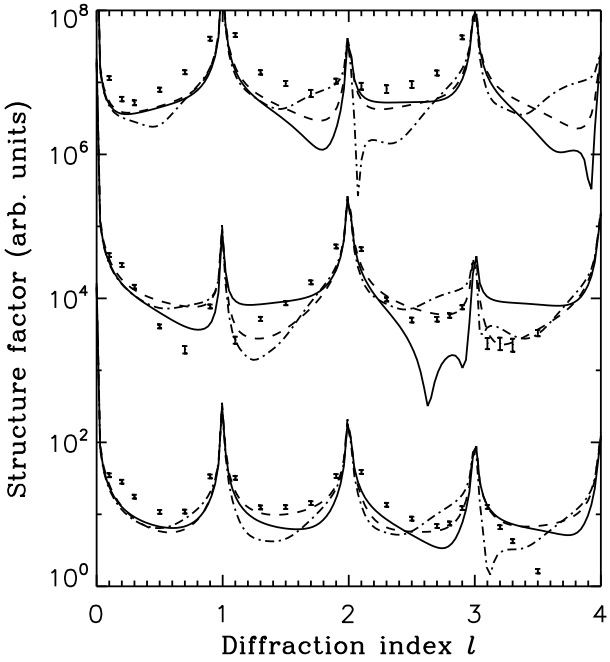

Figure 3.2: Crystal truncation rods calculated using the relaxations for the TiO_2-terminated surface found by Bickel *et al.* [35] (solid line), Cheng *et al.* [32] (dash-dotted line) and Charlton *et al.* [37] (dashed line). Shown are the *32* (top), *20* (middle) and *11* bottom) rods (the errorbar is included for the experimental data points) which are calculated by refining only the overall scale factor for the whole data set.

rumpling for other ionic solids, the larger anions move towards the vacuum and the smaller cations towards the bulk. Although the displacements found with this model seem to be very reasonable, the studies do not agree with each other. Surprisingly enough in the TiO_2-terminated case, it seems that whereas the theoretical studies systematically find a relaxation towards the bulk of the outermost layer, the experiments systematically indicate the opposite.

In figures 3.2 and 3.3 calculated CTR's, using the relaxations found by Bickel *et al.* [35], Cheng *et al.* [32] and Charlton *et al.* [37], are presented together with the experimental data.

The displacements of the atoms found by each of the authors are listed in Table 3.3 and these are used together with a fitted overall scale factor for the CTR calculations. Of the displacements reported by Cheng *et al.*, only the first two layers are presented in table 3.3, whereas the CTR's shown in the figures are calculated using

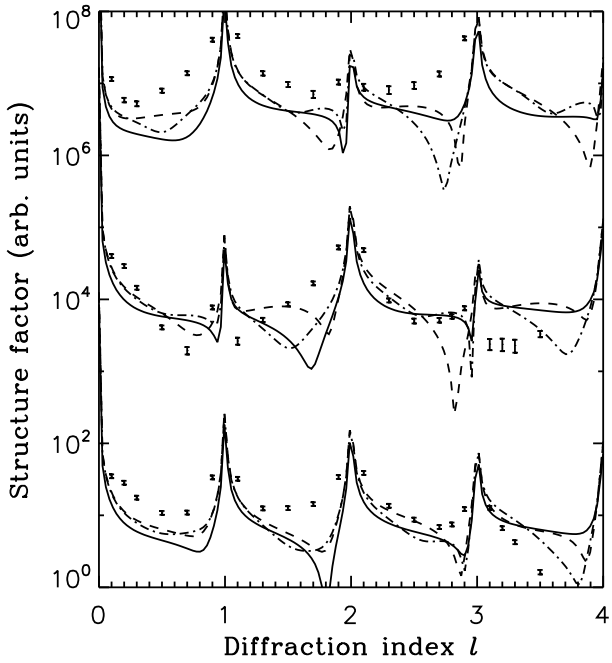

Figure 3.3: Crystal truncation rods calculated by using the relaxations for the SrO-terminated surface found by Bickel *et al.* [35] (solid line), Cheng *et al.* [32] (dash-dotted line) and Charlton *et al.* [37] (dashed line). Only the overall scale factor is refined. Experimental data points including the errorbar are shown for the *32* (top), *20* (middle) and *11* (bottom) CTR's.

the displacements of all four layers.

The resulting R-factors and χ^2-values are listed in the summary table 3.7.

When comparing the displacements found for both terminations, it is seen that on average the heavier atoms, Sr and Ti, move more in the SrO-terminated crystals. This is reflected in the shape of the CTR's (fig. 3.3), where all of them have sharp minima between most of the Bragg peaks. These sharp features are also present in the *32* and *20* CTR in case of the Bickel and Cheng models for the TiO_2 surface (fig. 3.2). The model of Charlton in case of TiO_2 termination, with the smallest displacements for the Ti and Sr, follows the shape of the data the best. However, all the TiO_2-terminated models fit less well for the higher order CTR's (i.e. having higher in-plane momentum transfer), than for the lower order, indicating a scaling problem.

	TiO_2-termination				SrO-termination			
	Ti1	O1	Sr1	O2	Sr1	O1	Ti1	O2
Bickel *et al.*	2	4	-2	-2	-10	-6	4	4
Charlton *et al.*	0	-12.8	-0.2	5	-6.4	-7.6	-6.1	-10.2
Cheng *et al.*	-1.8	-0.3	4.6	0.8	-6.7	1.0	1.8	0.3

Table 3.3: Relaxations of the atoms in the z-direction for the rumpling model. All values are in percentage of the bulk c-axis length. Only displacements of the first two atom layers are presented, although some authors included more layers in their model.

3.5.2 Low temperature-like structure

Bulk STO undergoes a cubic-to-tetragonal phase-transition around 110 K [2]. The crystal structure changes from $Pm\bar{3}m$ to I4/mcm, by a rotation of the oxygen octahedra around one of the principle axes. The diagonals of the cubic structure are the principle axes of the tetragonal, low temperature, phase. Experimental evidence has been found for the existence of the low temperature phase in the surface region at an onset temperature much higher than in the bulk. Mishina *et al.* [38] find a change in the (110) surface at a temperature around 150 K. They conclude that this is the low temperature non-centrosymmetric phase due to the detection of optical second harmonics. Krainyukova *et al.* [39] conclude from their electron diffraction study, that at a temperature around 170 K the (001) surface transforms to the tetragonal phase.

Here, in the CTR calculations, we use this low-temperature model. It consists of a rotation of the oxygens around the 4-fold titanium atom, as indicated in fig. 3.4.

This distortion is, in first approximation, restricted to the topmost TiO_2 layer. Despite the absence of fractional order reflections, the validity of this model is tested, because the rotations are very small (typically 3^o), and therefore the surface distorts only a little, which means that fractional order reflections are extremely weak.
Due to the change of symmetry from the cubic to tetragonal structure, the following transformations concerning the indices of diffraction have to be made:

$$H_t = MH_c, \tag{3.2}$$

with,

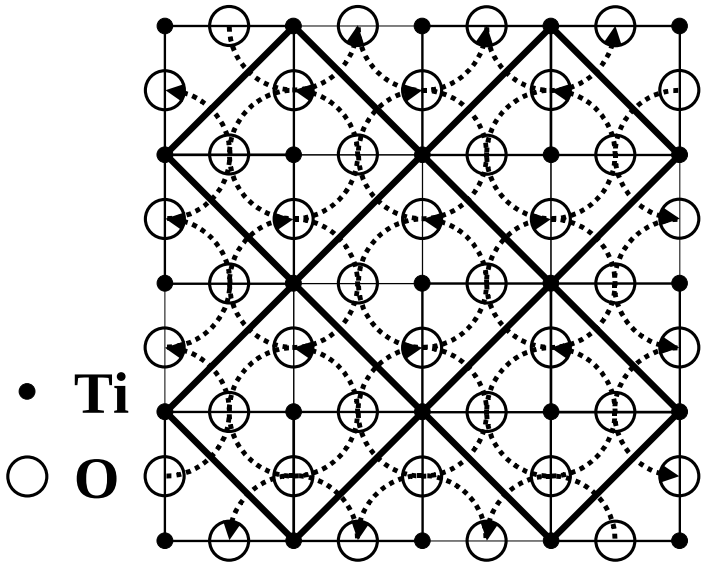

Figure 3.4: Planar view of the oxygen rotations in the TiO_2-plane of the low temperature tetragonal phase. The diagonals of the initial cubic phase form the a and b axes of the tetragonal phase (bold). The central Ti in the newly formed planar unit cell is four-fold co-ordinated by oxygens, which in turn rotate over the dotted circle, as indicated by the black arrowheads

$$M = \begin{pmatrix} 1 & -1 & 0 \\ 1 & 1 & 0 \\ 0 & 0 & 1 \end{pmatrix}. \tag{3.3}$$

The diffraction indices hkl are denoted by H and the subscripts t and c indicate the notation in tetragonal and cubic symmetry respectively. The fractional co-ordinates $r = (x, y, z)$ of the atoms change by [40]:

$$r_t = \left(M^{-1}\right)^T r_c. \tag{3.4}$$

In fig. 3.5 the resulting CTR's are shown for rotation angles of 3, 6 and 12 degrees.

To show only the effect of the oxygens concerned in the rotation on the CTR's, all other atoms are kept in their bulk positions and only the overall scale factor is refined. All CTR's shown in the figures as well as discussed in the remainder of this paragraph are denoted in tetragonal notation. The resulting R-factors and χ^2-values

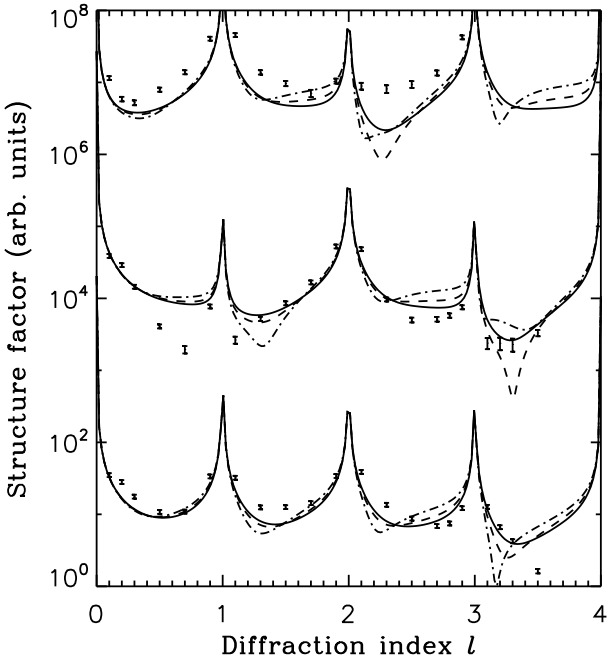

Figure 3.5: Calculated CTR's in I4/mcm notation *51* (top), *22* (middle) and *20* (bottom) for different rotations of the oxygen octahedra. No relaxations in the z-direction are used, only the four oxygens around the Ti are rotated by 3 (solid line), 6 (dashed line) and 12 (dash-dotted line) degrees. Experimental data points are shown including their error bar.

are listed in the summary table 3.7.

The higher the rotation angle by which the oxygen octahedra tilt, the sharper the features in the CTR's get. In case of the *22* CTR this results in a better fit of the dip just after the *221* Bragg peak. At the same time, however, the region between the *222* and *223* becomes flatter, which is not what the data indicate. The same holds for the *51* rod, where the flatness and the dip occur between l =1 and $l = 3$, whereas the data indicate a much smoother curve. Systematically, the calculated values for the *51* CTR are too low, while the lowest order *11* CTR is much better fitted.

3.5.3 Strontium adatom

As stated before, depending on the annealing conditions different kind of reconstructions have been found. Most of the studies agree on the effect of ordering of oxygen vacancies at the surface. However, Kubo *et al.* [17, 16] argue that these reconstruc-

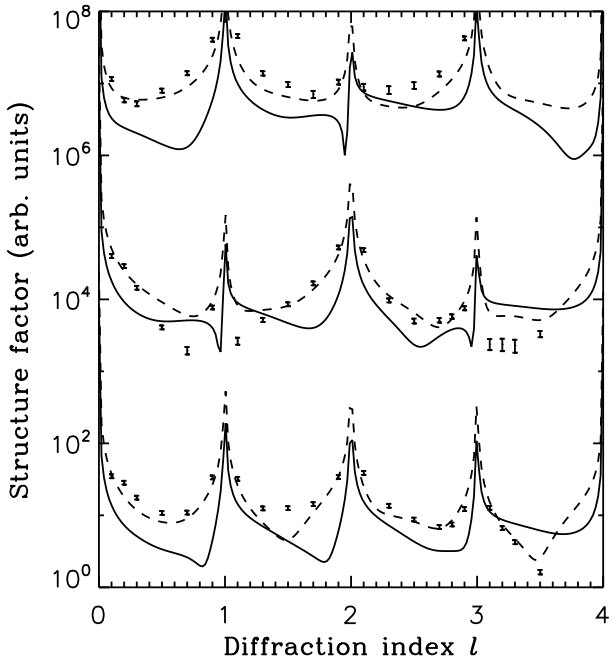

Figure 3.6: Calculated CTR's for the model of an ordered Sr adatom on the TiO_2 surface. Shown are the *32* (top), *20* (middle) and *11* (bottom) CTR's in case of the displacements found by Kubo *et al.* [16] (solid) and our best fit (dashed). Experimental data points are shown including their error bar.

tions are formed by additional Sr atoms on the surface. The coverage and subsequent ordering of these adatoms, form a whole range of different reconstructions. In case of a (1×1) reconstructed surface, this means that there are two possibilities. Either the coverage of adatoms is zero, which is equivalent with a normal TiO_2-terminated crystal, or on top of the TiO_2 layer, a complete Sr-layer exists. The latter is equivalent to having a SrO-terminated surface, and subsequently removing all the oxygens. Here, we investigate the model in which the coverage of Sr-adatoms is one, because when the coverage is zero the structure resembles the one where rumpling occurs (section 3.5.1). Kubo *et al.* reported relaxations for the topmost Sr-layer and the two layers underneath, where in each layer both kind of atoms displace equally. Both the results for the displacements found by Kubo *et al.* [16] as well as the best fit to our data by using this model are plotted in figure 3.6.

The displacements are listed in table 3.4, the resulting R-factors and χ^2-values are shown in summary table 3.7.

	Kubo *et al.*	Present
Sr1	-13	0.81±0.04
Ti1	7.9	1.4±0.1
O1	7.9	−2.3±0.2
Sr2	-1.6	0.59±0.03
O2	-1.6	1.5±0.4

Table 3.4: Displacements relative to the bulk positions in the z-direction for the Sr-adatom model. Values reported by Kubo *et al.* and present best fit results are listed. All displacements are listed as a percentage of the bulk lattice parameter.

In case of the displacements found by Kubo, the CTR's show large asymmetry before and after the different Bragg peaks. This does not at all correspond to the data. By running a fitting procedure of the Sr-adatom model, in which the atoms are allowed only to move in the z-direction, a better fit is obtained. As can be seen in table 3.4, the results for the present fit to our data, indicate only positional changes in the order of 1 % for the heavier atoms, resulting in much smoother CTR's. However, the data around the *201* Bragg peak is not very well described, as well as most of the *32* CTR is too low compared with the data.

3.5.4 Lateral displacement

Ravikumar *et al.* [41] suggested a model in which the top layer of the SrO-terminated surface displaces laterally. Both the Sr and O shift along the same principle axis, although with different magnitudes and in opposite directions (see figure 3.7).

The TiO_2-terminated surface should not undergo such a reconstruction. In case of the mentioned lateral displacement, the planar P4mm symmetry would be broken. However, the results of merging (see section 3.4) do not indicate the absence of a 4-fold rotation axis around the [001] direction. Therefore the validity of this model is tested under the assumption of four different co-existing domains, related through 90-degree rotation around the [001] direction. Figure 3.8 shows the CTR's calculated using the findings of Ravikumar *et al.* [41] as well as fits for SrO and TiO_2 terminated surfaces with lateral displacements. In table 3.5 the displacements are listed.

In all cases a domain structure as described previously is used and no relaxation in the z-direction is applied. The resulting R-factors and χ^2-values are listed in table

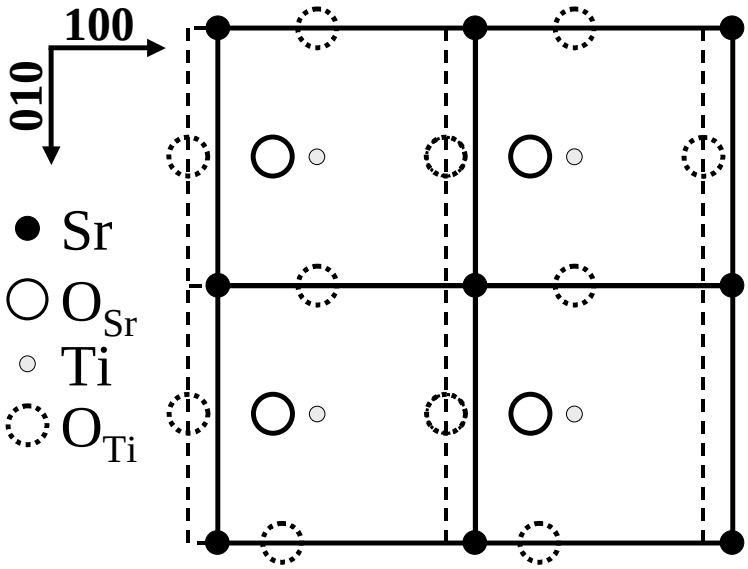

Figure 3.7: Schematic overview of the lateral displacement as proposed by Ravikumar *et al.* [41]. Here the distortion is shown where the Sr moves in the [100] direction and the oxygen in the topmost layer moves in the [-100] direction. The TiO_2-layer underneath remains in its bulk position (indicated by the dashed line). To maintain the symmetry of the four fold axis, a structure, consisting of four 90-degrees rotated domains, is used in the calculations. The subscripts for the oxygens indicate whether they are part of the topmost Ti-layer or the Sr-layer underneath.

	Ravikumar *et al.*	present	
	SrO	SrO	TiO_2
$\Delta x(Sr,Ti)$	19.5	0.80±0.06	−9.0±0.4
$\Delta y(Sr,Ti)$	-	0.3±0.5	1±5
$\Delta x(O)$	2.6	33±1	7±1
$\Delta y(O)$	-	−21±2	−10±1

Table 3.5: Relaxations in case of lateral displacements. Both the findings of Ravikumar *et al.* [41] as well as our best fit results are shown. All values are expressed in a percentage of the bulk lattice parameter.

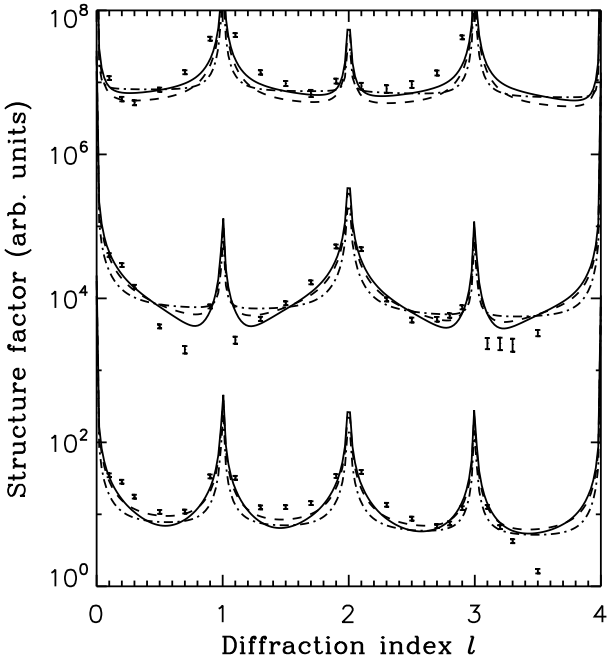

Figure 3.8: Calculated CTR's in the case of lateral displacements. In case of the reconstruction found by Ravikumar *et al.* [41] (dash-dotted line), SrO-termination (solid line) and TiO_2 termination (dashed line) and. The *32* (top), *20* (middle) and *11* (bottom) CTR's are shown. Experimental data points are indicated by their error bar.

3.7.

It is seen that the overall shape of the different CTR's in fig 3.8 corresponds rather well to the data. Particularly the two minima around the 201 Bragg peak are present, though still too shallow, when using the SrO termination. When taking the model of Ravikumar, the Bragg peaks are too narrow, or equivalently the modelled Bragg peaks are not strong enough. It is noted that all data are used in the refinement of the overall scale factor, meaning that a better fit could be obtained when using only the rods plotted in fig. 3.8.

3.5.5 Oxygen overlayer model

Already from the shape of the CTR's, calculated by using different literature models, it becomes clear that none of them reproduces the data very well. When considerable relaxation for the heavier Sr and Ti atoms is present in the z-direction, the CTR's show dips in between two Bragg peaks, as can be seen in figures 3.2, 3.3 and

3.6. Those models where no z-displacements of these atoms are used, such as the low temperature-like structure and the lateral displacement (sections 3.5.2 and 3.5.4 respectively), give the best result. This would indicate that the crystal is bulk terminated. The shapes of the rods with high in-plane momentum transfer or having both h and k odd, are described quite accurately by the bulk terminated model. In contrast, the two dips at lower and higher momentum transfer of the *201* Bragg point, shown for example in figure 3.2, are not well described by assuming bulk termination. The CTR's having a different shape, as discussed in section 3.2.2, also seem to have a different scale factor. This can be seen for example in figure 3.2 where the calculated bulk contributions for the *32* and *11* CTR seem to be too low in comparison with the experimental data. As stated before, this indicates that the heavier atoms, Sr and Ti, remain in their bulk positions. This leaves the oxygens to be considered as accounting for the differences seen between our data and a model using bulk termination. For the oxygens present in the structure there are in principle two different possibilities. First they could relax, either laterally or perpendicularly to the surface. However, in case of displacements of the oxygens, just like it is seen in section 3.5.1, those alone do not give a satisfactory result for all CTR's. Second the occupancy of the oxygens could change. Assuming that subsequently to oxygen-outdiffusion of the topmost layer, ordering of the vacancies occurs, the occupancy change can be ruled out, since no fractional order peaks are found. Moreover, adjusting the occupancy of the oxygens does not solve the previuosly described problem of fitting all CTR's simultaneously. Therefore we propose a model in which the terminating layer consists of oxygen atoms on top of a TiO_2 terminated cell. These oxygens occupy (x, y) positions: $(0,0), (\frac{1}{2},0), (0,\frac{1}{2})$ and $(\frac{1}{2},\frac{1}{2})$, thereby respecting the planar P4mm symmetry. Because the atomic scattering factor for these additional oxygen atoms falls off rapidly as function of $\frac{sin(\theta)}{\lambda}$, they will contribute little to the higher order CTR's. The resulting CTR's are shown in figure 3.9 and the displacements are listed in table 3.6. Figure 3.10 shows the resulting structure.

The displacements listed in table 3.6 are found with the data set of crystal 1. Using the data set of crystal 2 gives similar results, only the uncertainties in the thermal parameters are even larger. Another indication that the surfaces of the two crystals are well described by the oxygen overlayer model is seen in the overall scale factors obtained from the two fits. The ratio between the overall scale factors is exactly the scale factor that is applied when merging the two data sets (see Table 3.2). The resulting R-factors and χ^2-values are listed in table 3.7.

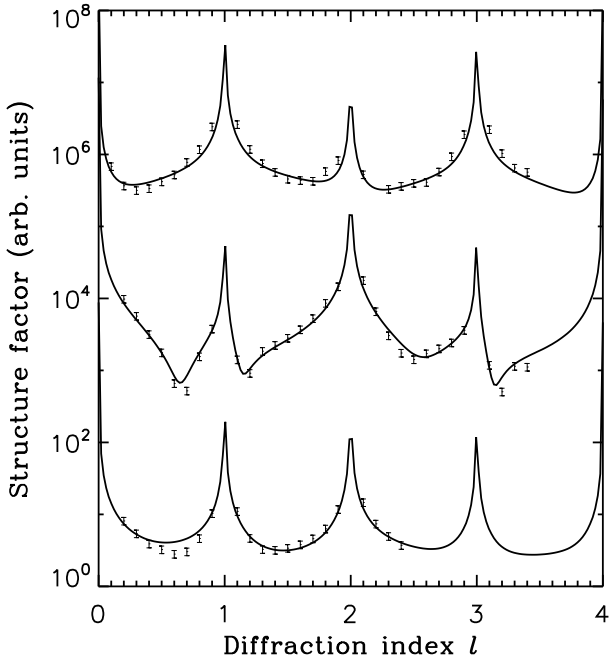

Figure 3.9: Experimental data points and CTR's obtained with the oxygen overlayer model. Shown are the *32* (top), *20* (middle) and *11* (bottom) CTR's, where the error bars indicate the experimental data points.

Atom	x	y	z	$B_{\|\|}$ (Å^2)	$B_{\perp}$ (Å^2)
O1	0	0	1.08±0.03	5±4	10±2
O2	$\frac{1}{2}$	0	1.037±0.001	0.3±0.7	0.4±0.5
O3	$\frac{1}{2}$	$\frac{1}{2}$	1.04±0.01	0.2±0.7	3±1
Ti	$\frac{1}{2}$	$\frac{1}{2}$	0.481±0.005	1.0±0.5	1.6±0.5
O4	$\frac{1}{2}$	0	0.50±0.01	0.7±0.7	–

Table 3.6: Refined positions and thermal parameters of the different atoms found for the present oxygen overlayer model. Fractional co-ordinates (x, y, z) are indicated, where z is zero in the bulk. Atom O4 is assumed to have an isotropic thermal parameter.

Model	crystal 1				crystal 2			
	TiO_2		SrO		TiO_2		SrO	
	R	χ^2	R	χ^2	R	χ^2	R	χ^2
Surface rumpling								
Bickel *et al.*	47	20	61	26	62	30	73	36
Charlton *et al.*	37	14	52	21	49	21	64	29
Cheng *et al.*	47	19	54	23	59	26	64	29
Low temperature-like								
3° rotation	50	22	-	-	53	24	-	-
6° rotation	49	21	-	-	52	23	-	-
12° rotation	46	19	-	-	50	22	-	-
Lateral displacements								
Ravikumar *et al.*	-	-	52	17	-	-	57	21
present	36	10	33	8.7	46	17	39	13
Sr adatom								
Kubo *et al.*	63	27	-	-	75	37	-	-
present	29	8.3	-	-	38	12	-	-
Oxygen overlayer								
present	16	2.3	-	-	26	5.8	-	-

[a] $\chi^2 = \frac{1}{N-p-1} \sum_{hkl} \frac{(|F_{obs}(hkl)|-s|F_{calc}(hkl)|)^2}{\sigma^2(F_{obs}(hkl))}$, with N the number of observed structure factors, p the number of refined parameters and s the overall scalefactor [42]. The errors, $\sigma(F_{obs})$, are mainly determined by the systematic errors, which have been taken twice the value R_{merge} of crystal 2 (see section 3.4), resulting in 12%.

Table 3.7: Overview of the resulting R-factors (eq. 3.1) and reduced χ^2 [a] values for all different models as described in the text. Both SrO as well as TiO_2-terminated models are tested against the data of crystal 1 and crystal 2. Values for the R-factors are in %.

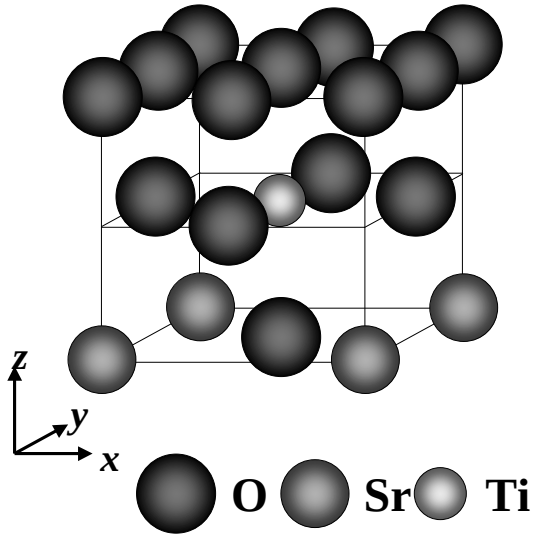

Figure 3.10: Present model showing the oxygen overlayer on top of a TiO_2-terminated STO crystal. In the lowest SrO layer no relaxations are assumed, the displacements of the TiO_2 layer and oxygen overlayer are listed in table 3.6.

The first questions that arise from the present model are where these additional oxygens come from and what the bond lengths correspond to. It is well known that STO and similar compounds, like TiO_2, adsorb water [43], where usually the water oxygen (O_w) binds to the particular surface. In general, at temperatures lower than about 300K water adsorbs as molecules, whereas at higher temperatures dissociation takes place and hydroxyl groups are formed [43]. The surface structure is also found to be of importance. In the case of rutile TiO_2, the (110) face adsorbs water molecularly in contrast to the (100) face, where dissociation of water takes place [44]. It is believed that depending on the distance of the O_w to the nearest binding site, one of the hydrogens detaches [44]. Recently, it was found that the TiO_2(011) (2×1) surface adsorbs water in a mixed molecular/dissociated state [45, 46]. For TiO_2-terminated STO(001) it was found that defects, such as step edges and oxygen vacancies, act as catalytic centres for the dissociation of water [47, 48]. Similar results with respect to defects on STO(001) were obtained for the adsorption and reaction of CO and CO_2 [49]. In the case of adsorption of water on the face of a crystal, one expects the water layer to be ordered due to the surface crystal structure. Water layers, completely in

registry with the underlying crystal surface and partially disordered layers, have been found for several systems. In the case of KH_2PO_4 growth from the solution, Reedijk *et al.* [50] find water layers starting from completely ordered at the interface to completely disordered in the solution, with O–O distances of approximately 3 Å. The unstrained hydrogen bonded O–O distance is around 2.7 Å at room temperature. Similar water layers have been found on mica [51], whereas on hexagonal Ru(0001) a ring-like structure resembling ice I_h and consisting of partially dissociated water [52], has been identified. In both systems the O–O distances are 2.5-2.7 Å, which suggests that they are hydrogen-bonded. In the present model the shortest O–O bonds are close to 2 Å, which rules out normal hydrogen bonds. Even in ice X, known for its extremely short O–O distances, the pressure has to be well above 140 GPa in order to have the oxygens approach each other to about 2 Å [53]. On the other hand, Chu *et al.* [54] find an O–O distance of 2.3(1) Å for the electrochemical RuO_2(110)/water interface in an electric field of $\approx 10^9$ V/m, which obviously is the driving force for this particular O–O configuration. Reverting to the present model, it is arguable whether the O2 oxygens in the topmost layer are present. If absent, all O–O distances would be enlarged to approximately 2.8 Å, which would then suggest hydrogen bonding. The fit by leaving out the O2 oxygens in the topmost layer results in the underlying O4 oxygens to be pulled out of the Ti-layer. However, the resulting χ^2 value becomes worse, and furthermore the particular features as described previously in the *20* and *22* CTR's are less well described. Another indication that O2 describes the experimental data rather well is seen in the temperature factors, shown in table 3.6. These might even suggest that O1 is absent, which does not solve the problem of the short O–O distances. The possibility of adsorption of carbonates was examined as well (see [49]). For this the O2 was replaced by a carbon atom. Due to the similarity in atomic scattering factor between C and O, the fits are not substantially different, though with a slightly better χ^2 value for the oxygen overlayer model. However, the thermal parameters for the carbon become zero in the fit, and the subsequently refined occupancy becomes 1.25. Fitting the occupancy of O2 in the oxygen overlayer model, results in a value close to 0.9. Since the difference in atomic scattering factor, as used in ROD, between O and C is about 30% for small angles, the resulting occupancies and thermal parameters seem to indicate that indeed the atom at the $(\frac{1}{2}, 0)$ position should be oxygen. In the final oxygen overlayer model of which the results are listed in table 3.6, no attempts were made at fitting the occupancies and all positions in the overlayer are assumed to be fully occupied.

It seems that the O–O distances in the present model are too short to be hydrogen bonds and too long to be completely covalent bonds, like in molecular oxygen (1.2 Å), ozone (1.3 Å) or H_2O_2 (1.5 Å). The nature of the O–O bonds in the present model might be clarified by verifying the presence and/or location of hydrogens. Lopez *et al.* [55] find no signature of O–H bonds in their high resolution electron energy loss spectroscopy (HREELS) study on clean STO(001) surfaces, unlike when Na is present. This might indicate that the surfaces used here are either not clean or that water dissociates completely into H_2 and O, like has been found for the Si(111)-7×7 surface [56]. Unfortunately, in the present study the used technique of SXRD is not sensitive to the scattering of hydrogen atoms. Furthermore, the current data do not include the specular CTR, which for very low angles would contain some information about hydrogens in the structure.

The fact that the literature models do not fit very well to our data might be attributed to the difference in characterization technique, experimental conditions or sample preparation, of which an overview is given in Table 3.8. All of the aforementioned authors have carried out their experiments in vacuum or presumed the crystals to be in vacuum for their calculations. Therefore, a similar experiment performed in vacuum and at elevated temperatures would allow for a more careful comparison. Next, the differences in sample preparation between the present work and the earlier studies result in different surfaces. The chemical treatment used here gives single terminated (001) surfaces, while other treatments result in double termination. However, all studies report (1×1) reconstructed surfaces. Finally, our experiment compares the best with the SXRD study of Charlton *et al.*. Unfortunately, the data set that is obtained in that experiment is rather limited and not very sensitive to the oxygens in the surface. Furthermore, the fact that a double terminated crystal is used, complicates the matter even more, due to the increase in the number of fit parameters. Nevertheless, when assuming that there is indeed a layer covering the surface in air, which might very well dissapear by Ar^+ sputtering, the structure of the TiO_2 layer underneath is differing only slightly from the bulk.

author	termination	polishing/ cleaning	annealing	experimental conditions
Charlton *et al.*	double	Ar^+ sputtering	900 K, 10^{-6} mbar O_2	UHV
Bickel *et al.*	double	Ar^+ sputtering	900 K, flash to 1400 K	UHV
Krainyukova *et al.*	not reported	chemo-mechanical	high temperature	UHV 170 K

Table 3.8: Preparation and experimental conditions for STO(001) surfaces by different authors.

3.6 Conclusions

The atomic surface structure of single terminated $SrTiO_3$ (001) (1 × 1) crystals, obtained by chemical etching and annealing in oxygen, is studied in air using SXRD. AFM measurements confirm that the surface is single terminated and the absence of fractional order reflections in both RHEED and the present SXRD measurements indicate no lateral surface reconstruction. Two crystals, prepared in the same manner, are used in two different experiments. From the results of merging the two data sets it is concluded that both the preparation method as well as the SXRD experiments are carried out in a reliable and reproducible way. Models as proposed in literature can not be fitted satisfactorily to our data. First of all, those models in which the heavier Ti and/or Sr atoms displace more than about 0.2 Å from their bulk positions, do not agree with the higher order SXRD data. Second, those models that keep the heavier atoms in their bulk positions, lack enough degrees of freedom for the oxygens to adequately fit the lower order data. A complete overview of the resulting R-factors (see eq. 3.1) and reduced χ^2 values for each of the models is given in table 3.7. A model in which a TiO_2-terminated surface is completely covered by oxygen leads to the best fit. This oxygen overlayer model leads to O–O distances close to 2 Å. Since hydrogen bonds would result in O–O distances close to 2.7 Å, these short distances seem to rule out hydrogen bonding and would point towards a more covalent binding character between the nearest oxygens. Most likely the oxygen overlayer is formed due to the (dissociative) adsorption of water, possibly occurring during the chemical etching or further surface treatment process. Verifying the presence of hydrogen

would be very helpful in clarifying the nature of the oxygen overlayer, however the method used here is not capable of doing so. The TiO_2-layer underneath the oxygen layer displays only slight rumpling, close to bulk termination. When comparing this with previous studies, this would be an indication that the surface is very stable, regardless UHV or preparation conditions.

References

[1] F. Jona, G. Shirane, *Ferroelectric Crystals*, Dover Publicatitions, New York, 1993.

[2] G. Shirane, Y. Yamada, Phys. Rev. **177** (1969) 858.

[3] S. M. Shapiro, J. D. Axe, G. Shirane, Phys. Rev. **B6** (1972) 4332.

[4] K. A. Müller, W. Berlinger, Phys. Rev. Lett. **26** (1971) 13.

[5] R. A. Cowley, W. J. L. Buyers, G. Dolling, Solid State Commun. **7** (1969) 181.

[6] T. Sakudo, H. Unoki, Phys. Rev. Lett. **26** (1971) 851.

[7] W. G. Stirling, J. Phys. C:Solid State Phys. **5** (1972) 2711.

[8] G. Rijnders, S. Curràs, M. Huijben, D. Blank, H. Rogalla, Appl. Phys. Lett. **84** (2004) 1150.

[9] M. Kawasaki, K. Takahashi, T. Maeda, R. Tsuchiya, M. Shinohara, O. Ishiyama, T. Yonezawa, M. Yoshimoto, H. Koinuma, Science **266** (1994) 1540.

[10] M. Kawasaki, A. Ohtomo, T. Arkane, K. Takahashi, M. Yoshimoto, H. Koinuma, Appl. Surf. Sci. **107** (1996) 102.

[11] G. Koster, G. Rijnders, D. H. A. Blank, H. Rogalla, Physica C **339** (2000) 215.

[12] Q. Jiang, J. Zegenhagen, Surf. Sci. **367** (1996) L42.

[13] Q. Jiang, J. Zegenhagen, Surf. Sci. **425** (1999) 343.

[14] T. Nishimura, A. Ikeda, H. Namba, T. Morishita, Y. Kido, Surf. Sci. **421** (1999) 273.

[15] N. Erdman, L. D. Marks, Surf. Sci. **526** (2003) 107.

[16] T. Kubo, H. Nozoye, Surf. Sci. **542** (2003) 177.

[17] T. Kubo, H. Nozoye, Phys. Rev. Lett. **86** (2001) 1801.

[18] Y. A. Abramov, V. G. Tsirelson, V. E. Zavodnik, S. A. Ivanov, I. D. Brown, Acta Cryst. **B51** (1995) 942.

[19] I. K. Robinson, *Handbook on Synchrotron Radiation*, Vol. **3**, North-Holland, Amsterdam, 1991, Ch. 7, pp. 221–266.

[20] R. Feidenhans'l, Surf. Sci. Rep. **10** (1989) 105.

[21] G. Koster, B. L. Kropman, G. Rijnders, D. H. A. Blank, H. Rogalla, Mater. Sci. Eng. B **56** (1998) 209.

[22] G. Koster, B. L. Kropman, G. Rijnders, D. H. A. Blank, H. Rogalla, Appl. Phys. Lett. **73** (1998) 2920.

[23] S. Ferrer, F. Comin, Rev. Sci. Instrum. **66** (1995) 1674.

[24] M. Borsboom, W. Bras, I. Cerjak, D. Detollenaere, D. G. van Loon, P. Goedtkindt, M. Konijnenberg, P. Lassing, Y. K. Levine, B. Munneke, M. Oversluizen, R. van Tol, E. Vlieg, J. Synchr. Rad. **5** (1998) 518.

[25] E. Vlieg, J. Appl. Cryst. **31** (1998) 198.

[26] E. Vlieg, J. Appl. Cryst. **30** (1997) 532.

[27] A. Munkholm, S. Brennan, J. Appl. Cryst. **32** (1999) 143.

[28] E. Vlieg, J. Appl. Cryst. **33** (2000) 401.

[29] J. Padilla, D. Vanderbilt, Surf. Sci. **418** (1998) 64.

[30] Z. Q. Li, J. L. Zhu, C. Q. Wu, Z. Tang, Y. Kawazoe, Phys. Rev. B **58** (1998) 8075.

[31] J. Prade, J. Phys.:Condens. Matter **5** (1993) 1.

[32] C. Cheng, K. Kunc, M. H. Lee, Phys. Rev. B **62** (2000) 10409.

[33] E. Heifets, R. I. Eglitis, E. A. Kotomin, J. Maier, G. Borstel, Phys. Rev. B **64** (2001) 235417.

[34] A. Ikeda, T. Nishimura, T. Morishita, Y. Kido, Surf. Sci. **433** (1999) 520.

[35] N. Bickel, G. Schmidt, K. Heinz, K. Müller, Phys. Rev. Lett. **62** (1989) 2009.

[36] T. Hikita, T. Hanada, M. Kudo, J. Vac. Sci. Technol. A **11** (1993) 2649.

[37] G. Charlton, S. Brennan, C. A. Muryn, R. McGrath, D. Norman, T. S. Turner, G. Thornton, Surf. Sci. **457** (2000) L376.

[38] E. D. Mishina, N. E. Sherstuyk, V. V. Lemanov, A. I. Morozov, A. S. Sigov, T. Rasing, Phys. Rev. Lett. **85** (2000) 3664.

[39] N. V. Krainyukova, V. V. Butskii, Surf. Sci. **454** (2000) 628.

[40] D. E. Sands, *Vectors and Tensors in Crystallography*, Addison-Wesley, New York, 1982.

[41] V. Ravikumar, D. Wolf, V. P. Dravid, Phys. Rev. Lett. **74** (1995) 960.

[42] P. R. Bevington, Data reduction and error analysis for the physical sciences, McGraw-Hill, New York, 1969.

[43] P. Thiel, T. E. Madey, Surf. Sci. Rep. **7** (1987) 211.

[44] M. A. Henderson, Langmuir **12** (1996) 5093.

[45] T.J.Beck, A.Klust, M.Batzill, U.Diebold, C.DiValentin, A.Tilocca, A.Selloni, Surf. Sci. Lett.In press.

[46] C.DiValentin, A.Tilocca, A.Selloni, T.J.Beck, A.Klust, M.Batzill, Y.Losovvj, U.Diebold, J.Am. Chem. Soc. **127** (2005) 9895.

[47] R. G. Egdell, P. D. Naylor, Chem. Phys. Lett. **91** (1982) 200.

[48] N. B. Brookes, G. Thornton, F. M. Quinn, Solid State Comm. **64** (1987) 383.

[49] S. Azad, M. H. Engelhard, L.-Q. Wang, J. Phys. Chem. B **109** (2005) 10327.

[50] M. F. Reedijk, J. Arsic, F. F. A. Hollander, S. A. de Vries, E. Vlieg, Phys. Rev. Lett. **90** (2003) 066103.

[51] L. Cheng, P. Fenter, K. L. Nagy, M. L. Schlegel, N. C. Sturchio, Phys. Rev. Lett. **87** (2001) 156103.

[52] J. Weissenrieder, A. Mikkelsen, J. N. Andersen, P. J. Feibelman, G. Held, Phys. Rev. Lett. **93** (2004) 196102.

[53] M. Benoit, D. Marx, M. Parrinello, Nature **392** (1998) 258.

[54] Y. S. Chu, T. E. Lister, W. G. Cullen, H. You, Z. Nagy, Phys. Rev. Lett. **86** (2001) 3364.

[55] A. Lopez, T. Heller, T. Bitzer, Q. Chen, N. Richardson, Surf. Sci **494** (2001) L811.

[56] R.-L. Lo, I.-S. Hwang, T. Tsong, Surf. Sci **530** (2003) L302.

Chapter 4

Chamber for in situ X-ray Diffraction during Pulsed Laser Deposition

4.1 Introduction

Pulsed Laser Deposition (PLD) is a very successful technique that is ever more used for the growth of complex oxide thin films [1]. It makes use of a laser to ablate target-material, which is deposited on a heated substrate, where a thin film is grown. Since with each laser pulse only a fraction of a monolayer is deposited, the thickness of the film can be controlled very accurately. Until recently [2], in situ monitoring of the growing interface has been performed mainly using electron diffraction techniques, even at relatively high background pressure [3]. Unfortunately, quantitative analysis of the electron scattering is hampered by the fact that the kinematical description does not apply, unlike in the case of X-rays. The study of crystal growth using surface sensitive X-ray scattering techniques is a field that has gained much interest over the past years [4, 5]. Combining the high-brilliance synchrotron X-ray beams, nowadays readily available at third generation sources, with sample chambers allowing for grazing incidence geometry, opens the possibility to study the growing interface or surface at an atomic scale. Here we present the design of a chamber for studying in situ the PLD process using synchrotron X-rays.

4.2 Requirements and present design

Three different parameters play an important role in the PLD process: substrate temperature, oxygen background pressure and the laser fluence. In the case of growth

of complex oxidic materials, like ferroelectrics and high-T_c superconductors, the substrate temperature is typically 800 °C and the oxygen background pressure is around 10^{-2} mbar. Since in some cases the oxygen content of the grown materials is not ideal at these high temperatures, the oxygen pressure in the chamber is increased to 1 bar during cool-down to room-temperature, in order to obtain the desired phase. The laser beam, having typically a wavelength of 248 nm, is focussed by a lense, resulting in a fluence of approximately 1.5 J/cm^2 in the focal spot on the target. In the present design, shown in figure 4.1, the laser enters the chamber through a fused silica window, that is fixed to the aluminium chamber wall, thereby hitting the target at an angle of 45 °. SXRD measurements are typically done at a fixed angle in the order of 1° of the X-ray beam with respect to the substrate surface. Since the measurements are performed with one point detector, during deposition only one reciprocal space point is being monitored at the time. Therefore deposition is interrupted after a number of monolayers, thereby allowing for movement of the diffractometer angles and detailed measurements of the grown film. The X-rays pass through the middle aluminium part, where a cylindrically shaped strip of 27 mm height is thinned to a thickness of 0.5 mm, in order to minimize absorption. The opening angles achievable in this way are 0 to 20 degrees for the incoming and outgoing beam with respect to the surface and 310 degrees for rotation around the surface normal. The choice of geometry when monitoring the diffracted intensity during deposition is free, i.e. both in-plane or out-of-plane reflections can be chosen. By use of two rotary feed-throughs in the cover lid, the target spindle and shutter axes are led into the chamber. The target is being rotated during deposition in order not to hit it at the same position with each laser pulse. Prior to deposition the shutter is placed between the substrate and target in order the clean the top most layer of the target by firing the laser a number of times without depsositing material on the substrate. The heating element consists of a coil-shaped thermocoax resistor wire embedded in a Ni heater block, which is non-reactive in an oxygen environment. The substrate is attached to the heater, using Cerastil ceramic glue. At 800 °C and ambient pressure the total power used by the heater is 85 W. Under these demanding conditions, the chamber was tested for thermal loss, showing that the cover lid reaches a temperature of 60 °C while the other walls only heat up to 40 °C.

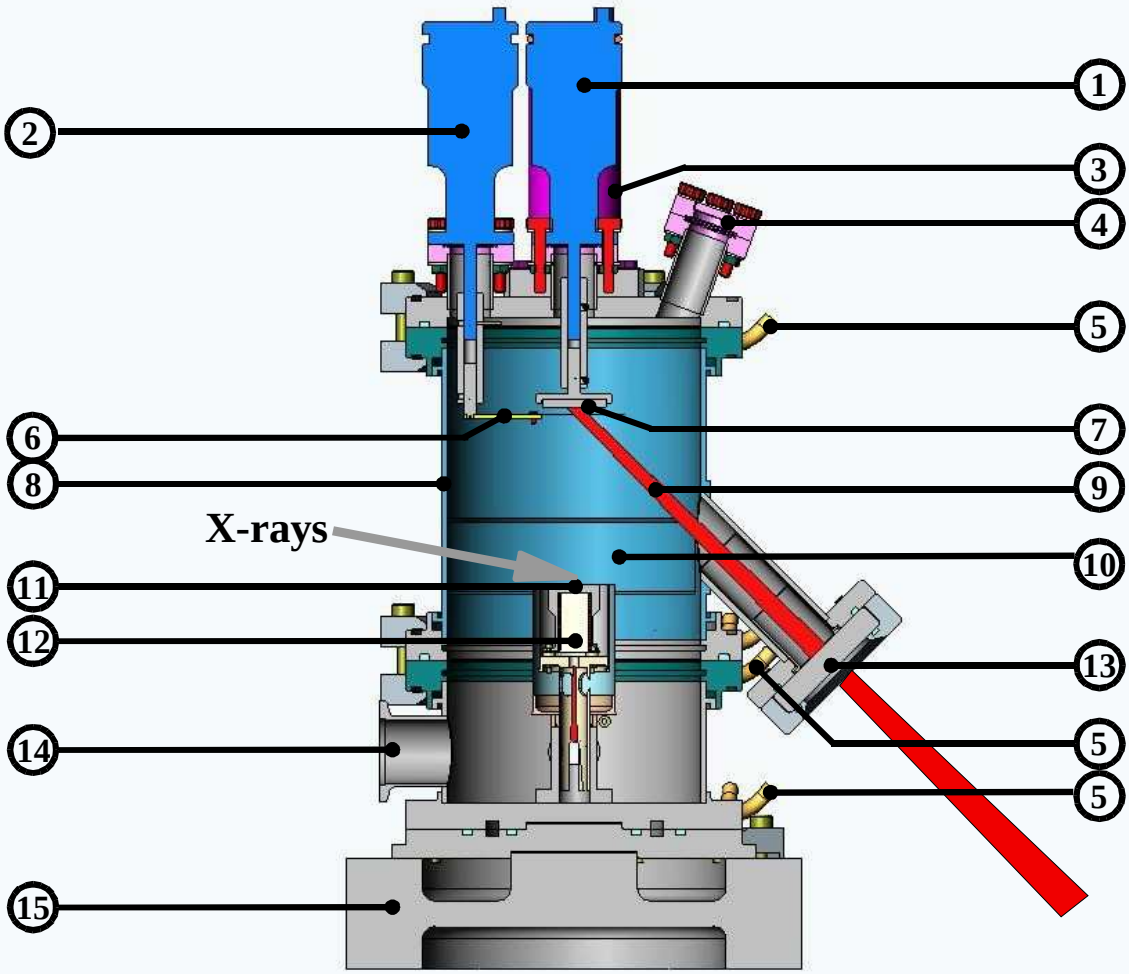

Figure 4.1: Cross-sectional view of the sample chamber. The height from base plate to top lid is 260 mm, the diameter of the middle part is 140 mm. 1. Feedthrough for target spindle. 2. Feedthrough for pre-ablation shutter. 3. Electro-motor for target spindle. 4. Viewport. 5. Water-cooling connections. 6. Pre-ablation shutter. 7. Target. 8. Aluminium chamber wall. 9. Laser beam. 10. Thinned part of aluminium wall (0.5 mm). 11. Substrate position. 12. Resistive wire heater embedded in nickel heater block. 13. Fused silica laser window. 14. Vacuum pump connection. 15. Base plate (d=150 mm).

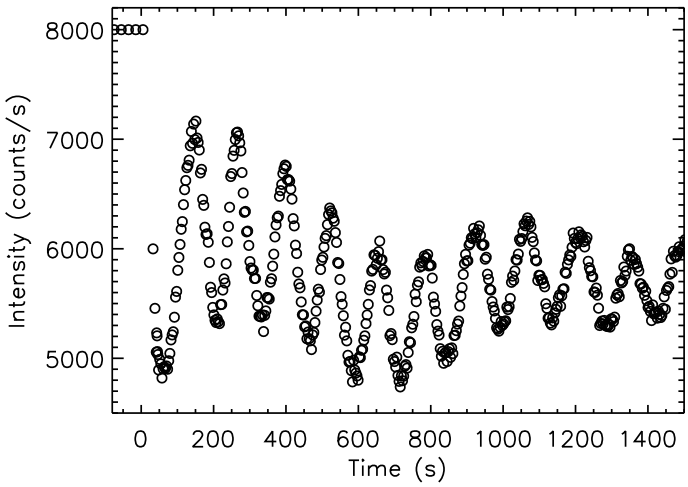

Figure 4.2: Intensity oscillations for the homoepitaxial deposition of $SrTiO_3$. Clearly growth proceeds in a layer-by-layer fashion. Upon completion of a monolayer the intensity goes to a maximum. Due to surface roughening the intensity decreases. For clarity, the intensity prior to deposition is shown too. During the first few laser shots the X-ray shutter was still closed.

4.3 Applications

The chamber has been used in combination with an excimer laser (KrF 248 nm, Lambda Physik EMG 103) for the homoepitaxial deposition of $SrTiO_3$. The laser beam is focused down to about 3 mm^2 by a lense, resulting in a laser fluence of 2 J/cm^2 on the target. X-ray diffraction experiments, using a wavelength of 0.775 Å, were performed in situ, by mounting the chamber on a 2+3 type surface diffractometer [6], on BM26 (Dubble) [7] at the European Synchrotron Radiation Facility (ESRF). Figure 4.2 shows the measured intensity oscillations of the specularly reflected X-ray beam at an angle of incidence of 1°. Each maximum in figure 4.2 corresponds to the completion of another monolayer of the material, and this kind of oscillations is a clear signature for layer-by-layer growth.

4.4 Conlusion

A sample chamber for the purpose of studying the PLD process in situ with surface sensitive X-ray scattering, is successfully tested and implemented at a synchrotron beamline. The very first results show that it is possible to follow the evolution of the $SrTiO_3(001)$ surface, during layer-by-layer growth up to many monolayers. This opens the possibilities to do detailed studies of crystal growth using PLD and to profit from the resulting quantifiable data using kinematical description of X-ray scattering.

References

[1] D. B. Chrisey, G. K. Hubler (Eds.), *Pulsed laser deposition of thin films*, John Wiley & Sons inc., 1994.

[2] G. Eres, J. Z. Tischler, M. Yoon, B. C. Larson, C. M. Rouleau, D. H. Lowndes, P. Zschack, Appl. Phys. Lett. **80** (2002) 3379.

[3] A. J. H. M. Rijnders, G. Koster, D. H. A. Blank, H. Rogalla, Appl. Phys. Lett. **70** (1997) 1888.

[4] G. Renaud, Surf. Sci. Rep. **32** (1998) 1–90.

[5] E. Vlieg, Surf. Sci. **500** (2002) 458–474.

[6] E. Vlieg, J. Appl. Cryst. **31** (1998) 198.

[7] M. Borsboom, W. Bras, I. Cerjak, D. Detollenaere, D. G. van Loon, P. Goedtkindt, M. Konijnenberg, P. Lassing, Y. K. Levine, B. Munneke, M. Oversluizen, R. van Tol, E. Vlieg, J. Synchr. Rad. **5** (1998) 518.

Chapter 5

$YBa_2Cu_3O_{7-x}$ Growth Studies

5.1 Introduction

In this chapter, the results of growth studies on $YBa_2Cu_3O_{7-x}$ thin films by pulsed laser deposition on $SrTiO_3(001)$ substrates are given. By the use of high intensity X-rays, available at third generation synchrotron sources, it is in principle possible to study simultaneously the surface morphology, atomic structure and strain state *during* growth and conditioning of pulsed-laser-deposited thin films. In the following paragraphs, first a brief introduction into some physical and chemical properties of the system $YBa_2Cu_3O_{7-x}$, will be given. Next the details and the results of three different experiments are described and discussed in view of earlier results. Finally, the stability of ultra-thin films is discussed after which conclusions regarding the method in general and growth of $YBa_2Cu_3O_{7-x}$ particularly are given.

5.2 $YBa_2Cu_3O_{7-x}$

The discovery of superconductivity in the La-Ba-Cu-O system with a transition temperature $T_c \approx 35$ K, by Bednorz and Müller in 1986 [1] (Nobel Prize 1987), led to a worldwide quest for materials with even higher transition temperatures [2]. The layered copper oxide materials were soon called High-T_c superconductors. It was the group of Chu *et al.* that found a $T_c \approx 92$ K for $YBa_2Cu_3O_{7-x}$ in 1987 [3]. With this discovery an important barrier was broken: a T_c well above the boiling point of liquid nitrogen (77 K). Up to that time, cooling was performed mainly using liquid helium, which is relatively expensive. The ability to cool with nitrogen paved the way for more applied superconductivity. Nowadays, many more compounds with a T_c above

90 K are known, most of which belong to the family of layered copper oxides ReBCO (Re=rare earth, B=barium, C=copper and O=oxygen) [4]. Nevertheless, finding a material that is superconducting at room temperature still is one of the 'Holy Grails' in physics, and the search continues.

5.2.1 Crystal structure and physical properties

The properties and crystal structure of $YBa_2Cu_3O_{7-x}$ (YBCO), shown in fig. 5.1, depend crucially on the oxygen deficiency [5]. With x changing from 1 to 0, the ground plane oxygen orders, and a whole series of different (super)structures can be identified [6, 7, 8, 9, 10], rendering either a tetragonal or orthorhombic crystal structure. This ordering manifests itself in oxygen preferentially occupying the site in the bc-plane at $z = 0$, thereby forming CuO-chains along the b-axis [11]. Furthermore, the ordering is dependent on the temperature, which is discussed in more detail in chapter 6. In the case of oxygen ordering, the a and b axes are no longer identical and the structure is orthorhombic. YBCO is however not superconducting in the tetragonal phase and with increasing oxygen content T_c increases [12]. Thin films of YBCO are typically synthesized at high temperatures in the tetragonal phase, which imposes a post-annealing process in an oxygen environment to obtain an optimum oxygen content[1]. During this process the thin film crystal structure undergoes a tetragonal-to-orthorhombic phase transition.

It is known that the layered structure of copper oxide planes and the ordering of oxygen into chains result in anisotropic physical properties. As a function of temperature, the normal-state resistivity shows semi-conductor behaviour in the c-axis direction and metallic behaviour in the ab-plane [14]. On theoretical grounds it is also expected that in the superconducting state the supercurrent flows mainly in the ab-plane [15]. More recent experiments provide evidence for anisotropy of the supercurrent, exhibiting d-wave symmetry in the ab-plane [16, 17]. The anisotropic properties require that for application of these layered materials in thin films the ab-planes lie in the surface plane, or in other words, require so-called $c-$axis growth [18].

[1] In the case of pulsed laser deposition it has been found that YBCO thin films are substantially oxidized ($x < 0.5$), even without a post-annealing process in 1 bar of oxygen [13].

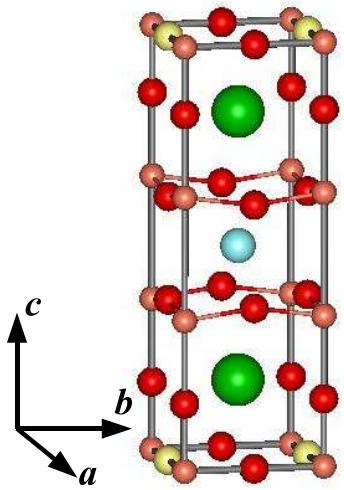

Figure 5.1: Unit cell of $YBa_2Cu_3O_{7-x}$. The seventh oxygen, which is situated in the ground plane, occupies either the $(\frac{1}{2}, 0, 0)$ (light color) or $(0, \frac{1}{2}, 0)$ (dark color) position. In the tetragonal phase both positions are equally occupied, and the a and b axes are identical. If however the oxygen preferentially occupies the, by convention, $(0, \frac{1}{2}, 0)$ position, the structure is orthorhombic. This oxygen ordering is dependent on x and the temperature.

5.2.2 Crystal chemistry

Bulk YBCO is usually prepared via a solid state reaction at 950°C, utilizing as initial constituents Y_2O_3, CuO and $BaCO_3$ [3, 18]. The poly-crystalline target material used for thin film growth by PLD, is made in the same way. The plasma formed during ablation, does not consist of the desired phase, but of a variety of sub-oxide clusters [19]. Therefore, the thermodynamic conditions at the surface must be optimized for the formation of YBCO. As a function of temperature and oxygen partial pressure, the following reaction is important in the formation process of YBCO [20]:

$$2YBa_2Cu_3O_6 \rightarrow Y_2BaCuO_5 + 3BaCuO_2 + Cu_2O \tag{5.1}$$

This reaction describes the transition from Y123 to Y211, of which the latter is dubbed the "green phase" owing to its colour, and where the numbers relate to the number of Y, Ba and Cu atoms in the structure respectively. Since the Y211 phase is not superconducting, it is obvious that it has to be prevented from forming. In addition to the thermodynamic conditions to form the desired phase, two other important aspects rely on the growth conditions as well. First of all, the growth direction. As

mentioned before, the YBCO film c-axis should be parallel with the substrate surface normal. It was found that at substrate temperatures lower than 500 °C mixed a and c-axis growth occurs on $SrTiO_3(001)$ substrates [21]. Second, to promote layer-by-layer growth during PLD, which results in smooth film surfaces, the substrate temperature should be sufficiently high, since the mobility of adatoms/clusters is thereby enhanced. All these factors together result in the optimum growth conditions[2] $P_{O_2} \simeq 10^{-1}$ mbar and a substrate temperature $T_{sub} = 780°C$.

5.3 Experimental

The experiments were carried out using the PLD chamber, described in chapter 4 [22], which was mounted on a 2+3 type surface diffractometer with vertical scattering geometry at BM26 (DUBBLE) [23] at the European Synchrotron Radiation Facility (ESRF). The X-ray beam was monochromatized to a wavelength of 0.775(1) Å. Optically polished $SrTiO_3$ (001) (spacegroup $Pm\bar{3}m$ with a=3.901(1) at room temperature [24]) substrates were obtained from Surfacenet GmbH, Rheine, Germany. A special treatment of these substrates results in single TiO_2-terminated surfaces [25]. A sintered pellet of $YBa_2Cu_3O_{7-x}$ (YBCO, spacegroup Pmmm with $a = 3.832(1), b = 3.887(1), c = 11.680(1)$ and $x \simeq 0.05$ at room temperature [26]) was used as a target. During deposition the substrate temperature was kept at 780°C, while the oxygen pressure in the chamber was 0.1 mbar, which are the proper conditions for YBCO c-axis growth as described in the previous section. The KrF excimer laser beam (Lambda Physik EMG101) was focused, resulting in approximately a fluence of 1.5 Jcm^{-2} in the focal spot on the target. In order to obtain sufficient statistics of the diffracted signals, the laser repetition rate was set in the range 0.25-0.5 Hz, thereby allowing to count two to four seconds per laser pulse.

5.4 Results and discussion

Here, the results of three different experiments of heteroepitaxial growth of YBCO on STO are described. In all experiments, at a grazing angle of 1.0 degree for the incoming X-ray beam, the intensity of approximately the reciprocal point *(0,0,0.175)*

[2]The oxygen pressure in the deposition chamber has a strong effect on the plasma. See chapter 1 for more details.

in STO lattice units was monitored during deposition. Interrupting the deposition allowed for measurement of the reflectivity, providing information about the c-axis, total film thickness and, to a certain extent, the film roughness.

During layer-by layer-growth of thin films, several phenomena can be identified: increasing film thickness, cycling between smooth and rough film surfaces and structural evolution of the thin film with increasing film thickness, which manifests itself in strain relaxation. In the following sections, three different experiments are described, each focusing on one of the aforementioned aspects of thin film growth by PLD.

5.4.1 First experiment

In the first experiment, the substrate had a miscut of 0.38(5)° in approximately the [210] direction. This value is obtained from the orientation matrix of the substrate, whose surface normal was aligned along the principle sample rotation axis. An alternative method for determining the miscut angle without use of the orientation matrix, is given in appendix A. In fig. 5.2 the intensity growth oscillations (see section 2.5) are shown together with the reflectivity ridge scans when deposition was temporarily stopped. Finally, after the last deposition run, the sample was cooled to room temperature in an oxygen-rich environment. Subsequent resistance measurement as a function of temperature showed a superconducting transition temperature T_c of about 85K.

5.4.1.1 Epitaxial relationship

The angle between the c-axes of film and substrate (α) is deduced from the angular positions of several reflections, as described in appendix A. As a consequence of the particlar scattering geometry in which the measurements were performed here, it is of crucial importance to align the reflections very precisely in all diffractometer angles before using them in the procedure to determine the angle α. For small scattering angles, the diffractometer angle that moves the detector in the vertical plane (δ) has a large effect on the value obtained for α. In order to determine α with an accuracy of about 0.1 degrees, δ has to be determined with an accuracy of 0.01-0.02 degrees. Since the reflections were not always centred with the required precision in all diffractometer angles, the angle α can not be determined for each stage during growth. Nevertheless, the results for the very first deposition run and after cool down

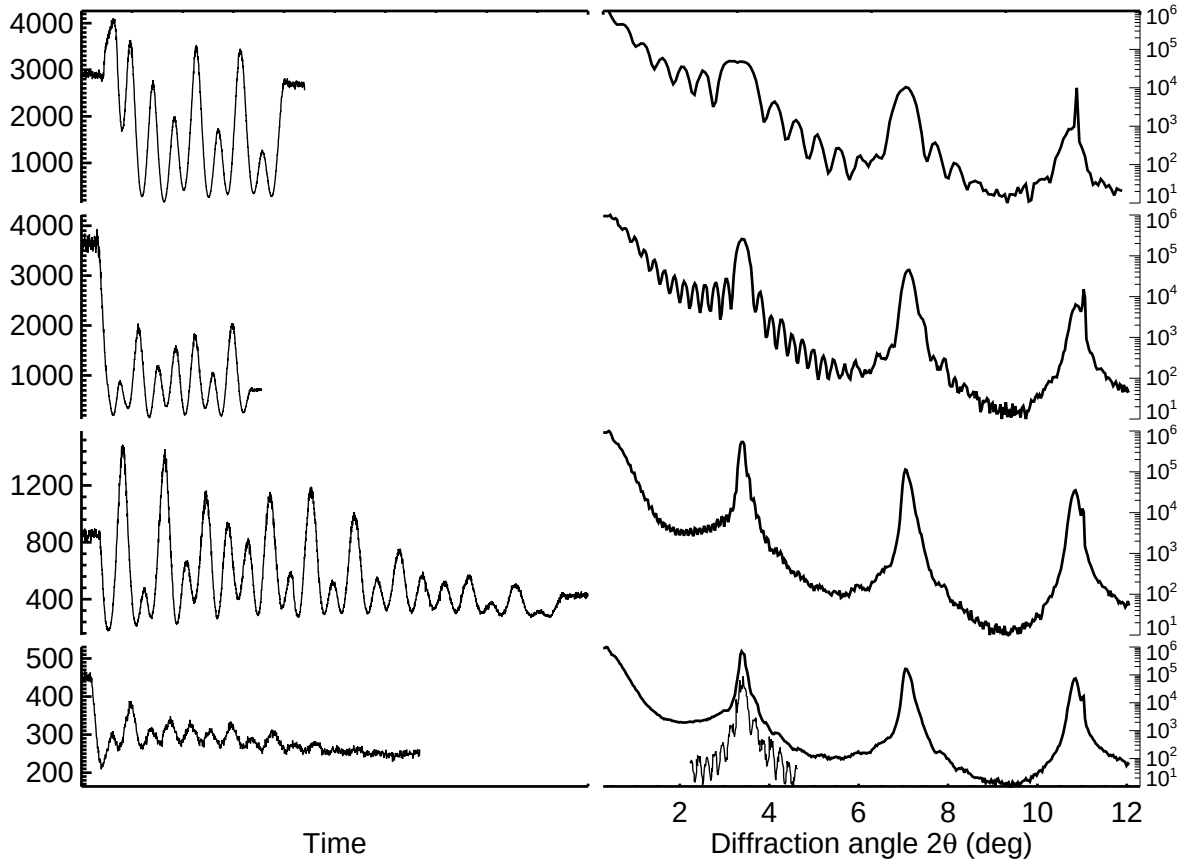

Figure 5.2: Diffraction measurements during and in between subsequent deposition runs of YBCO on STO for the first experiment. (left) Intensity oscillations during the deposition runs, measured at a grazing angle of 1.0 degree of the incoming X-ray beam with respect to the surface. The top left shows the measurements during the first deposition run on the bare STO substrate. The intensity oscillations during subsequent deposition runs are shown in the left graphs from top to bottom. (right) Scans along the *00l* direction measured after each of the deposition runs, of which the intensity growth oscillations are shown in the left graphs. With increasing film thickness, the Kiessig fringes appear closer together. The sharp feature at 11.2 degrees, is the *001* substrate reflection. In the lower right part the *001* YBCO reflection from another measurement on the same film is inserted. For clarity, the angular scale of this inserted reflection is extended by a factor 2.5 compared with the upper curve and the position and intensity are scaled to position it just under the *001* of the upper curve. The pronounced Kiessig fringes allowed for a thickness determination.

♯ maxima	thickness (Å)	c-axis (Å)	♯ layers	α (deg)
9	96(1)	11.91(5)	8.1(1)	0.1(1)
17	192(1)	11.95(4)	16.1(1)	-
38	448(1)	12.0(1)	37.3(4)	-
52	610(4)	12.0(1)	50.8(5)	-
-	605(11) [a]	11.716(2)	52(1)	0.1(1)

[a] Measured after cool down to room temperature.

Table 5.1: Structural parameters of a YBCO film during growth, determined from the data shown in fig. 5.2.

of the full grown film, seem to indicate that the orientation did not change during growth.

5.4.1.2 Thickness control

From the diffraction measurements, shown in figure 5.2 the c-axis length and total film thickness are determined. These are listed together with the number of observed growth oscillations and the calculated number of unit cell layers in table 5.1.

Disregarding substrate and defect scattering, the specularly diffracted intensity of a thin film is described by (see also section 2.3):

$$I \propto \frac{\sin^2(Nq_zc/2)}{\sin^2(q_zc/2)}. \tag{5.2}$$

This function has local maxima for those values of q_z where the denominator goes to zero, i.e. the Bragg points (see also section 2.3). The numerator is a function that, for $N > 1$, has a smaller period in reciprocal space than the denominator and describes the well-known Kiessig fringes [27]. From equation 5.2 the thickness follows from determining the distance between the positions where the nominator goes to zero, or to a maximum, resulting in:

$$t = Nc = \frac{\lambda}{2\cos(\theta)\Delta\theta} \tag{5.3}$$

with λ the X-ray wavelength, c the c-axis lattice parameter, θ the Bragg angle and $\Delta\theta$ the angular separation between the Kiessig fringes. The diffraction pattern can in general be devided in two regions, the low and high angle side [28]. In the low angle

region, the average electron density is probed, thereby giving the total film thickness. In the high angle region, the atomic structure becomes important, and fringes in this region arise from diffracting from a finite repeating lattice. In the present case, the boundary between the low and high angle region can be defined around the *001* YBCO Bragg peak, which is around $2\theta = 3.6°$. Since the film thicknesses listed in table 5.1 are mainly determined from Kiessig fringes in the high angle regions of the subsequent diffraction spectra, the results give the thickness of the repeating YBCO unit cell[3]. Using the above considerations to explain the discrepancy between the observed number of growth oscillations and the calculated number of unit cell layers, shown in table 5.1, leads to the hypothesis that the first two smooth layers deposited on the STO substrate together form one complete unit cell of YBCO. Within the error bar, the number of observed growth oscillations is systematically one larger than the number of unit cell layers YBCO deduced from thickness and c-axis length measurements. This is also concluded by comparing the time needed to deposit the first two and subsequent smooth layers. Assuming that the deposition rate (monolayers/s) does not change too much during growth[4], the first two smooth layers together were deposited in about 4/3 of the time of the subsequent layers. It has been shown previously that the initial growth of YBCO proceeds in perovskite-type (Y,Ba)CuO_{3-x} blocks which are a third of the size of the bulk unit cell [29]. The results here indicate that indeed the very first layer on the substrate does not consist of the complete bulk unit cell Y123, possibly formed by four perovskite-type blocks. The exact shape of the first intensity oscillation will depend on the nucleation and atomic structure of this first monolayer. Unfortunately, the current data do not allow to determine this structure, a point that will be discussed in more detail in section 5.5.

5.4.1.3 Dynamics during growth

The intensity growth oscillation in figure 5.2 show a number of details that give information about the growth dynamics. As described in the previous section, each

[3]The low angle regions of the diffraction spectra given here, show that the periodicity of the fringes is indeed smaller. Unfortunately, the measurements are not accurate enough to determine the complete film thickness from the low angle region. Attempts to use the program SUPREX [28] to extract the film thickness did not give a satisfying result for the present data.

[4]Due to passivation of the KrF gas in the laser, the laser power decreased gradually with time. This required to refill the laser gas several times during this experiment.

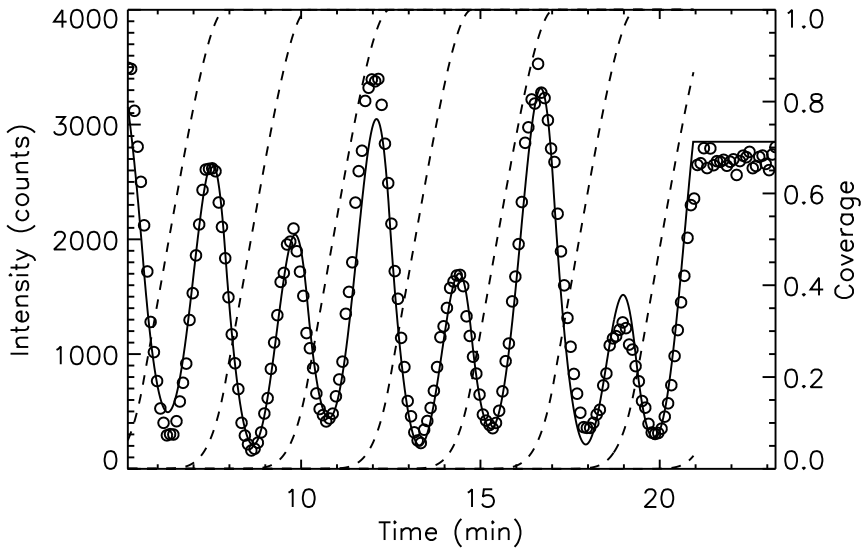

Figure 5.3: Intensity growth oscillations during deposition of YBCO on STO. The data (open circles) used here are the part from the second intensity maximum of the first deposition run as shown in the top left spectrum of figure 5.2. The fit obtained by using a model as described in the text renders the coverage of each layer as a function of time (dotted lines) and results in the calculated intensity (solid line).

intensity maximum corresponds to the addition of one unit cell layer YBCO, except the very first two just after starting growth on the bare substrate. In order to extract the temporal structure evolution of the film during deposition, a distributed growth model, much like that of Cohen *et al.* [30] is used to describe the intensity oscillations quantitatively. Within this model, the coverage of a layer is evaluated as a function of time. If growth proceeds in a layer-by-layer fashion, as described in section 1.3.2, a certain level starts to grow only when the level below is (almost) fully occupied. In other words, as long as a level j is not fully occupied, all the material that arrives at level $j+1$ will diffuse down to level j. Figure 5.3 shows the results for the first deposition run starting from the second intensity maximum, of which the data are presented in the left top part of fig. 5.2 as well. The first two intensity maxima were not taken into account, because the structure during the initial deposition is unclear as described in the previous section. The coverage θ of the j-th layer as a function of time is found by solving the following set of coupled differential equations:

$$\frac{d\theta_j}{dt} = (1-\lambda_{j-1})\frac{1}{\tau}(\theta_{j-1}-\theta_j) + \lambda_j\frac{1}{\tau}(\theta_j-\theta_{j+1}) \tag{5.4}$$

with τ the time needed to deposit a complete monolayer and λ_{j-1} and λ_j describe the fractions of material that diffuse from level j to $j-1$ and from level $j+1$ to j, respectively. These parameters λ that describe the interlayer mass transport are made time-dependent by using the following relation [31]:

$$\lambda_j = 1 - \exp\left(\frac{-\alpha\sqrt{\frac{1}{2}-|\theta_{j-1}-\frac{1}{2}|}}{\theta_{j-1}}\right) \tag{5.5}$$

with α a parameter describing the interlayer mass transport. When $\alpha \to \infty$ there is perfect layer by layer growth, for each layer $\lambda_j = 1$ which means that all the material that arrives at a certain level will diffuse to the level below. The other extreme case, $\alpha = 0$ results in Poisson growth, where for each layer $\lambda_j = 0$, which means that there is no interlayer mass transport. For finite values of α there will be some intermediate layer-by-layer growth. The difference with the model used by Van der Vegt *et al.* [31] is that the interlayer mass transport is made level independent. The coverages of each layer as a function of time are used to calculate the scattered intensity by using:

$$I(l,t) = s\left|F_0|e^{i\phi_0} + \sum_{j=1}^{n}\theta_j(t)F_{ybco}(l)e^{i2\pi lj}\right|^2 + I_{bg} \tag{5.6}$$

with l the diffraction index, s a scale factor, $|F_0|$ and ϕ_0 the modulus and phase of the initial structure factor respectively, $F_{ybco}(l)$ the structure factor of YBCO and I_{bg} a constant X-ray background. Equation 5.6 is used to fit four independent parameters to the intensity oscillations shown in the top left spectrum of figure 5.2. The results are listed in table 5.2. The structure factor of YBCO is calculated using bulk atomic positions obtained from an electron density study [26]. By fitting the unkown initial structure factor F_0, the problem of the crystal structure during the very first two oscillations is circumvented. For the present purpose of obtaining a picture of the temporal structure evolution of the thin film, this approximation is justified. The problem of the initial atomic interface structure of YBCO on STO will be discussed in more detail later on in this chapter. The value $\alpha = 3.38$ derived from the fit is an indication that there is substantial interlayer mass transport. Another way of interpreting the current result is by calculating the maximum number of layers

parameter	value
s	0.49(5)
$\|F_0\|$	88.1(6)
ϕ_0	−1.42(6)
α	3.38(5)
τ(s)	137.3
l	0.536
I_{bg}(counts)	200

Table 5.2: Parameters obtained from fitting the distributed growth model as described in the text to the experimental data of the first deposition run of YBCO on STO. The parameters originate from equation 5.6. The three parameters listed below the line were kept fixed in the fit.

that grows simultaneously as a function of α. This is shown in figure 5.4, which was obtained by determining the maximum number of layers having at the same time a coverage between 0.01 an 0.99. This was done for several values of α and results that in the present case ($\alpha = 3.38$) during deposition maximally two layers grew at a time.

5.4.2 Second experiment

In the second experiment, the substrate had a miscut of about 0.1° in approximately the [210] direction. Shown in fig. 5.5 are the reflectivity ridge scans for three different layer thicknesses. The first scan is for a thickness thickness of approximately 5 unit cell layers YBCO. Upon subsequent deposition of more material, the intensity of the *(0,0,0.55)* reciprocal space point in YBCO lattice units is monitored. Deposition was stopped when reaching a maximum and the reflectivity scan was performed. Next, deposition was continued and stopped when reaching a minimum of the *(0,0,0.55)*. Again the reflectivity was measured.

5.4.2.1 Roughness evolution

Again the shape of the resulting diffraction patterns can be explained by equation 5.2, that is in a first approximation without taking into account substrate scattering or the functional form of the YBCO structure factor as a function of diffraction angle. In the case of N completely smooth unit cell layers, there will be $N-2$ Kiessig fringes

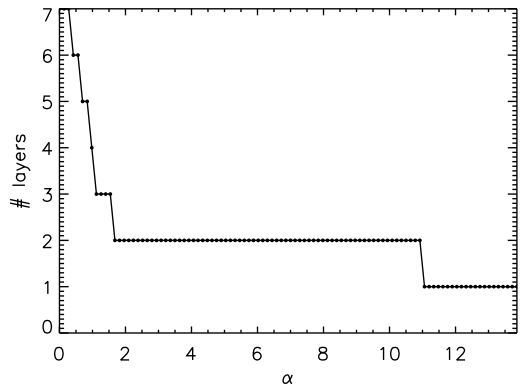

Figure 5.4: Maximum number of layers that grows simultaneously as a function of α as defined by equation 5.5. The values plotted here are determined by using cut-off values of 1%, that is, a layer is assumed to grow as long as its coverage is between 0.01 an 0.99. The present graph is not very reliable for values $\alpha < 0.5$ because the value at $\alpha = 0$ will depend on how many layers are evaluated in the simulation, which for the present case was seven.

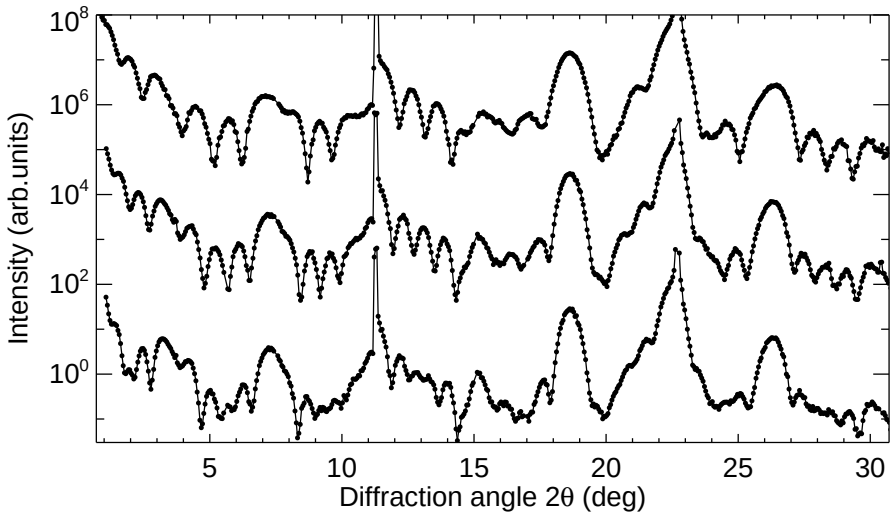

Figure 5.5: Diffraction patterns along the $00l$ direction of a YBCO film. Shown are the initial scan (top) of approximately 5 unit cells YBCO, after adding one more monolayer (middle) and depositing half a monolayer more (bottom). For clarity the top and bottom curves are multiplied by a factor of 10^3 and 10^{-3} respectively. The sharp peaks at 11.2 and 22.3 degrees are the substrate *001* and *002* reflection respectively.

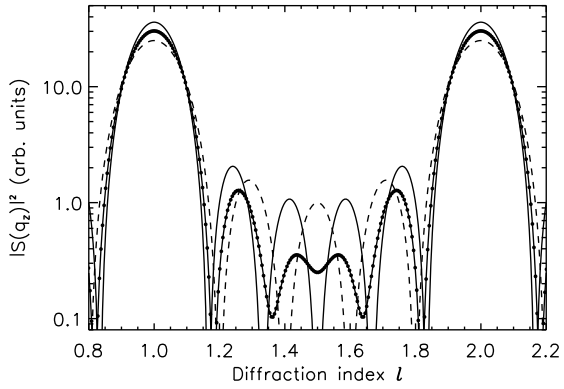

Figure 5.6: The two-level interference function of equation 5.7. Shown are $|S_1|^2$ with $N = 5$ (dashed) , $|S_2|^2$ with $N = 6$ (solid) and the interference $|\frac{1}{2}S_1 + \frac{1}{2}S_2|^2$ (filled circles). Clearly the contrast $\frac{I_{max}-I_{min}}{I_{max}+I_{min}}$ changes drastically half way the Bragg peaks.

in between two neighbouring Bragg peaks. So when growing one extra unit cell layer, one extra Kiessig fringe appears between the Bragg peaks. This is seen when going from the top to the middle diffraction profile in fig. 5.5. When depositing half a unit cell layer more, the diffraction profile is built up of two contributions, shown in fig. 5.6 and given by:

$$I(q_z) \propto |\frac{1}{2}S_1(q_z) + \frac{1}{2}S_2(q_z)|^2 = |\frac{1}{2}\frac{1-\exp(iNq_zc)}{1-\exp(iq_zc)} + \frac{1}{2}\frac{1-\exp(i(N+1)q_zc)}{1-\exp(iq_zc)}|^2 \quad (5.7)$$

The slight difference in periodicity of the two contributions, S_1 and S_2, results in the washing out of fringes, which is most pronounced half way the Bragg peaks. By defining a fringe contrast as the relative intensity difference between a maximum and neighbouring minimum as $(I_{max} - I_{min})/(I_{max} + I_{min})$, roughness can be interpreted in the following way. In the absence of crystal truncation scattering and noise, the interference function 5.7 renders a fringe contrast of 1 for perfectly smooth surfaces, because in the minima $I_{min} = 0$. As the roughness increases, the fringes wash out, i.e. $I_{max} \approx I_{min}$ and the fringe contrast goes to zero. This is seen in the bottom diffraction pattern of fig. 5.5 and simulated in fig. 5.6 for a two-level system. The dependence of the fringe contrast on scattering angle also becomes obvious from fig. 5.6. At the anti-Bragg positions, the diffraction pattern is most sensitive to surface

roughness, thereby decreasing the fringe contrast most (see also section 2.4.2). If even more roughness were present, this could be modelled by summing in eq. 5.7 over more terms S_i, each representing a column of N_i unit cell layers. For many of these terms the fringes would disappear completely as they will for large N, i.e. a thick crystal (see also section 2.3).
The results here indicate that the Kiessig fringe contrast is extremely sensitive to the surface roughness. The surface cycles between rough and smooth during deposition, which can be followed by X-ray diffraction. By use of the crystal shape function, the number of Kiessig fringes between two Bragg reflections can be used to determine the film thickness. However, the crystal shape function is modified by the slowly varying structure factor with diffraction angle, which in the present case makes that some of the Bragg reflections are not very clear.

5.4.3 Third experiment

In the third experiment, the miscut angle of the substrate was determined to be 0.22(8) degrees in approximately the [110] direction. Intensity oscillations in the specularly diffracted X-ray beam during deposition are shown in fig. 5.7.

The deposition was interrupted several times, for characterization of the grown film. Figure 5.8 shows scans along the $00l$ direction of Bragg reflections of the film at three different thicknesses. The pronounced Kiessig fringes allow for an accurate determination of the thickness, as described in section 5.4.1.2. The out-of-plane lattice parameter of the film is obtained from the angular positions of several Bragg peaks and when comparing them with the angular positions of the substrate reflections, their relative orientation is determined. The angle between the c-axes of film and substrate, α, and their lengths are shown together with the resulting film thickness in table 5.3.

5.4.3.1 Post-annealing

The deposition was stopped after approximately 34 monolayers, and the oxygen pressure was increased to 1 bar after which the sample was cooled to room temperature. Two reflections, of types *hhl* and *00l* were followed during the conditioning. The resulting c-axis and average in-plane $\bar{a} = \frac{1}{2}(a+b)$, both determined from the angular positions of the two measured reflections, as a function of temperature are shown in figure 5.9. Since following the reflections required constant re-centring, because of

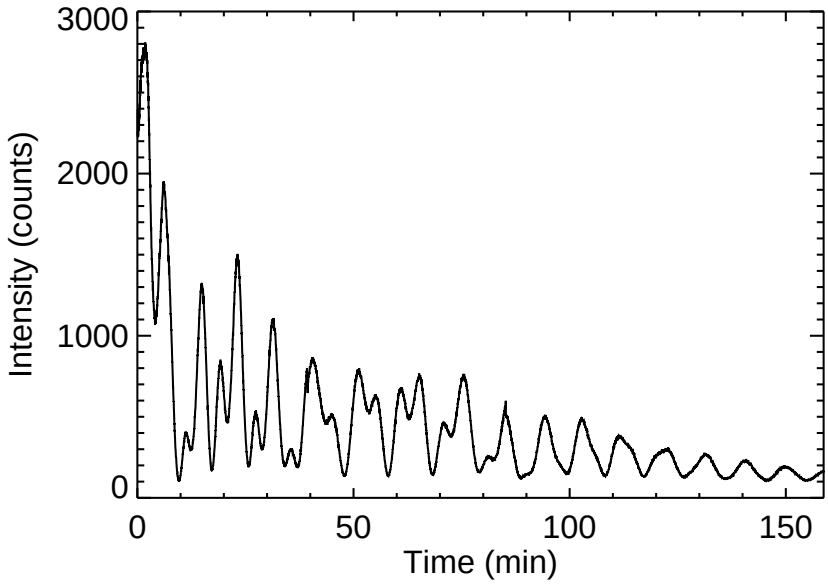

Figure 5.7: Intensity oscillations of approximately the (0,0,0.156) reciprocal space point in STO lattice units. Each maximum corresponds to the completion of another monolayer.

♯ maxima	thickness (Å)	c-axis (Å)	♯ layers (-)	α (deg)
10	108(1)	12.05(4)	9.0(1)	0.1(1)
19	210(1)	12.04(1)	17.4(1)	-
27 (35[a])	419(2)	12.055(4)	34.8(2)	0.3(1)
-	382(8)[b]	11.710(3)	33(1)	0.2(1)

[a] Assuming that a doubling of intensity growth oscillation period occurred.
[b] Measured after cool down to room temperature.

Table 5.3: Structural parameters of the $YBa_2Cu_3O_{7-x}$ thin film at different stages of growth. The first column indicates the maximum obtained from fig. 5.7, and the fourth column the number of unit cell layers obtain from thickness and c-axis measurement ($N_{layers} = t/c$). The last column shows the angle α between the c-axes of the substrate and the film.

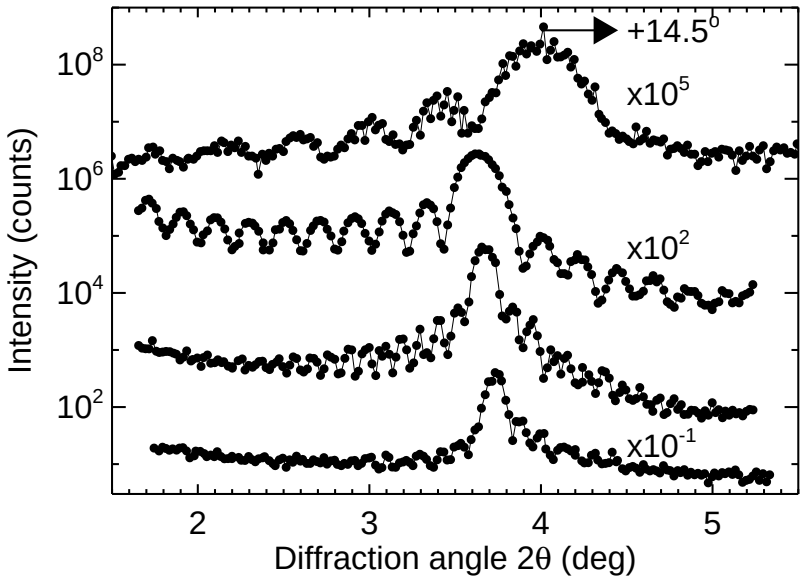

Figure 5.8: Kiessig fringes around Bragg reflections at different times during deposition. Shown are the *005* reflection for a 11nm (top), *001* for a 21nm (second from top) and *001* for a 42nm (second from bottom) film at deposition temperature. The *001* reflection after cool down to room temperature is also shown (bottom). For clarity the different diffraction profiles are displaced verically. In addition, the *005* (top) is shifted by 14.5 degrees to make it appear in the same range as the other profiles, which show *001* reflections.

thermal contraction of the heating stage, the cooling rate was chosen such that it took about three hours to revert to room temperature. It is expected that during cooldown the tetragonal-to-orthorhombic phase transition should take place. However, no anomalous changes in peak positions, indicative of a phase transition, can be deduced from figure 5.9. Furthermore, there is no change in peak-shape of the *hhl* reflection, which should occur due to the formation of twin domains, that accompanies the tetragonal-to-orthorhombic phae transition. A twinned YBCO crystal gives rise to the *hhl*-type reflections being split into three parts, however in the experiment described here the *hhl*-type reflection remained a single peak. Chapter 7 gives more details of the twinning mechanism for a fully oxygenated YBCO film and the resulting diffraction pattern.

The room temperature *001* Bragg reflection, shown in figure 5.8, shows some dis-

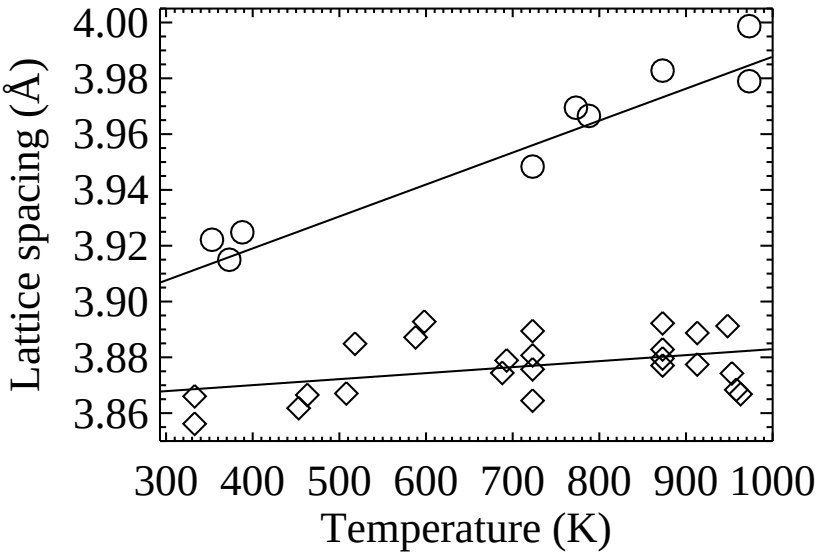

Figure 5.9: Evolution of the lattice parameters from deposition to room temperature of a 42nm thin YBCO film. Shown are values of $\frac{1}{3}c$ (circles) and the average in-plane $\bar{a}$ (diamonds) as a function of temperature. The lines are linear fits as function of temperature to the data and render the thermal expansion coefficients $\alpha_c = 30(3)\times10^{-6}$ K^{-1} and $\alpha_{\bar{a}} = 6(3) \times 10^{-6}$ K^{-1}.

tinct differences compared with the high temperature diffraction peaks. First of all, the position is shifted due to the thermal contraction and possibly a change in oxygen content, resulting in a different c-axis. Second, the fringe contrast decreased, which is an indication of surface roughening. Third, the integrated intensity diminished, which can be ascribed to a crystal quality degradation or to a change in crystal structure. All the aforementioned differences may arise from strain relaxation. Finally, when comparing the film thickness and c-axis of the film before and after cool down, it seems that the equivalent of approximately 2 unit cells disappeared. It might well be that the top part of the film oxidizes during cool down to form a different phase. Since the Kiessig fringes appear due to differences in the mean electron density, such a thin and different top layer would show up as an oscillation with a much larger period than those emerging from the thicker YBCO film.

The sample shows a reduced superconducting transition temperature T_c of 76 K,

indicating that the optimal oxygen deficiency of $x \simeq 0.05$ is not completely reached [11]. This might be due to a non-ideal post-annealing process. Usually the cool-down is done in two steps, where at 600 °C and 450 °C the cooling is stopped for 20-30 minutes, resulting in a total anneal time of about one hour [18]. In the present experiment the whole procedure took about three hours, with interrupts of 30 minutes at 600 °C and about one hour at 450 °C. Within the accuracy of determination, fluorescence data, taken during a Scanning Electron Microscopy (SEM) measurement by using an energy-dispersive detector, reveal no contaminating elements, which might account for a decrease of T_c as well. Chapter 6 gives a more detailed description of the (micro) structure of thin YBCO films as a function of temperature and oxygen partial pressure.

5.4.3.2 Epitaxial relationship

The orientation between film and substrate, indicated by angle α and listed in table 5.3 for different stages during growth, seems not to change during growth. However, the differences are about as large as the errors. Furthermore, α could not be determined at all stages of growth, because the reflections were not precisely enough aligned in all diffractometer angles (see appendix A for details about the calculation). Epilayer tilt is a phenomenon quite common in thin film heteroepitaxy [32, 33, 34, 35, 36]. Also for YBCO thin films, a change in epitaxial relationship between film and substrate with increasing film thickness, shown schematically in Figure 5.10, has been reported previously in ex-situ room temperature studies [37, 38] and is discussed in chapter 7 as well. The films used in those studies were thicker than 20 nm, whereas for 10 nm films no epitaxial tilt has been observed [39]. The epitaxial tilt could be formed by the introduction and subsequent alignment of dislocations at the interface and is therefore a consequence of strain relaxation [40]. It is well known in metallurgy, that upon alignment of dislocations in a plane, so-called low angle grain boundaries are formed [41]. A possible strain relaxation should be seen by a change in length of the out-of-plane lattice parameter as well. However, the data here are not accurate enough to show a significant difference with increasing film thickness (see Table 5.3).

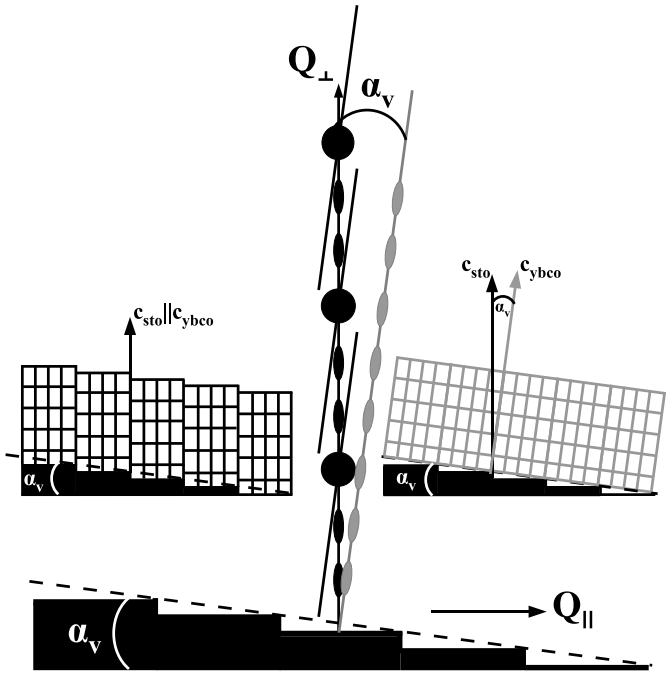

Figure 5.10: Schematic view of real and reciprocal space for the two epitaxial relationships between film and substrate. The substrate 00l peaks (black circles) lie on the $Q_\perp$-axis, and they are streaked (CTR's) along the direction that is perpendicular to the vicinal surface (dotted line). When the film c-axis is parallel to the substrate c-axis, the film Bragg peaks (black ellipses) lie on the $Q_\perp$-axis in between the substrate peaks. When the film c-axis is perpendicular to the vicinal surface, the film Bragg peaks lie in a direction (grey line and ellipses) that is tilted by the miscut angle, α_v, and no longer lie in between the STO Bragg reflections.

5.4.3.3 Doubling of oscillation period

Figure 5.7 has a number of details that give information about the growth dynamics. The distinct intensity oscillations clearly indicate layer-by-layer growth, much like in the first experiment described in section 5.4.1.2. Each maximum corresponds to the completion of a unit cell layer YBCO, except the very first two. It has been shown in section 5.4.1.3 that the pattern of intensity maxima alternating between a high and a low maximum can be adequately described by assuming almost perfect layer-by-layer growth of YBCO unit cell layers. However, in figure 5.7 it is seen that after around 85 min, where the film is about 20 nm thick, the period with which the oscillations occur doubles. From the resulting thickness and c-axis measurements, shown in ta-

ble 5.3, it is concluded that each subsequent intensity maximum corresponds to the deposition of two unit cell layers. Bearing this in mind, the results here (table 5.3) are consistent with the results presented in section 5.4.1.2: the number of observed intensity maxima is systematically one higher than the number of estimated unit cell layers YBCO [5]. Again this can be explained by assuming that the very first deposited smooth layer is not the Y123 phase. The intensity oscillation period doubling might indicate a change in the growing unit, i.e. upon depositing a double unit cell layer, the surface is smooth again. Similar behaviour has been observed in the case of growing superlattices containing $BaCuO_2$ (BCO) perovskite-type blocks by PLD [42, 43]. The reasoning used in those studies was that only units consisting of 2 blocks of BCO stacked on each other would be stable. However, it is not very likely that a double unit cell layer of YBCO becomes more stable than a single one *during* growth.

Another possible explanation for the intensity oscillation period doubling might be given by a non-uniform growth rate across the illuminated sample area. It is very plausible that indeed the deposition rate is not constant at each point of the sample. The resulting scattering pattern would then be the superposition of many intensity growth oscillation curves, each with a slightly different period. One distinct feature of the resulting intensity oscillations in such a case is that not only the intensity maxima but also the minima lie on an envelope, both of which converge to the same non-zero constant intensity [44, 45]. A non-uniform deposition rate over the surface area sampled by the X-ray beam, therefore, results in an intensity oscillation curve distinctly different from one arising from a multi-level growth front due to roughening, in which the minima remain zero [30]. However, in both the first experiment as well in the present, clearly the intensity minima do not increase too much during several deposition runs, which is an indication that the deposition rate may be assumed practically uniform over the illuminated surface area [46].

We propose an explanation without any of the previously two mentioned mechanisms for the doubling of the intensity oscillation period. The change in intensity oscillation period occurs at the thickness where possibly strain is relaxed and the epitaxial relation might change as discussed in section 5.4.3.2. To understand the in-

[5] With the exception of the second line of table 5.3 giving the results for the 19^{th} intensity maximum. The number of estimated unit cell layers is about half a unit cell layer less than the expected number. It is not certain whether deposition was stopped in an intensity oscillation maximum, because a non-integer number of unit cell layers would result in a rough surface and this in turn would not render such pronounced Kiessig fringes as seen in fig. 5.8 (see also section 5.4.2.1).

fluence of the epitaxial tilt on the measured diffraction signal, the scattered intensity in the case of a thin film on a substrate is considered by:

$$I(\mathbf{Q}) \sim |\sum_{j=-\infty}^{0} F_{sub}(\mathbf{Q}) e^{iq_z c_{sub} j} e^{\mu_{sub} j} e^{-\mu_{film} n} + \sum_{k=1}^{n+1} \theta_k F_k(\mathbf{Q}) e^{-iq_z c_{film} k} e^{\mu_{film}(k-n-1)}|^2, \tag{5.8}$$

where F is the structure factor, $\mathbf{Q} = (q_x, q_y, q_z)$, μ is the attenuation factor and θ_k the occupancy of the k-th film layer. The sums run over unit cell layers in the z-direction. The first sum results in the well-known Crystal Truncation Rod (CTR) [47] and does not change during growth except for some additional absorption by the film. The second sum results in the contribution to the scattering by the film, which is time-dependent. Upon completion of each freshly deposited monolayer ($\theta_k = 1$), the surface is smooth again and the intensity reaches a maximum. If the film were grown infinitely thick, i.e. when $n \to \infty$, due to the absorption the contribution by the substrate would vanish, and the sum over the film layers would result in a CTR, still oscillating with the period of one unit cell layer. However, equation 5.8 is valid only when the epitaxial relationship between film and substrate is such that there is perfect continuity of the substrate lattice, i.e. the contributions to the structure amplitude by substrate and film overlap in reciprocal space. In the case here, as suggested by table 5.3, the epitaxial relationship between film and substrate might have changed during growth. Therefore, when the film grows thicker than about 17 unit cell layers (after 85 min in fig. 5.7), the scattering is determined by the sum of the individual contributions by the substrate and film, which both peak at different positions. The effect on the specularly reflected intensity is shown in figure 5.11, using equation 5.8 with $\theta_k = \frac{1}{2} + \frac{1}{2}\tanh((t - t_k)/\tau)$, with t_k determining the time when layer k starts to grow and τ the deposition time per layer [48]. Up to 17 monolayers both sums from eq. 5.8 are added for $l_{STO} = 0.151$. From 17 monolayers onward only the sum over the film layers is calculated for $l_{YBCO} = 0.453$ and the scattering from the substrate is assumed as a constant background. Since the c-axes differ by a factor of three the distance to the origin of reciprocal space is the same for both points. Only the orientation of the sample differs in both cases and the difference is given by the miscut angle of the substrate (see figure 5.10). If in the simulation for the thicker film ($>$ 17 monolayers) the reciprocal space point were exactly at the anti-Bragg position of the film ($l_{YBCO} = \frac{1}{2}$), the maxima would

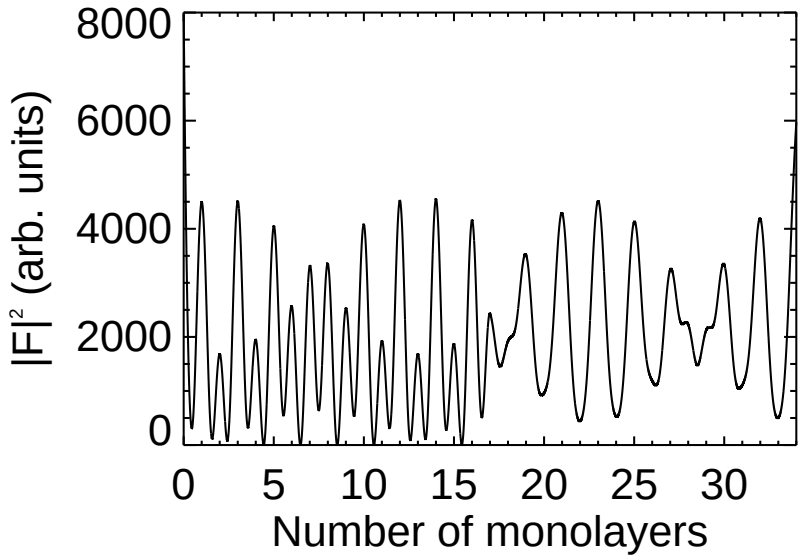

Figure 5.11: Simulated intensity oscillations during growth of a YBCO film on a STO substrate. At a coverage of 17 monolayers, the epitaxial relationship between film and substrate changes such that the scattering from both do not add coherently any more, resulting in a doubling of the oscillation period. The calculation is performed for the (0,0,0.177) reciprocal space point in STO lattice units, which is slightly off the anti-Bragg position $l_{YBCO} = \frac{1}{2}$ of the YBCO film.

occur exactly 2 monolayers apart. In the case of a thin crystal, i.e. much thinner than the absorption length, a maximum or minimum in scattered intensity at the anti-Bragg position is reached for respectively an odd or even number of unit cell layers. Here, just slightly off the anti-Bragg position, small shoulders appear on the oscillations. The simulation does not include a gradual roughening of the surface, which would damp the oscillations like indicated by the experimental data of fig 5.7. A doubling of the intensity oscillation period can therefore be the result of a change in the epitaxial relation between film and substrate. Since the latter is a consequence of strain relief, due to the introduction of dislocations, the accompanying thickness is the upper limit of the so-called pseudomorphic phase: the critical thickness. Films thinner than the critical thickness can adept their structure elastically to match the underlying substrate lattice. With the film becoming thicker, more strain energy is stored up to the thickness where it is more favorable to introduce lattice defects.

A critical thickness of around 20 nm at deposition temperature as implied by the present results, is much higher than the 8 to 13 nm reported for room temperature samples [49, 50, 51]. This implies that during cool-down the critical thickness is further reduced, most likely by the incorporation of extra oxygen leading to the tetragonal-to-orthorhombic phase transition.

5.5 Morphology and stability of ultra-thin films

The results that are described in the previous sections, suggest the formation of a phase different from Y123 for the first closed monolayer. Unfortunately, ultra-thin films of YBCO appeared not to be stable over the typical data collection times needed to measure several CTRs. In figure 5.12 the reflectivity ridge scans are shown for two ultra-thin films just after deposition and several hours later. Clearly the diffraction patterns changed drastically, with what appears the formation of a new phase. For the sub-unit cell thin film, two peaks, situated at 13.75(1) degrees and at 27.75(1) degrees, appear after several hours. Assuming that these are the *001* and *002* reflections of a new phase, a lattice parameter is estimated of 3.23(1) Å. Unfortunately, no other peaks of this phase could be identified, leaving the nature of this phase unclear. Also a slightly thicker film showed not to be stable (fig. 5.12). From the fringes a thickness of 17.1(5) Å is determined, which suggests that at least one complete Y123 unit cell is formed. Now approximately 11 hours later, two peaks at 12.67(1) and 13.54(1) appeared, this time suggesting the formation of new phases having lattice parameters of approximately 3.51(2) and 3.29(2) Å respectively. The sharpness of the peaks that appear after several hours is an indication that the morphology has changed into rather high islands. For the sub-unit cell thin film this was confirmed by ex situ AFM measurements. From the measurements shown here however, it can not be concluded whether the change in morphology is accompanied by reaction as well. Or in other words, it is unclear whether there is a chemical reaction responsible for the changes, or that simply the first monolayer piles up to form islands. Supposing that just after depostion a smooth layer, completely covering the substrate is grown, the expected diffraction pattern will not show sharp features other than the substrate peaks. If however in the course of time islands are formed by this layer, the diffraction pattern may well compose of several sharp peaks, the width of which is related to the average island height.

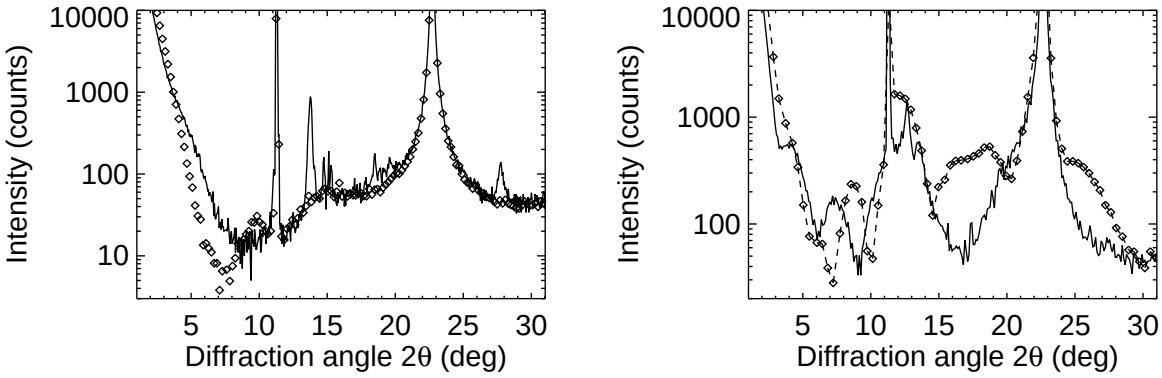

Figure 5.12: Specular reflectivity ridge scans of ultrathin YBCO films at deposition conditions. (left) Measurement just after deposition of approximately half a unit cell layer YBCO (symbols) and 13 hours later (solid line). (right) Measurement just after deposition of approximately one and a half unit cell layer YBCO (symbols and dashed line) and 11 hours later (solid line).

The in-plane order and surface morphology can be studied by rocking curves of specially selected parts in reciprocal space. As an example, a reflection having an in-plane component of momentum transfer, is shown in figure 5.13. The peak shape consists of two superimposed contributions: a sharp feature, being the Bragg component, which describes the long range structural order and a broad diffuse feature which is related to the defect structure [52, 53, 54].

5.6 Conclusions

Use of in situ X-ray diffraction during the PLD growth of YBCO films, enabled to determine several aspects of the growth simultaneously. The clear and distinct intensity growth oscillations reveal that growth proceeds in a layer-by-layer fashion, and that interlayer mass transport is substantial. Comparing the number of observed intensity oscillations during growth and the *c*-axis and total film thickness, leads to the conclusion that the very first two smooth layers do not consist of Y123. This is in accordance with earlier results regarding the initial growth of YBCO [29, 55], from which it was concluded that the initial growth proceeds in blocks that are 1/3 the size of Y123. In the present studies, the times needed to complete each of the very first two smooth layesr, indicate that material equivalent to about 2/3 unit cell

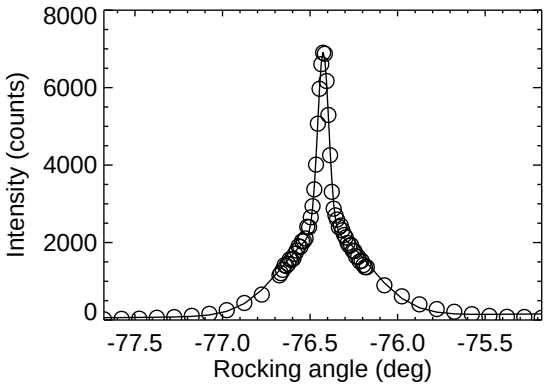

Figure 5.13: The *102* reflection of an approximately 14nm thin YBCO film measured at 780 °C. The solid line is a fit using the superposition of two gaussian profiles, yielding widths of 0.074(1) and 0.566(4) degrees.

layer of Y123 was deposited. Unfortunately, the very first smooth monolayer proved not to be stable during typical data collection times of 12 hours, needed for an extensive data set containing several CTRs. Recent developments using so-called pixel detectors, which are 2-dimensional arrays of pixels, each being a photon counter, have shown to reduce the data collection time by 1 to 2 orders of magnitude [56]. This new generation of X-ray detectors seems therefore to be ideally suited for surface diffraction experiments, where the surfaces under investigation often are stable only for a limited time.

From the angular positions of the diffraction peaks of film and substrate, the epitaxial relationship is determined. Although the accuracy with which the epitaxial relation between film and substrate can be determined is not sufficient to show a change during the growth, it might be related with the intensity oscillation period doubling. Upon a change in epitaxial relationship, the film scattering can no longer be added to the CTR scattering of the substrate because they peak at different positions in reciprocal space and the oscillation period changes from one to two monolayers. The results here indicate that although no significant change of the c-axis of the growing film could be observed, the change in epitaxial relationship between film and substrate can be explained by strain relaxation in the form of the introduction and subsequent alignment of dislocations. The change in intensity oscillation period was not observed in another experiment, although the growth conditions were very similar. Since the scattering is also dependent on the properties of the beam, such as

for instance the divergence, an optimized diffraction set up[6] should allow for a more careful comparison. In such an experiment, one could think of performing several runs thereby changing the miscut angle and direction of the substrate, just as in the ex situ studies [38, 39].

The shape of the out-of-plane Bragg peak of the film after cool down shows that the surface has further roughened and that most likely the crystal quality degraded. Both phenomena are indications that during the conditioning step the strain is further relaxed. This is in agreement with the obtained critical thickness at deposition conditions of 20 nm and reported literature values from ex situ measurements of around 10 nm.

References

[1] J. G. Bednorz, K. A. Müller, Z. Phys. **B64** (1986) 189.

[2] R. J. Cava, J. Am. Ceram. Soc. **83** (2000) 5–28.

[3] M. K. Wu, J. R. Ashburn, C. J. Torng, P. H. Hor, R. L. Meng, L. Gao, Z. J. Huang, C. W. Chu, Phys. Rev. Lett. **58** (1987) 908.

[4] C. P. Poole Jr. (Ed.), *Handbook of Superconductivity*, Academic Press, San Diego, 2000.

[5] K. Yvon, M. François, Z. Phys. B **76** (1989) 413–444.

[6] S. Semenovskaya, A. G. Khachaturyan, Phys. Rev. **B46** (1992) 6511.

[7] W. Schwarz, O. Blaschko, G. Collin, F. Marucco, Phys. Rev. **B48** (1993) 6513.

[8] P. Schleger, H. Casalta, R. Hadfield, H. F. Poulsen, M. von Zimmermann, N. H. Andersen, J. R. Schneider, R. Liang, P. Dosanjh, W. N. Hardy, Physica C **241** (1995) 103.

[9] T. Zeiske, R. Sonntag, D. Hohlwein, N. H. Andersen, T. Wolf, Nature **353** (1991) 542.

[6] The diffractometer at BM26 used for these experiments is also a limiting factor for very accurate peak position measurements, which is seen in the badly resolved substrate peaks shown in figure 5.2.

[10] N. H. Andersen, M. von Zimmermann, T. Frello, M. Käll, D. Mønster, P.-A. Lindgård, J. Madsen, T. Niemøller, H. F. Poulsen, O. Schmidt, J. Schneider, T. Wolf, P. Dosanjh, R. Liang, W. N. Hardy, Physica C **317-318** (1999) 259–269.

[11] R. J. Cava, B. Battlog, C. H. Chen, E. A. Rietman, S. M. Zahurak, D. Werder, Phys. Rev. **B36** (1987) 5719.

[12] H. F. Poulsen, N. H. Andersen, J. V. Andersen, H. Bohr, O. G. Mouritsen, Nature **349** (1991) 321.

[13] J. García López, D. H. A. Blank, H. Rogalla, Appl. Surf. Sci. **127-129** (1998) 1011–1016.

[14] S. W. Tozer, A. W. Kleinasser, T. Penney, D. Kaiser, F. Holtzberg, Phys. Rev. Lett. **59** (1987) 1768.

[15] M. Tinkham, *Introduction to Superconductivity*, McGraw-Hill, New York, 1996.

[16] C. C. Tsuei, J. R. Kirtley, Rev. Mod. Phys. **72** (2000) 969.

[17] H.-J. Smilde, *Josephson contacts between high-T_c and low-T_c superconductors*, Ph.D. thesis, University of Twente, The Netherlands (2001).

[18] D. H. A. Blank, *High-T_c thin films prepared by laser ablation*, Ph.D. thesis, University of Twente, The Netherlands (1991).

[19] Venkatesan et al., Appl. Phys. Lett. **53** (1988) 1431.

[20] R. H. Hammond, V. Matijasevic, R. Bormann, in: R. McDonald, R. Noufi (Eds.), *Science and Technology of thin film superconductors*, Vol. **2**, Plenum Press, New York, 1990, p. 395.

[21] S. K. Singh, J. Narayan, J. Appl. Phys. **67** (1990) 3785.

[22] V. Vonk, S. Konings, L. Barthe, B. Gorges, H. Graafsma, J. Synchr. Rad. **12** (2005) 833.

[23] M. Borsboom, W. Bras, I. Cerjak, D. Detollenaere, D. G. van Loon, P. Goedtkindt, M. Konijnenberg, P. Lassing, Y. K. Levine, B. Munneke, M. Oversluizen, R. van Tol, E. Vlieg, J. Synchr. Rad. **5** (1998) 518.

[24] Y. A. Abramov, V. G. Tsirelson, V. E. Zavodnik, S. A. Ivanov, I. D. Brown, Acta Cryst. **B51** (1995) 942.

[25] G. Koster, B. L. Kropman, G. Rijnders, D. H. A. Blank, H. Rogalla, Mater. Sci. Eng. **B56** (1998) 209.

[26] T. Lippmann, P. Blaha, N. H. Andersen, H. F. Poulsen, T. Wolf, J. R. Schneider, K.-H. Schwarz, Acta Cryst. **A59** (2003) 437–451.

[27] H. Kiessig, Ann. Phys. **10** (1931) 769–788.

[28] E. E. Fullerton, I. K. Schuller, H. Vanderstraeten, Y. Bruynserade, Phys. Rev. **B45** (1992) 9292.

[29] T. Haage, J. Zegenhagen, H.-U. Habermaier, M. Cardona, Phys. Rev. Lett. **80** (1998) 4225.

[30] P. I. Cohen, G. S. Petrich, P. R. Pukite, G. J. Whaley, A. S. Arrott, Surf. Sci. **216** (1989) 222–248.

[31] H. A. van der Vegt, H. M. van Pinxteren, M. Lohmeier, E. Vlieg, J. Thornton, Phys. Rev. Lett. **68** (1992) 3335.

[32] H. Nagai, J. Appl. Phys **45** (1974) 3789.

[33] G. H. Olsen, R. T. Smith, Phys. Stat. Sol. (a) **31** (1975) 739.

[34] B. W. Dodson, D. R. Myers, A. K. Datye, V. S. Kaushik, D. L. Kendall, B. Martinez-Tovar, Phys. Rev. Lett. **61** (1988) 2681.

[35] L. J. Schowalter, E. L. Hall, N. Lewis, S. Hashimoto, Thin Solid Films **184** (1990) 437.

[36] F. Riesz, J. Vac. Sci. Technol. A **14** (1995) 425.

[37] J.-L. Maurice, J. Briático, D.-G. Crété, J.-P. Contour, Phys. Rev. **B68** (2003) 115429.

[38] J. M. Dekkers, G. Rijnders, S. Harkema, H. Smilde, H. Hilgenkamp, H. Rogalla, D. H. A. Blank, Appl. Phys. Lett. **83** (2003) 5199.

[39] J. M. Dekkers, *Twin Behaviour of $YBa_2Cu_3O_{7-x}$ Thin Films on Vicinal $SrTiO_3$ Substrates*, Master's thesis, University of Twente, The Netherlands (2002).

[40] F. Riesz, Vacuum **46** (1995) 1021.

[41] D. Hull, Introduction to Dislocations, Pergamon Press, Oxford, 1975.

[42] A. DelVecchio, L. Mirenghi, L. D. Caro, L. Tapfer, C. Aruta, G. Petrocelli, G. Balestrino, J. Appl. Phys. **82** (1997) 5465.

[43] G. Koster, K. Verbist, G. Rijnders, H. Rogalla, G. van Tendeloo, D. H. A. Blank, Physica **C353** (2001) 167.

[44] J. M. V. Hove, , P. R. Pukite, P. I. Cohen, J. Vac. Sci. Technol. B **3** (1984) 563.

[45] J. P. A. van der Wagt, K. L. Bacher, G. S. Solomon, J. S. Harris Jr, J. Vac. Sci. Technol. B **10** (1991) 825.

[46] H. A. van der Vegt, W. J. Huisman, P. B. Howes, E. Vlieg, Surface Sci. **330**, (1995) 101–112.

[47] I. K. Robinson, Handbook on Synchrotron Radiation, Vol. **3**, North-Holland, Amsterdam, 1991, Ch. 7, pp. 221–266.

[48] W. Braun, B. Jenichen, V. Kaganer, A. Shtukenberg, L. Däweritz, K. Ploog, Surf. Sci. **525** (2003) 126.

[49] K. Kamigaki, H. Terauchi, T. Terashima, K. Yamamoto, K. Hirata, K. Hayashi, I. Nakagawa, Y. Tomii, J. Appl. Phys. **69** (1991) 3653.

[50] J. Zegenhagen, T. Siegrist, E. Fontes, L. E. Berman, J. R. Patel, Sol. State Comm. **98** (2004) 763.

[51] V. Vonk, S. J. van Reeuwijk, J. M. Dekkers, S. Harkema, A. Rijnders, H. Graafsma, Thin Solid Films **449** (2004) 133.

[52] M. Krivoglaz, *X-ray and neutron diffraction in non-ideal crystals*, Springer Verlag, Berlin-Heidelberg, 1996.

[53] V. M. Kaganer, R. Köhler, M. Schmidtbauer, R. Opitz, Phys. Rev. **B55** (1997) 1793–1810.

[54] E. Vlieg, J. F. van der Veen, S. J. Gurman, C. Norris, J. E. MacDonald, Surf. Sci. **210** (1989) 301–321.

[55] G. Rijnders, *The initial growth of complex oxides: study and manipulation*, Ph.D. thesis, University of Twente, The Netherlands (2001).

[56] C. M. Schlepütz, R. Herger, P. R. Willmott, B. D. Patterson, O. Bunk, C. Brönnimann, B. Henrich, G. Hülsen, E. F. Eikenberry, Acta. Cryst. **A61** (2005) 418.

Chapter 6

Thermal Cycling of $YBa_2Cu_3O_{7-x}$ Thin Films Studied in situ by Synchrotron X-ray Diffraction

6.1 Introduction

Thin films of $YBa_2Cu_3O_{7-x}$ (YBCO) are widely used in various High-T_c superconducting applications involving magnetism and electronics. Usually, thin YBCO films of several tens of nanometers are fabricated either by sputtering or laser ablation. Since the deposition process can be controlled very accurately, it is possible to engineer structures, down to the nanometer level. Examples are ramp-type Josephson junctions [1], Superconducting Quantum Interference Devices (SQUIDs) [2] or fabrication of well-defined in-plane grain boundaries [3]. Especially Josephson juntions of High-T_c and Low-T_c superconducting materials show behaviour, that allows to study the fundamentals of superconductivity [4, 5]. In order to fabricate these structures, a thin film has to be processed in several steps consisting of lithography and deposition. It is well-known that the superconducting properties of YBCO depend strongly on the crystal structure, the oxygen deficiency and subsequent ordering [6]. Since the latter is closely related to strain and microstructure, it is interesting from a fundamental point of view to study the oxygen ordering in thin films, because it is closely related to the superconductivity. The high temperature structure of YBCO, with 6 oxygen atoms in the unit cell, is not superconducting. In order to obtain the appropriate phase, it has been shown that annealing in a well defined oxygen atmosphere is necessary. Many experiments over the past years have been devoted to the study of oxygen dynamics in YBCO as a function of temperature, and it is

generally accepted that anisotropic oxygen diffusion takes place. The oxygen diffusion constants $D_{a,b}$ and D_c differ by a factor of 10^3, D_c being the smallest. Aarnink *et al.* [7] showed by an in situ ellipsometric study that indeed oxygen diffusion in c-axis oriented YBCO films on $SrTiO_3$ is essentially a 2D process in the ab-plane. Defects, like grain boundaries, act as shortcuts for oxygen diffusion in the c-direction. This implies that the micro structure of the film is very important for the diffusion process. By interface engineering, the defect density can be reduced, resulting in much longer annealing times in oxygen in order to obtain superconducting films, because of the enlarged in-plane diffusion path [8].

Here, in situ X-ray diffraction studies employing synchrotron radiation of thermal cycling of thin YBCO films are presented. From the postions of the Bragg peaks and their widths it was possible to follow uniform and non-uniform strain in different crystallographic directions as a function of temperature. At moderate temperatures, in the range 250-350 °C, drastic changes in the microstructure occur. When cooling down from this temperature range, the changes appear irreversible. However, when reverting to deposition conditions, T=780 °C, and following a commonly used anneal procedure [9] it was possible to obtain the initial structure again. This method might be of interest to improve the quality of structures that are thermally cycled several times during fabrication. In the following paragraphs first the twinning mechanism and then the phase diagram of YBCO will be described. Next the results of peak-shape analysis of *00l* reflections of two YBCO thin films are presented. Then, the results of experiments in which thin YBCO films were thermally cycled are discussed. Finally the results of following the temporal evolution of the positions and widths of diffraction peaks of YBCO films at elevated temperatures are presented. In the final section the different results are discussed in view of earlier results obtained from similar experiments performed mosltly on YBCO powder samples.

6.2 Twinning in $YBa_2Cu_3O_{7-x}$

In section 5.2.1 the crystal struture of bulk YBCO was already discussed. Here a description of the microsctructure is given, foussing on the twinning mechanism. As a function of the oxygen content, YBCO has a tetragonal or orthorhombic crystal structure and the transition between the two structures is of the so-called ferro-elastic kind, because spontaneous strain is the driving force [10]. A consequence of this ferro-

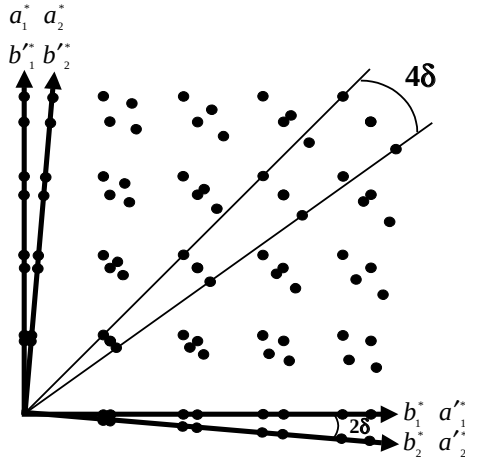

Figure 6.1: Schematic overview of reciprocal space of YBCO in the l=0 plane. Each of the domains has corresponding axes a_i^* and b_i^* with i=1-2. The twinning is described by a 2δ rotation around the c^*-axis and inversion of a and b axis (see text). The two outer peaks of the *hh0* reflections are separated by an angle 4δ.

elastic strain is that orthorhombic YBCO is twinned with twin walls parallel to the mutually perpendicular *hh0* and $h\bar{h}0$ mirror planes of the tetragonal lattice [11]. This mechanism leads to four different co-existing twin-domain orientations [12] and is schematically shown in figure 6.1. Twinning in YBCO appears in the *hk*-plane and is visualized as four different sets of axes (a_i^*, b_i^*). The set (a_1^*, b_1^*) is rotated over an angle 2δ with respect to the set (a_2^*, b_2^*). The other two sets are obtained by inverting the a and b axes, indicated by $(b\prime_1^*, a\prime_1^*)$ and $(b\prime_2^*, a\prime_2^*)$ in figure 6.1. The rotation angle 2δ is directly related to the in-plane direct lattice parameters by:

$$\tan\delta = \frac{b-a}{b+a} \equiv \eta \tag{6.1}$$

The parameter η is the so-called orthorhombicity, which in case of a tetragonal structure is zero and in case of an orthrorhombic structure is non-zero. Clearly, twinning appears only when the a and b axes are not identical and the larger the difference the larger the splitting indicated by the angle 2δ. The two outermost peaks of an *hh*0 reflection are separated by an angle 4δ, as can be seen in figure 6.1. This separation can be measured by a simple ω-scan[1]. In the experiments described in this chapter,

[1]More details about the twinning and resulting difraction pattern can be found in chapter 7.

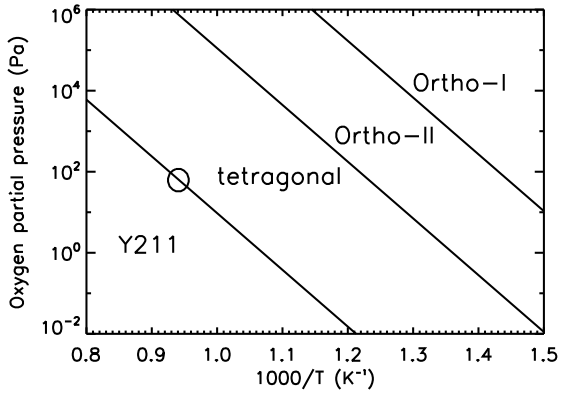

Figure 6.2: Phase diagram (P_{O_2}, T) of YBCO [13]. The circle indicates the area where usually the pulsed laser deposition parameters are chosen for optimal YBCO growth. The lines separating the different phases should not be taken as sharp as indicated here, which is also implied by the optimal PLD parameter area being on both sides of the Y211/Y123 decomposition line (see also section 5.2.2).

the splitting of *hhl*-type reflections will be used as an indication of changes in the in-plane lattice parameters, which is related to strain and to the oxygen content in the thin YBCO films.

6.3 Phase diagram of $YBa_2Cu_3O_{7-x}$

The phase diagram given by Hammond *et al.* [13] and shown in figure 6.2 is often used to illustrate the structure of YBCO as a function of temperature and partial oxygen pressure. The PLD process takes place at 780 °C ($= \frac{1000}{1053} = 0.95\mathrm{K}^{-1}$) and around an oxygen partial pressure of 1 mbar (=100 Pa), close to the Y211/Y123 decomposition line. In order to obtain the desired Ortho-I phase, the oxygen pressure is increased once the film is grown, after which the sample is cooled down to room temperature.

6.4 Experimental

Thin YBCO films were grown by Pulsed Laser Deposition (PLD) on STO(001) in a standard way [14]. The substrates were chemically treated prior to deposition in order to obtain single TiO_2 termination [15]. X-ray diffraction measurements were

carried out at end-station ID15C [16] of the European Synchrotron Radiation Facility, Grenoble, France. The samples were mounted in a furnace, consisting of a resistor wire embedded in a nickel heater block, surrounded by an aluminium wall, which was partially thinned to 0.5 mm, in order to minimize absorption of the X-ray beam. The watercooled base-plate was mounted on a translation stage and the whole furnace was put on a Huber 511.1 diffractometer. A single bounce Si(111) monochromator provided the 38 keV X-ray beam and by using a WB_4 multilayer, higher harmonics in the incident beam were reduced by at least three orders of magnitude. Two pairs of slits were placed before the detector, thereby reducing the background and allowing a high angular resolution. The instrument resolution could be improved further by changing the horizontal aperture of a slit in front of the diffractometer, thereby reducing the divergence of the incoming X-ray beam. The instrument resolution function was characterized, using a Si single crystal as analyzer. In the range $0 < \sin(\theta)/\lambda < 0.3$, the widths of the Si peaks were at least a factor of 10 smaller than diffraction peaks of the thin film samples discussed here. These very narrow Si peaks indicate that the instrument resolution function does not contributes significantly to the width of the thin film diffraction peaks. Therefore, to a good approximation, it was not necessary to deconvolve the instrument resolution function from the measured thin film diffraction profiles.

6.5 Results

The set-up, described in the previous section, allowed to determine the peak positions and widths with high accuracy. In the next two sections, the results of peak-shape analysis of Bragg reflection measurements and the measurements as function of temperature will be shown.

6.5.1 Particle size and strain

By differentation of Bragg's law, diffraction peak broadening, β, due to the crystallite size-effect and the non-uniform strain results in:

$$\beta_{size} = \frac{1}{2L} \tag{6.2}$$

and

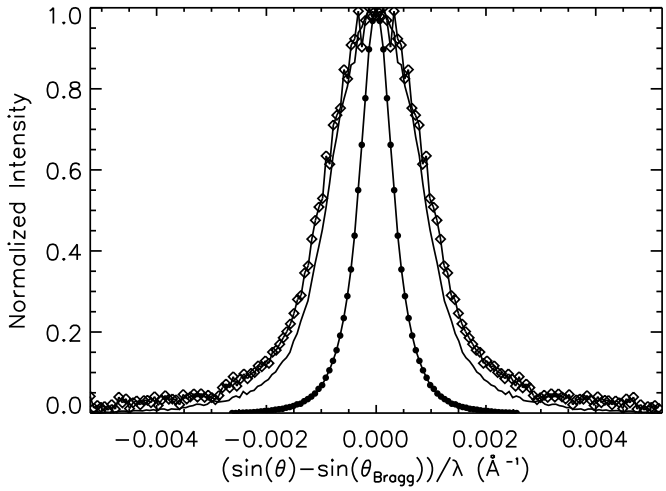

Figure 6.3: Several orders of the *00l* reflections as a function of $\sin(\theta)\lambda$ of a 400 nm YBCO film. Shown are the *005* (circles), *007* (solid line) and *0010* (squares), that were made symmetric as described in the text. In order to centre the reflections at zero, each peak is displaced by $\sin(\theta_{Bragg})/\lambda$ which is the position of the particular Bragg reflection. The intensities are all normalized to one.

$$\beta_{strain} = \frac{\sin(\theta)}{\lambda}\frac{\Delta d}{d} \tag{6.3}$$

where both widths are given in units of $\sin(\theta)/\lambda$ ($=\text{Å}^{-1}$), L is the crystallite size and $\frac{\Delta d}{d}$ the strain[2]. The crystallite-size effect is constant as a function of $\sin(\theta)/\lambda$, unlike the strain effect. In figure 6.3 several orders of the *00l* reflections of a 400 nm YBCO film are shown. Clearly, in figure 6.3 the diffraction peaks become wider for higher order reflections, which is an indication of non-uniform strain. Assuming a delta-shaped instrument resolution function as described in section 6.4, the shapes of the resulting diffraction peaks are a convolution of the size and strain effects and by use of the Warren-Averbach method, the two contributions may be separated [17]. This method consists of Fourier analysis of the diffraction profiles, which in general results in complex functions. In the analysis real functions need to be used[18]. For

[2]Here is meant that not the average d changes, but that there is a spread in d spacings given by Δd. A change Δd, which shifts the average d-spacings, would give rise to a shift in the *position* of the diffraction peak. This also would require a minus sign in the right hand side of equation 6.3.

this purpose, only the real, symmetric, part of the Fourier transform of the peaks was used, which resulted in peak shapes that deviated an average of three times the statistical uncertainty per point from the raw data ($\chi^2 < 3$ by use of counting statistics). The Fourier components can be assumed to depend linearly as function of l^2, given by [19, 20][3]:

$$A(n,l) = A_s(n)\left(1 - 2\pi^2 n^2 l^2 < \epsilon^2(n) >\right) \tag{6.4}$$

with A_s the Fourier components of the particle size part, n the harmonic number in the Fourier series, l the diffraction index and ϵ the strain contribution. Extrapolation of the Fourier components to $l = 0$ resulted in a crystallite size $L_z = 69 \pm 7$ nm for the nominally 400nm thick film. Similar measurements on another, nominally 100 nm thick film, resulted in $L_z = 83 \pm 5$ nm. In addition, due to the appearence of Kiessig fringes on the low and high angle side of the *001* reflection, a film thickness $t = 100 \pm 2$ nm could be determined as well for this sample. These results will be discussed in more detail in section 6.6.1.

6.5.2 Temperature cycling

In the next paragraphs the results of thermal cycling of several thin YBCO films are presented. First three different samples are described which were heated in 1 bar of oxygen. Next briefly the results of several films that were heated in vacuum will be given.

6.5.2.1 First sample

This sample, having a nominal thickness of 400nm, was subjected to a heat treatment ranging from room temperature up to 450 °C under 1 bar of flowing oxygen. The evolution of the *007* and *115* reflections is shown in figure 6.4. The widths, β, are obtained from a 2θ-scan. From the *007* reflection the film c-axis is deduced, which is subsequently used to determine the average in-plane lattice parameter $\bar{a} = (a + b)/2$ from the *115* reflection.

The lattice parameters expand linearly as a function of temperature. Since with increasing temperature the sample position changes with respect to the X-ray beam

[3]Originally values of $\ln A$ were evaluated as function of l^2. In practise this gives only good results for pure Gaussian profiles.

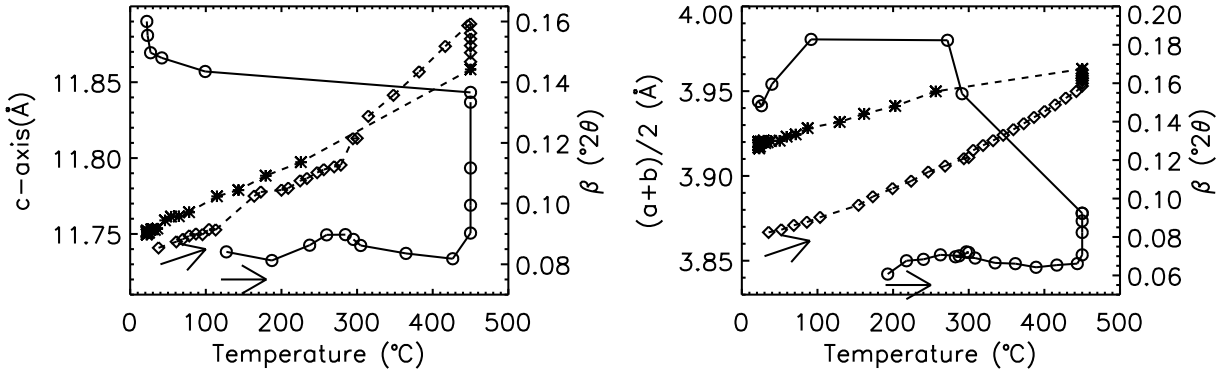

Figure 6.4: (left) Lattice constant c during heating (squares) and subsequent cooling (asterisks) of the *007* reflection of a nominally 400 nm thick film as function of temperature. Shown in the same plot is also the width β (circles) of the 2θ-scan.
(right) Average in-plane lattice constant $\bar{a} = (a + b)/2$ during heating (squares) and subsequent cooling (asterisks) as function of temperature and the corresponding width β (circles) obtained from the 2θ-scan of the *115* reflection.

due to thermal expansion of the whole furnace, the height of the sample was re-addjusted several times. The positions of the reflections will change as a result of such a re-alignment procedure and appear as small jumps in figure 6.4, nevertheless the c-axis parameter clearly shows linear trends as a function of temperature. Around 300 °C however, there appears a kink in the temperature dependence of the c-axis, which is evident from a sudden change in the slope. Then at the temperature plateau at 450 °C, the c-axis decreases slowly, and upon cooling contracts again. After reaching room temperature again, it is obvious that there is an increase in c-axis of 0.1-0.2 Å (1-2 %) with respect to the start of the heat treatment. From the width of the 2θ-scan of the measured reflection, it is clear that all the way up to 450 °C there is hardly any change, whereas on the plateau the width increases considerably, and also irreversibly. After reaching room temperature again, the width of the reflection has increased by about 0.06 $^o2\theta$ (75%), meaning that it has almost doubled. Similar behaviour is seen for the average in-plane lattice parameter as function of temperature in figure 6.4.

6.5.2.2 Second sample

The results of following an *hhl*-type reflection of another nominally 400 nm thick YBCO film are shown in figure 6.5. The d-spacing of the *115* shows behaviour similar to the reflections as described for the first sample in the previous section. The ω-

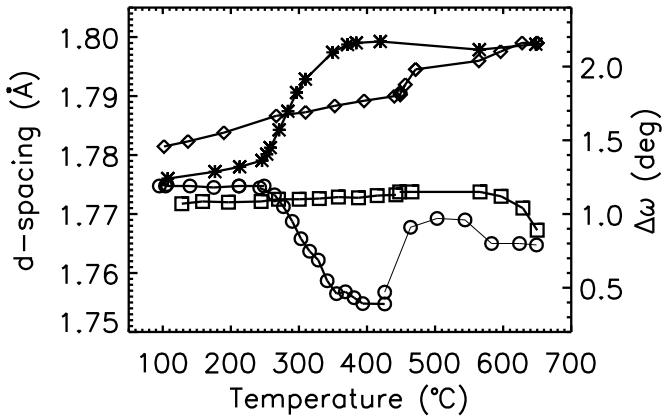

Figure 6.5: Splitting of the *115* reflection $\Delta\omega$ as a function of temperature during heating ($\circ$) and cooling ($\square$). The d-spacing of the *115* reflection is shown as well during heating ($*$) and cooling ($\diamond$). The smaller the angle $\Delta\omega$, the less the twin structure is developed. Clearly at 250 and 450°C drastic changes occur.

scan of this type of reflection, shows three superimposed peaks, due to the twinning mechanism as described in section 6.2. All three peaks emerge from lattice planes with an equal spacing, therefore having equal Bragg angles, only their positions in ω are different because they belong to different twin domains. Again due to thermal expansion of the crystal lattice, the d-spacing of the reflection increases linearly with temperature. At 250 °C, the lattice spacing changes drastically to become more or less constant at 350 °C. At the same time, the angle between the outermost peaks in the ω-scan, $\Delta\omega$, becomes much smaller. This means that the three peaks come closer to the middle one, which indicates that the angle between the different twin domains is becoming smaller. By increasing the temperature to 650 °C, the peaks separate again, but not to the initial value. An irreversible change occurs for the d-spacing as well.

In a second experiment, the same 400 nm thick YBCO film was subjected to heat treatments in 1 bar of flowing oxygen. Here, at 750 ^{o}C the shape of the ω-scan of an *hhl*-type reflection changes to a single peak, that is $\Delta\omega = 0$, which is shown in figure 6.6. Clearly, the shoulders on the main peak disappear, and a single peak is formed. If merely the twin structure would disappear, the integrated intensity should stay the same, and the intensity that disappears from the shoulders, should appear

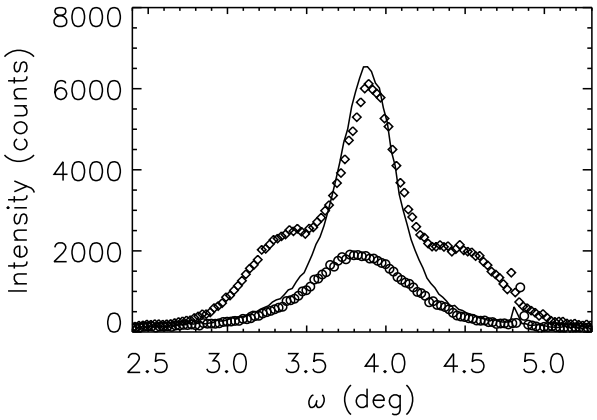

Figure 6.6: The orthorhombic-to-tetragonal phase transition and subsequent loss of the 123-phase of a 400 nm film. Shown are three ω-scans of the *115* reflection measured at 750 °C in 1 bar of flowing oxygen, with a two minutes time interval. The change from a fully developed twin structure, with a split peak (squares), to an untwinned structure (solid line), and subsequent diminishing intensity (circles), is evident. Two minutes later the *115* completely disappeared, which indicates that the Y123 phase decomposed.

in the main peak. The fact that the integrated intensity is reduced by 30% from the three-peak shape to the single peak, is an indication that the crystal structure is decomposing. Unlike in the previously described experiment (fig. 6.7), where the reflection maintained its characteristic shape, here the thin film is decomposing which is further evidenced by the reflection finally disappearing.

6.5.2.3 Third sample

Figure 6.7 shows ω-scans of the *225* reflection of an 80nm thick YBCO film during heating. The peak positions, shown in the inset of figure 6.7, are obtained by fitting the superposition of three Lorentzians to the peak profiles. Clearly, above approximately 230 °C, the two outermost peaks get significantly closer to the middle peak, that stays constant. However, the characteristic peak shape maintains, which indicates that the twin structure has not vanished completely. The decreasing intensity of the *225* is caused mainly by a too small detector acceptance angle for the reflection of the thin film whose crystal quality is degrading at higher temperatures. This is

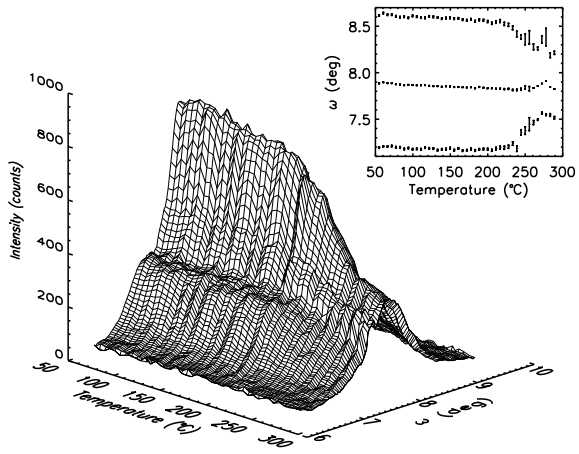

Figure 6.7: The *225* reflection of a 80 nm thin YBCO film as a function of temperature and rocking angle ω. The inset shows the positions obtained from fitting the superposition of three Lorentzians to the rocking scans at each temperature. Clearly around 230 °C the two outer peaks move toward the central one. Although it seems as if there is a small peak of possibly a new phase appearing in the diffraction pattern, this was found to be an artefact.

concluded from the shapes of the 2θ-scans, which at higher temperatures do not show a flat plateau anymore.

6.5.2.4 Summary of thermal cycling results in oxygen

In Table 6.1 the results of four different experiments, conducted on the three previously described thin films in an oxygen environment are given. The transition temperature, T_t, is defined as the point where the two outermost peaks of the *hhl* start to move towards the central peak, as described previously. Furthermore, the linear expansion coefficients of the d-spacings, α_{hkl}, corresponding to the measured reflections are listed. In the present case these follow from:

$$\frac{1}{d_{hkl}}\frac{d(d_{hkl})}{dT} = \alpha_{hkl} \tag{6.5}$$

with d_{hkl} the spacing of the hkl planes as function of temperature T. As a comparison, the values of the linear expansion coefficients for several d-spacings obtained from powder diffraction data [21], are listed in Table 6.2.

		$T < T_t$		$T > T_t$		T_{cool}	
t (nm)	T_t (°C)	$\alpha_{hhl}(K^{-1})$	$\alpha_{00l}(K^{-1})$	$\alpha_{hhl}(K^{-1})$	$\alpha_{00l}(K^{-1})$	$\alpha_{hhl}(K^{-1})$	$\alpha_{00l}(K^{-1})$
400^{I}	250(20)	1.59(7)	-	14.1(4)	–	1.18(7)	–
400^{II}	250(20)	1.11(2)	1.63(3)	8.4(5)	14(1)	1.1(2)	1.9(1)
400	280(20)	1.88(4)	2.10(7)	2.69(2)	3.86(2)	1.39(4)	2.14(2)
80	230(20)	1.09(7)	1.35(7)	0.7(3)	28.4(6)	0.5(2)	0.5(1)

Table 6.1: Overview of characteristics of different YBCO films, which were subjected to heat treatments in 1 bar O_2. The linear expansion coefficients α_i are given in $10^{-5}K^{-1}$. For the 400nm films the *115* was followed, for the 80nm film the *225* reflection. The superscripts I and II denote the second sample from section 6.5.2.2 before and after the standard anneal treatment as described in section 6.5.3.

hkl	α_{hkl} (K^{-1})
100	1.0
010	1.2
001	1.9
115	1.6
225	1.3

Table 6.2: Thermal expansion coefficients for different lattice planes of YBCO. The values for α_i, all given in $10^{-5}K^{-1}$, are estimated from the low temperature part (T<450°C) of the powder diffraction data on orthorhombic YBCO by Jorgensen *et al.* [21].

6.5.2.5 Thermal cycling in vacuum

In order to investigate the influence of the oxygen background pressure on the crystal structure of YBCO films at elevated temperatures, experiments similar to those described in the previous sections were carried out in vacuum. The results of the tranistion temperature where the ω-scan starts to change its shape are shown in Table 6.3.

Again here the structural changes proved irreversible upon cooling down to room temperature.

t(nm)	T_t (°C)
60	250(20)
80	300(20)
100	280(20)
400	300(20)

Table 6.3: Overview of transition temperatures (T_t) of different thin YBCO films, subjected to a heat treatment in vacuum ($P < 10^{-3}$ mbar).

6.5.3 Recovery

The results of thermal cycling, summarized in Table 6.1, indicate that irreversible structural changes occur. In order to investigate the effect of reverting to deposition conditions, and using a commonly used annealing procedure, two different films were used, a 400nm and a 40nm. Both films had been subjected to heat treatments similar to the ones described so far. Subsequently, the films were heated to 780 °C in 0.5 mbar oxygen and kept at these conditions for 30 minutes, after which the oxygen pressure was increased to 1 bar and the films were cooled to room temperature in two steps, stopping at 600 °C and 450 °C, 20 minutes each time. For the 400nm film, this treatment resulted in the splitting of the peaks in the *115* increasing from $\Delta\omega = 1.12$ to 1.19 degrees and the FWHM of the same reflection decreasing from 0.46 to 0.34 degrees. The *00l* reflections of the 40nm film had completely disappeared after a heat treatment to 450 °C, which indicates that the crystal quality degraded severely or that the Y123 phase decomposed. After reverting to deposition conditions and following the anneal procedure as described above, the *00l* reflections appeared again, which is shown in figure 6.8.

6.5.4 Temporal evolution

In order to investigate the structural evolution as function of time, experiments were carried out at a fixed temperature of 450°C. The results of following two types of reflection for a 400 nm thick YBCO film are shown in figure 6.9.

Diffusion controlled processes, often behave according to the theorem described by Avrami [22], which results in exponential-like behaviour. Here a slightly different form is used, because the measurements were stopped before a new equilibrium was

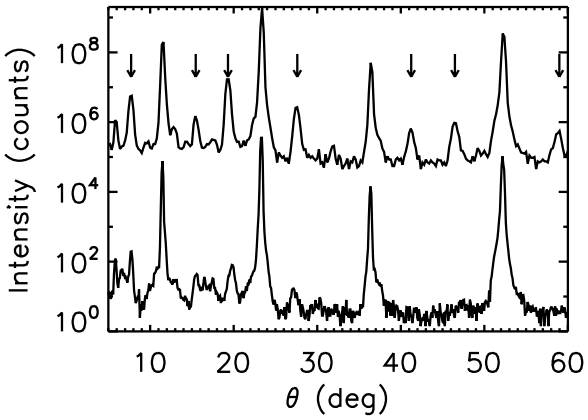

Figure 6.8: Effect of different annealing procedures on the structure of a 40nm YBCO film. Shown are the scans, using Cu K_α radiation, along the *00l* direction after a heat treatment at 450 °C in flowing oxygen (150 l/hour) for 1 hour (bottom) and after an anneal procedure from 780 °C (top) as described in the text. The four strongest reflections originatie from the STO substrate, the arrows indicate YBCO film reflections. Clearly the film *0010*, *0011* and *0013* reflections, around 42, 47 and 59 degrees respectively, appear after the anneal at 780 °C.

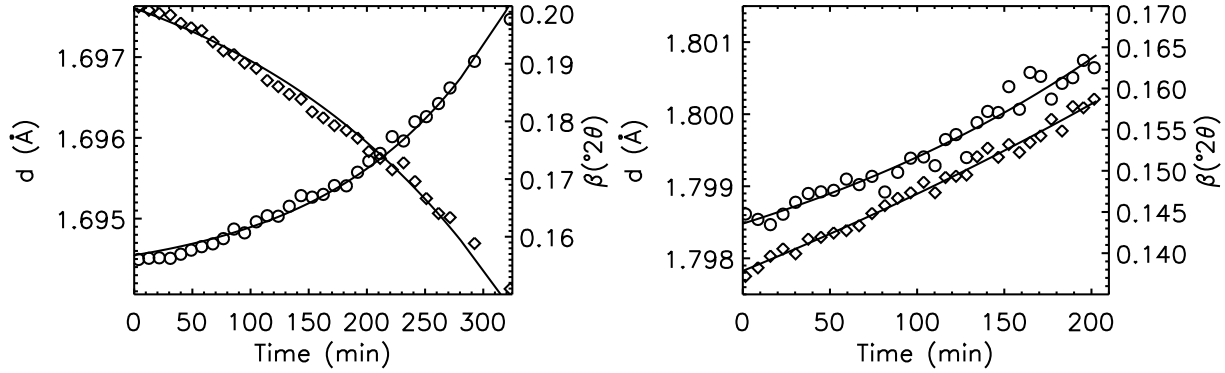

Figure 6.9: Temporal evolution of d-spacings (squares) and widths β (circles) of the *007* (left) and *115* (right) reflection. The solid lines are fits to an exponential-like as describe by equation 6.6.

hkl	τ_d (min)	τ_β (min)	τ_d/τ_β (-)
007	$2.3(2)\times10^2$	$1.4(1)\times10^2$	1.6(2)
115	$6(3)\times10^2$	$3(1)\times10^2$	2(1)

Table 6.4: Characteristic times of the lattice spacings (τ_d) and widths (τ_β) of two different reflections from a 400 nm thick YBCO film at 450°C in a flowing oxygen environment. The values listed here are obtained from fitting a functional form like equation 6.6 to the data shown in figure 6.9.

reached. If it is assumed that the functional form of the evolving lattice spacings and widths resembles an exponential like:

$$y(t) = y_\infty + y_0 e^{-t^n/\tau} \tag{6.6}$$

where the physical quantity of interest, y, changes exponentially with time from an initial value $y_\infty + y_0$ to a final value y_∞ with a characteristic time constant τ. In all cases, the best fit was obtained with n very close to 1. Therefore in the final fits, of which the results are shown in table 6.4, n was fixed to 1 in order to reduce the number of parameters. For other samples, of which the results are not shown here, the characteristic time scales at which the peak shapes and/or positions change around T_t (250-300 °C) are in the range 20-200 minutes.

The widths of the *007* reflection evolve significantly faster than the lattice parameter as function of time. For the *115* reflection the same seems to hold, though the error bar is too large to be conclusive.

6.6 Discussion and conclusions

6.6.1 Particle size and strain

The crystallite size L_z obtained via the Warren-Averbach method from the high resolution diffraction profiles shown in section 6.5.1, is clearly not the thickness of the sample. This might be an indication of defects in the z-direction, which means that the total film thickness composes of several domains. Unfortunately, the method used here does not allow to determine the kind of defect, which may be grains, dislocations or stacking faults. Nevertheless, trends as function of temperature in the widths of

the reflections can be followed, and if assuming that the grain size does not change at moderate temperatures, the broadening is a consequence of increasing non-uniform strain.

6.6.2 Thermal treatment

Between 250 °C and 350 °C the crystal structure of all the studied films changes. This is seen in the sudden changes in the trends of positions and shapes of the reflections of the YBCO thin films as a function of temperature. After completion of a whole temperature cycle, up to temperatures as high as 650 °C, all samples show to have gone through an irreversible structural change. Similar results are obtained by Stenger *et al.* [23], who showed that the c-axis of sputtered YBCO thin films changes irreversibly when being heated above 200 °C in a 10 mbar oxygen environment. They conclude from the well-established relation between c-axis and oxygen content for bulk YBCO [24], that the irreversible change is due to oxygen out-diffusion. The oxygen content compares very well with values obtained for the superconducting transition temperature, determined for their samples after heat treatment. Platzer *et al.* [25, 26] find that oxygen deficient (x=0.75), tetragonal YBCO films change during heating in flowing oxygen to the orthorhombic structure between 200 and 400 °C.

By use of the standard anneal procedure, described in section 6.5.3, the crystal structure can be restored as indicated by the reappearence of the Bragg peaks in figure 6.8. In this procedure, the thin film samples were heated to 780 °C in 0.5 mbar oxygen, which is very close to the point of decomposition of the Y123 phase as shown in the phase diagram of figure 6.2. The successful restoration of the crystal structure at this high temperature seems to indicate that the thermodynamic conditions are optimal for the formation of the Y123 phase and for obtaining a good crystal quality. The latter can be explained by enhanced kinetics, which promote grain growth. This seems to be in agreement with earlier studies showing enhanced structural disorder in thin YBCO films heated to temperatures above 850 °C [27]. At lower temperatures in the studies presented here, the crystal quality of the thin films mainly seems to degrade.

6.6.2.1 Comparison with bulk YBCO powder

Thermogravimetric measurements [28] on fully oxygenated ($x = 0.02$) YBCO powders show that, within the accuracy of the experiment, the onset temperature for

	P_{O_2} (Pa)	T_{onset} (°C)	T_{OT} (°C)	α_c^{max} (K^{-1})
Callagher *et al.* [29]	0.2 (air)	500	620	4.5
Jorgensen *et al.* [21]	1.0	500	700	4.6
	0.2	500	670	-
	0.02	450	640	-
Kogachi *et al.* [30]	1.0	600	705	4.3
	0.25 (air)	525	663	5.6
	0.0 (vacuum)	450	552	6.7
Mizusaki *et al.* [31]	1.0	400	735	3.4
	0.1	350	620	5.2
	0.01	300	560	6.8
	0.001	300	495	6.8
	0.0001	250	435	9.3

Table 6.5: Overview of published results obtained from powder diffraction measurements. Most of the values are estimated graphically from the raw experimental curves shown in the different publications. For different oxygen partial pressures P_{O_2} are shown the temperature T_{onset} where the a and b axes start to deviate from linear behaviour as function of temperature, the temperature T_{OT} where the a and b axes become equal, which indicates the orthorhombic-to-tetragonal phase transition and the maximum thermal expansion coefficient α_c^{max}, given in $10^{-5}K^{-1}$, which is obtained from the maximum slope of the c-axis versus temperature measurements given in the various publications.

oxygen out-diffusion is approximately 400 °C, irrespective of the oxygen partial pressure[4]. In situ X-ray and neutron powder diffraction experiments have been performed extensively to investigate the structure evolution during heat treatments in different oxygen environments. An overview of several literature results for powders is given in table 6.5. A distinction is made between two different temperatures. The first, T_{onset}, is estimated from the various publications as the temperature where the lattice parameters a and b start to deviate from linear behaviour as function of temperature. The second, T_{OT}, is the temperature at which the lattice parameters a and b become equal, and represents the point at which the oxygen becomes diordered as discussed in section 5.2.1. The values listed in table 6.5 are determined graphically

[4]The temperature of 400 °C mentioned here, is the point at which for all the investigated oxygen partial pressures the oxygen content in the YBCO powders has changed by approximately $\Delta x \approx 0.03$, which is about the error given by the authors in reference [28].

from the various publications. This is not be the most accurate way, which might explain that there is scatter in the various values listed in table 6.5. Another explanation for this scatter could be that not only temperature and partial oxygen pressure are of importance, but most likely that not all powders are exactly identical. For instance the grain size, the defect density or the microstrain could be different fro the powders in the various experiments. It is very likely that the same holds in the case of the thin films studied here. Nevertheless, the literature results indicate some generalities which seem to hold in the case of powders and can be compared with the thin film results obtained here. All the values listed are dependent on the oxygen partial pressure. With decreasing oxygen partial pressure, the values for T_{onset} and T_{OT} decrease. This is understood by considering that oxygen out-diffusion is relatively more easy when the difference in oxygen concentration between film and surroundings is larger. Unlike for the powders, the values T_t obtained for the thin films studied here, are, within the scatter of the data, independent of oxygen partial pressure and are lower than the values Tonset obtained for the powders. This suggests that the temperature T_t is not so much related to oxygen out-diffusion, but more to a change in (micro) structure due to another mechanism. One possibility might be that the oxygen is becoming mobile within the crystal lattice, thereby effecting the strain state of the film very much. The onset temperature for the oxygen becoming mobile should not be dependent on the actual micro structure of the thin films, nor on the oxygen partial pressure. Therefore, the same behaviour is expected for YBCO powders. However, the strain-state of a powder is expected to be different from a thin film, mainly due to the film having another defect structure and the influence of the substrate. The oxygen becoming mobile and hopping through the crystal lattice is also a diffusion process. However, the oxygen becoming less ordered and leaving the crystal via out-diffusion have a different effect on the diffraction peaks. The first effect is not expected to change the average lattice parameters, but does have an effect on the twinning mechanism because the strain state is changing. However, in the temperature range studied here, oxygen-out-diffusion is of course non-zero, which means that the two effects always appear simultaneously. At temperatures in the range of 250 °C -350 °C, the effect on the scattering pattern of oxygen out-diffusion is less pronounced compared to the effect of oxygen becoming mobile.

The values for α_c^{max} are systematically larger than the thermal lattice expansion coefficients listed in table 6.2. This is understood from the c-axis becoming larger with decreasing oxygen content due to out-diffusion [32]. Furthermore, α_c^{max} becomes

larger with decreasing oxygen partial pressure, which can be related to an enlarged oxygen out-diffusion. Comparing the powder results for α_c^{max} to the results for α_{00l} obtained for thin films in a 1 bar oxygen environment listed in table 6.1, shows that values for most thin film samples are significantly larger. The measurements on the thin films presented here are most likely not performed on samples that were in equilibrium, unlike in the case of the results for powders listed in table 6.5. This might imply an even larger oxygen out-diffusion for thin films, possibly related to a different micro structure. Another explanation is derived by considering the following. The structure of the thin film samples does not evolve completely to an untwinned one with equal a and b axes, which would be expected when oxygen out-diffusion is so pronounced. The much enlarged values for α_{hkl} could therefore be a result of a change in (micro) structure occuring due to the oxygen becoming mobile within the crystal. At the same time, oxygen out-diffusion will take place as well, which also has an influence on the crystal structure, like an expansion of the c-axis. However, the effect of the oxygen becoming mobile on the positions of the diffraction peaks is much more pronounced than the effect of oxygen out-diffusion, especially in the case of thin films compared to YBCO powders.

Detailed studies on the structure of thin films, revealed that in general the c-axis of a thin film is slightly larger than that of a bulk material with equal oxygen content [27, 33]. This is attributed to two other factors, besides the oxygen content, that play a role for the c-axis length, namely lattice defects, like grain boundaries or dislocations and ionic disorder. Each of these have different relaxation temperatures in thin films. Oxygen deficiency can be changed and controlled at temperatures lower than 600 °C, while changes in ionic disorder become more pronounced at temperatures higher than 850 °C [34]. The sudden change in c-axis around 250 °C for the films studied here, seems therefore to be a consequence of changes in the oxygen order and/or content. Processes such as grain growth, recrystallization and diffusion of defects, are expected to take place at temperatures higher than approximately 850 °C. Although it is very likely that oxygen diffusion is responsible for the structural changes at the relatively low temperatures in the range 250 °C- 350 °C, the structure does not change to the tetragonal structure completely. It seems that a new orthorhombic equilibrium is reached. At higher temperatures, around 450°C, the oxygen diffusion is even reversed for two of the thin film samples. This is seen in figure 6.4 , where at the temperature plateau of 450 °C the c-axis length decreases again and in figure 6.5 the splitting of the *115* diffraction peak becomes more pronounced. This is consistent with previous

results obtained for YBCO films at 325 °C [35] and 500 °C [36] both of which find that in-diffusion is faster than out-diffusion. In the latter study, it was also found that the presence of water on the film surface significantly enhances the out-diffusion while unaltering the in-diffusion. In the present study it is very likely that water was present on the film surfaces, only not in a controlled way. This complicates matters even more and might explain discrepancies between the results obtained in the different experiments presented here.

Oxygen diffusion in YBCO single crystals and powders has been studied extensively using tracers [37]. The differences and scatter of the diffusion constants obtained for bulk YBCO and thin films (see e.g. overview in [38]) has been ascribed to the difference in microstructure in combination with the anisotropic diffusion process [7, 39]. Nevertheless, the time constants obtained here (see section 6.5.4) for the temporal evolution of changes in the diffraction patterns, agree with those reported for time and temperature dependent resistivity measurements on thin films [40, 41, 42].

From Table 6.4 it is seen that the widths of the reflections evolve faster than their positions. If again oxygen diffusion is the process responsible for the changing crystal structure, the change in position might be a consequence of a changing oxygen content. The change in peak width is then related to the oxygen disordering and increasing the non-uniform strain. Although both processes are a concequence of oxygen diffusion, the results imply that the oxygen disordering is the fastest of the two. This could be explained by assuming that there exists an extra energy barrier for oxygen to diffuse out of the crystal into the surroundings. As discussed before, the presence of water was found to influence the diffusion process, and therefore the assumption of an extra diffusion barrier seems justified.

It has been found by micro-beam X-ray diffraction that the twin domains of fully oxygenated YBCO films are strained at the boundaries while inside they are relaxed [43]. It is conceivable that due to the heat-treatment the rearranging oxygen changes the strain-state of the twin domain, thereby also altering the angle between neighbouring domains. This could in principle happen even without the total oxygen content of the film changing. The oxygen in the ab-plane becoming mobile and destroying long range order in the so-called Ortho-I and Ortho-II phases has been observed in oxygen deficient ($x = 0.5, 0.64$ and 0.65) single crystals at temperatures even lower than 250 °C [44]. The Ortho-II phase consists of alternating chains of oxygen and vacancies along the a-axis (the chains extending along the b-axis), thereby doubling the unit cell to $2a$ along the a-axis. The fact that oxygen is becoming mo-

bile, which can result in a change in microstructure would also explain the present finding of an identical transition temperature T_t in an oxygen environment and in vacuum. If merely oxygen in- or out-diffusion were responsible for the observed structural changes, the oxygen environment would certainly be of influence on the process.

6.7 Summary

Heating pulsed-laser-deposited thin YBCO films up to temperatures as high as 750 °C introduces structural changes that appear irreversible upon cooling to room temperature. The on-set temperature for these changes is around 250 °C, which is independent of gas environment or film thickness, ranging from 10^{-3} mbar to 1 bar flowing oxyen and 60-400nm respectively in the present study. From the widths and positions of the measured diffraction peaks it is concluded that both the composition as well as the microstructure change. Reversal of these changes is possible when reverting to the deposition temperature 780 °C, and then annealing in 1 bar of oxygen in two steps to room temperature. This procedure also restores crystal quality in case the crystalline structure was lost. The changes in microstructure at 250 °C appear mainly to be a consequence of oxygen becoming mobile and rearranging. This is concluded from the widths of the diffraction peaks evolving faster than their positions. The former is due to an increase in non-uniform strain, which is very likely to be related to the oxygen sub-lattice starting to disorder. Both the changing oxygen content and oxygen mobility are diffusion processes. The former being the slowest implies that there is an extra energy barrier to be overcome for oxygen to diffuse out of the crystal.

The orthorhombic-to-tetragonal phase transition appears at temperatures much higher than T_t of 250 °C. It seems that this is very close to the point of decomposition of YBCO. In figure 6.6 it is shown that at 750 °C the diffraction peaks disappeared. Another sample showed similar behaviour at 450 °C, which indicates that there might be large scatter in characteristic temperatures for thin films. Nevertheless, in both cases the reaction was reversed by a standard anneal from 780 °C in two steps to room temperature [9]. The temperatures of 650 °C and 450 °C at which the anneal is stopped for 20 minutes, seem to be temperatures where the oxygen-in-diffusion is taking place. This is seen in figures 6.4 and 6.5 where clearly the diffraction features are changing during the thermal treatment. By use of this standard anneal proce-

dure, the crystal structure can be restored as shown by the reappearence of the Bragg peaks in figure 6.8.

References

[1] H.-J. H. Smilde, H. Hilgenkamp, G. Rijnders, H. Rogalla, D. H. A. Blank, Appl. Phys. Lett. **80** (2002) 4579; J. Gao, W. A. M. Aarnink, G. J. Gerritsma, H. Rogalla, Physica C **171** (1990) 126; J. G. Wen, N. Koshizuka, S. Tanaka, T. Satoh, M. Hidaka, S. Tahara, Appl. Phys. Lett. **68** (1996) 1276.

[2] H. Hilgenkamp, *High-T_c DC SQUID Magnetometers*, Ph.D. thesis, University of Twente, The Netherlands (1995).

[3] H. Hilgenkamp, J. Mannhart, Rev. Mod. Phys. **74** (2002) 485.

[4] H. Hilgenkamp, Ariando, H.-J. H. Smilde, D. H. A. Blank, G. Rijnders, H. Rogalla, J. R. Kirtley, C. C. Tsuei, Nature **422** (2003) 50.

[5] Ariando, *Josephson Junction arrays with d-wave-induced π-shifts*, Ph.D. thesis, University of Twente, The Netherlands (2005).

[6] Zhi-Xiong Cai, Yimei Zhu, *Microstructures and Structural defects in High-Temperature Superconductors*, World Scienti0fic, Singapore, 1998.

[7] W. A. M. Aarnink, R. P. J. IJsselsteijn, J. Gao, A. van Silfhout, H. Rogalla, Phys. Rev. **B45** (1992) 13002.

[8] G. Rijnders, S. Curràs, M. Huijben, D. H. A. Blank, H. Rogalla, Appl. Phys. Lett. **84** (2004) 1150.

[9] R. Bormann, J. Nolting, Physica C **54** (1989) 2148; R. H. Hammond, R. Bormann, Physica C **162-164** (1989) 703.

[10] J. Sapriel, Phys. Rev. **B12** (1975) 5128.

[11] F. Sandiumenge, C. Dubs, P. Görnert, S. Galí, J. Appl. Phys. **75** (1994) 5243.

[12] G. J. McIntyre, A. Renault, G. Collin, Phys. Rev. **B37** (1988) 5148.

[13] R. H. Hammond, V. Matijasevic, R. Bormann, in: R. McDonald, R. Noufi (Eds.), *Science and Technology of thin film superconductors*, Vol. **2**, Plenum Press, New York, 1990, p. 395.

[14] D. B. Chrisey, G. K. E. Hubler (Eds.), *Pulsed laser deposition of thin films*, John Wiley & Sons inc., 1994.

[15] G. Koster, B. L. Kropman, G. Rijnders, D. H. A. Blank, H. Rogalla, Appl. Phys. Lett. **73** (1998) 2920.

[16] T. Tschentscher, P. Suortti, J. Synchrotron Rad. **5** (1998) 286.

[17] B. E. Warren, *X-ray diffraction*, Addison-Wesley, Massachusets, 1969.

[18] R. W. Cheary, E. Dooryhee, P. Lynch, N. Armstrong, S. Dligatch, J. Appl. Cryst. **33** (2000) 1271.

[19] B. E. Warren, Prog. in Metal Phys. **8** (1959) 147.

[20] S. Harkema, S. M. Franken, *Diffraction in Materials Science*, Reader University of Twente (1999).

[21] J. D. Jorgensen, M. A. Beno, D. G. Hinks, L. Soderholm, K. J. Volin, R. L. Hitterman, J. D. Grace, I. K. Schuller, Phys. Rev. **B36** (1987) 3608.

[22] M. Avrami, J. Chem. Phys. **7** (1939) 1103; J. Chem. Phys. **8** (1940) 212; J. Chem. Phys. **9** (1941) 177.

[23] M. Stenger, G. Ockenfuß, M. Reese, T. Königs, R. Wördenweber, C. Barre, J.-Y. Prieur, J. Joffrin, Solid State Commun. **98** (1996) 777–780.

[24] R. J. Cava, B. Batlogg, C. H. Chen, E. A. Rietman, S. M. Zahurak, D. Werder, Phys. Rev. **B36** (1987) 5719.

[25] R. Platzer, I. D. Dumkow, D. W. Tom, J. A. Gardner, J. Tate, J. Mater. Res. **13** (1998) 947.

[26] R. Platzer, I. D. Dumkow, J. A. Gardner, J. Tate, Hyperfine Interact. **120/121** (1999) 325.

[27] J. Ye, K. Nakamura, Phys. Rev. **B48** (1993) 7554.

[28] P. K. Gallagher, Adv. Cer. Mat. **2** (1987) 632–639.

[29] P. Gallagher, Adv. Cer. Mat. **2** (1987) 640–648.

[30] M. Kogachi, S. Nakanishi, K. Nakahigashi, S. Minamigawa, H. Saqsakura, N. Fukuoka, A. Yanase, Jpn. J. Appl. Phys. **27** (1988) L1228–L1230.

[31] J. Mizusaki, H. Tagawa, J. Am. Ceram. Soc. **78** (1995) 1781–1786.

[32] R. J. Cava, B. Batlogg, C. H. Chen, E. A. Rietman, S. M. Zahurak, D. Werder, Phys. Rev. **B36** (1987) 5719.

[33] J. L. MacManus-Driscoll, J. A. Alonso, P. C. Wang, T. H. Geballe, J. C. Bravman, Physica C **232** (1994) 288.

[34] J. Ye, K. Nakamura, Physica C **254** (1995) 113–123.

[35] X. Jin, L. Li, J. Mater. Sci. Lett. **19** (2000) 855–857.

[36] A. Michaelis, E. A. Irene, O. Auciello, A. R. Krauss, J. Appl. Phys. **83** (1998) 7736.

[37] S. J. Rothman, J. L. Routbort, J. E.Baker, Phys. Rev. **B40** (1989) 8852; S. Rothman, J. Routbort, U. Welp, J.E.Baker, Phys. Rev. **B44** (1991) 2326; J. L. Routbort, S. J. Rothman, J. Appl. Phys. **76** (1994) 5615.

[38] E. A. F. Span, H. Wormeester, D. H. A. Blank, H. Rogalla, Mat. Sci. Eng. **B56** (1998) 123.

[39] S. Kittelberger, U. Bolz, R. P. Huebener, B. Holzapfel, L. Mex, Physica C **302** (1998) 93–101.

[40] K. Yamamoto, B. M. Lairson, J. C. Bravman, T. H. Geballe, J. Appl. Phys. **69** (1991) 7189.

[41] H.-U. Krebs, C. Krauns, F. Mattheis, J. Alloy Compd. **195** (1993) 203.

[42] S. Kittelberger, O. M. Stoll, R. P. Huebener, Supercond. Sci. Tech. **11** (1998) 744–750.

[43] W. A. CAldwell, N. Tamura, R. S. Celestre, A. A. MacDowell, H. A. Padmore, T. H. Geballe, G. Koster, B. W. Batterman, J. R. Patel, Phys. Rev. Lett. **92** (2004) 216105.

[44] P. Schleger, R. A. Hadfield, H. Casalta, N. H. Andersen, H. F. Poulsen, M. V. Zimmermann, J. R. Schneider, R. Liang, P. Dosanjh, W. N. Hardy, Phys. Rev. Lett. **74** (1995) 1446; H. F. Poulsen, M. V. Zimmermann, J. R. Schneider, N. H. Andersen, P. Schleger, J. Madsen, R. A. Hadfield, H. Casalta, R. Liang, P. Dosanjh, W. N. Hardy, Phys. Rev. **B53** (1996) 15335.

Chapter 7

Strain-Induced Structural Changes in $YBa_2Cu_3O_{7-x}$ Thin Films on $SrTiO_3$ Substrates

7.1 Introduction

In the previous chapters the pulsed laser deposition processing and conditioning of thin $YBa_2Cu_3O_{7-x}$ films on $SrTiO_3(001)$ substrates has been described. In this chapter, a study of the room temperature structure of these films, which were grown and conditioned in a standard way, is presented. With the film thickness increasing, the influence of the interface between film and substrate is expected to become less important for the structure of the film. Therefore, the structure of the $YBa_2Cu_3O_{7-x}$ (YBCO) films is studied as a function of thickness. As known from bulk material, the superconducting properties of YBCO are highly dependent on the oxygen content, which in turn is directly related to the lattice parameters [1]. With the oxygen content changing from 6 to 7 the crystal structure changes from P4/mmm to Pmmm [2]. The additional oxygen will occupy preferentially the site in the *bc* plane, destroying the tetragonal symmetry. In fact, an oxygen content in between 6 and 7 results in different types of ordering of the oxygen and consequently different phases are formed [3] of which Ortho-I has the highest T_c around 92 K. This phase-transition as a function of oxygen content is of the so-called ferro-elastic kind, because spontaneous strain is the driving force [4]. A consequence of this ferro-elastic strain is that orthorhombic YBCO is twinned with twin walls parallel to the mutually perpendicular *hh0* and $h\bar{h}0$ mirror planes of the tetragonal lattice [5]. This mechanism leads to four different co-existing twin-domain orientations [6] as described in section 6.2.

For orthorhombic YBCO (i.e. Ortho-I with $x \simeq 0$) the bulk lattice parameters are given by $a = 3.822 \pm 0.001$, $b = 3.891 \pm 0.001$ and $c = 11.677 \pm 0.002$ Å [1]. However, due to substrate-induced strain, ultra-thin films will have in-plane lattice parameters comparable to those of the substrate, which are in the case of cubic $SrTiO_3$ (STO) a=b= 3.905 Å. Therefore the film and substrate will have equal in-plane lattice parameters and this is the so-called pseudomorphic phase. In thicker films, i.e. around the so-called critical thickness t_c, the lattice parameters relax towards their bulk values, mainly via formation of misfit dislocations [7, 8, 9]. Therefore a tetragonal-to-orthorhombic phase transition is expected to occur around t_c. This has already been investigated using X-ray diffraction in the case of $GdBa_2Cu_3O_{7-x}$ on STO [10]. It was found that in addition to strain release by formation of misfit dislocations also the type of growth (i.e. columnar-like) and twin-formation have to be taken into account in the total mechanism.

It is expected that since the in-plane lattice parameters of the film are changed due to substrate-induced strain, the c-axis of the film will be affected according to the Poisson ratio. Furthermore, the exact substrate surface-structure, together with the nucleation mechanism, will determine the epitaxial properties [11]. Méchin *et al.* [12] find that the c-axes of film and substrate are perfectly aligned, whereas Maurice *et al.* [13] find a misorientation in the same direction and equal to the miscut angle of the vicinal surface.

In the next section of this chapter a description will be given of the sample preparation, the experimental set-up and the principles of the data treatment. Two methods will be described to characterize the structural properties of the grown films. The first uses the twinning of the samples to determine the difference in in-plane lattice parameters from either Reciprocal Space Maps (RSM) or from ω-scans of *hhl*-type reflections. The second deals with the epitaxial properties of the film with respect to the crystallographic surface of the vicinal substrates.

7.2 Experimental

7.2.1 Sample preparation

Several thin films of different thickness were pulsed-laser deposited in a commonly used way [14]. Prior to deposition the STO substrates were treated chemically after which they were annealed at 950 °C in flowing oxygen for one hour such that they are

single TiO_2-terminated [15]. For the ablation of the target material, which consists of a stoichiometric YBCO pellet, a KrF excimer laser is used, having a wavelength, λ, of 248 nm. The laser beam is focused using lenses which results in a fluence of 1.3 J/cm^2. Typical deposition rates for YBCO are 1 Å/s. After depostion the oxygen pressure is increased to around 0.8 bar and the sample is cooled to room-temperature with two anneal-steps, one at 600 °C and one at 450 °C both lasting 15 minutes. Following this procedure ensures YBCO films with the appropriate oxygen content close to 7 in a reproducible way.

7.2.2 Experimental set-up

All XRD experiments described herein were performed at the end-station ID15C of the high energy beamline ID15 of the European Synchrotron Radiation Facility (ESRF). This beamline consists of an Asymmetric MultipoleWiggler (AMPW) with a critical energy of 44.1 keV which provides the radiation for three independent end-stations. The side-station ID15C is at a fixed angle with the main beam coming from the source and a reflection of a single crystal is used to provide the monochromatic X-ray beam. This single-bounce Si(111) Laue monochromator, which can be bent elliptically to focus in the scattering plane, gives an energy of about 40 keV. A detailed description of the lay-out and elements of this beamline can be found elsewhere [16].

The samples are mounted on a standard Huber 511.1 diffractometer, using two sets of slits on the detector arm in order to diminish the background and obtain a high angular resolution.

Due to the similar lattice parameters of film and substrate, their diffraction peaks overlap in reciprocal space. Especially, since the c-axes differ about a factor of three, all the substrate reflections at the third harmonic from the monochromator overlap with film reflections at the first harmonic. Although the third harmonic is only around 1% of the total incoming beam intensity, the diffracting volume of the substrate is 3-4 orders larger and in addition the substrate can be considered a perfect crystal. This can lead, especially for low order reflections, to such a high signal level of the third harmonic that it saturates the detector. To circumvent this undesired effect, a multilayer consisting of 120 bilayers of WB_4C, was used to suppress higher harmonics. A detailed description about this kind of optical element can be found in ref. [17]. The multilayer used in our set-up was constructed and characterized in the multilayer laboratory at the ESRF. The reflectivity of the first harmonic was measured to be

80% and the suppression of the third harmonic was calculated to be at least 10^3. Monitoring of the higher harmonics contamination, using a NaI(Tl) energy dispersive photon-counting detector, revealed no significant contribution to the measured signal.

7.2.3 Determination of orthorhombicity

Usually in crystallography the angular settings of several reflections of the crystal are used to refine the lattice parameters. In the case of twinned samples this method is not so straightforward, because reflections from different domains are close together in reciprocal space and centring becomes less obvious. The twinning mechanism in YBCO is described in detail in section 6.2. By reciprocal space mapping in the hk-plane of a reflection, the angle δ, indicating the twin angle in the hk-plane and defined by equation 6.1, can be determined from the relative difference Δh and Δk between the domains. In the case of a rocking curve it depends on the position in reciprocal space where the reflection passes through the Ewald sphere. For an *hhl* reflection two of the four domains overlap (see fig. 6.1), and since in this case all four domains have the same Bragg angle three peaks are seen when performing an ω-scan. For the measured angle $\Delta\omega$ between the two outer peaks the following relation holds:

$$\cos(\Delta\omega) = \frac{\cos(4\delta)(h^2(a^{*2}+b^{*2})) + l^2c^{*2}}{h^2(a^{*2}+b^{*2}) + l^2c^{*2}} \tag{7.1}$$

where it is noticed that when l=0, the angle $\Delta\omega$ is independent of $\sin(\theta)/\lambda$. The separation of reflections, expressed in reciprocal lattice units (r.l.u.), is of course still a function of $\sin(\theta)/\lambda$. By centring on the middle peak of several *hhl* reflections an orientation matrix (OM) can be found and the lattice parameters can be refined. Using only *hhl* reflections will result in equal a and b axes, which are the average of the real orthorhombic axes and therefore an OM of the underlying average tetragonal lattice is found. Nevertheless, the lattice parameters can then be determined from the value of η together with the average a and b from the OM.

As many reflections as possible are used to define the OM, resulting in 7 for the thinnest (7 nm) to about 20 for the thickest (400 nm) film. Once the OM is defined, mesh-scans of certain regions in reciprocal space can be performed. Since the splitting of the peaks is a function of $\sin(\theta)/\lambda$, high order reflections will be more suited. Here mainly the *304* and *115* reflections are used.

7.2.4 Determination of film orientation

In order to determine the epitaxial properties of the grown films, the orientation of the film with respect to the substrate has to be regarded. In principle, by comparison of the OM found for the film with the one of the substrate the relative orientation can be determined. However, by using the difference in angular settings of reflections of substrate and film directly, it is also possible to determine the relative orientation. In the latter case any systematic errors, like off-set values of the diffractometer axes, cancel and because several reflections can be used a spread in the determined values can be calculated. Taking two reflections, one of the substrate and one of the film denoted as $\overrightarrow{H}_s$ and $\overrightarrow{H}_f$ respectively, the directions of their scattering vectors are known. For the crystal to be in diffracting position the scattering vector is aligned in the horizontal scattering plane, making an angle $\frac{\pi}{2}-\theta$ with the beam. The directions of these vectors can now be written in the diffractometer-based frame by:

$$\overrightarrow{H}_f = (\sin(\frac{\pi}{2}-\theta_f), \cos(\frac{\pi}{2}-\theta_f), 0) \tag{7.2}$$

$$\overrightarrow{H}_s = (\sin(\frac{\pi}{2}-\theta_s), \cos(\frac{\pi}{2}-\theta_s), 0) \tag{7.3}$$

Using the angular settings of the sample on the diffractometer at these positions, denoted $(\omega_f, \chi_f, \phi_f)$ and $(\omega_s, \chi_s, \phi_s)$, it is possible to calculate the position of $\overrightarrow{H}_f$ at the angular settings of $\overrightarrow{H}_s$. This is done by first rotating $\overrightarrow{H}_f$ back to the zero position and then to the position of $\overrightarrow{H}_s$. In this way two vectors are known, both expressed in the same orthonormal lab-frame so that the angle between them can be calculated. Using the rotation matrices for a four-circle diffractometer as defined by Busing *et al.* [18] the required expression is given by:

$$\overrightarrow{H}'_f = R_{\omega_s,\chi_s,\phi_s} R_{-\phi_f,-\chi_f,-\omega_f} \overrightarrow{H}_f \tag{7.4}$$

where R is the 3×3 rotation matrix.

7.3 Results

Seven samples with thicknesses ranging from 7 to 400 nm were used in the measurements. Reciprocal space mapping of several *hhl* and *h0l*-type reflections is performed from which the orthorhombicity (see eq. 1) is determined. Figure 7.1 shows an *hk*-

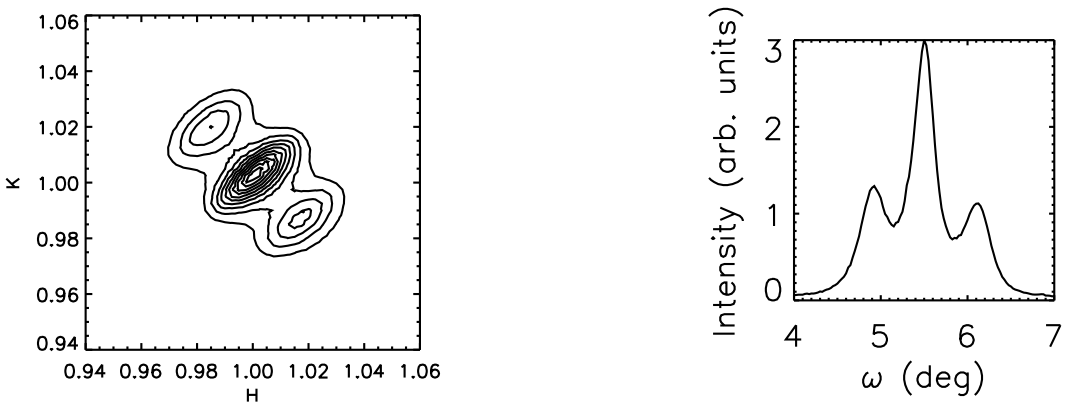

Figure 7.1: An *hk*-mesh (left) of the *115* of a 400nm film and the cooresponding ω-scan (right) of the same reflection.

mesh and the corresponding ω-scan of the *115* reflection of a 400-nm film. The results of the orthorhombicity of all samples are plotted in figure 7.2. The 7 nm film showed no splitting, therefore the orthorhombicity of this film is determined to be 0, without an error bar.

The error bars have been determined by taking the spread in the calculations of the orthorhombicity from several reflections of the same sample. The thickness is estimated from the deposition parameters and therefore no error bars are indicated.

For four samples the miscut angle is determined and also the angle between the c-axes of film and substrate. The results are listed in table 1. Error bars have been determined by calculating the angle using different sets of *00l* reflections for both substrate and film.

7.4 Discussion

Figure 7.2 shows clearly a transition from tetragonal to orthorhombic with increasing film thickness. The solid line in figure 7.2 is obtained by a fit to all data points, except the 7 nm film, of the form:

$$\eta(t) = \eta_{max} + \frac{B}{t} \tag{7.5}$$

The best fit is obtained with parameters $\eta_{max} = 0.0089 \pm 0.0002$ and $B = -0.104 \pm 0.005$. The value for η_{max} corresponds very well with the reported orthorhombicity

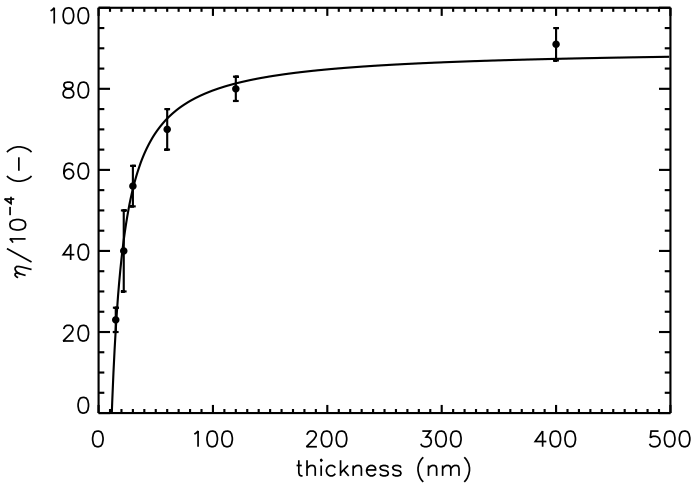

Figure 7.2: Orthorhombicity η as function of film thickness. The solid line is a fit to a $1/t$ behaviour as explained in the text.

of fully oxygenated bulk YBCO with $\eta_{bulk} = 0.0089 \pm 0.0003$, calculated from Cava *et al.* [1]. The midway point of the transition, i.e. for $\eta = \eta_{max}/2$, corresponds to a thickness of $t_{OT} = 23 \pm 1$ nm, where the subscript OT denotes the orthorhombic-to-tetragonal transition. The fit gives a critical thicknes t_c, where $\eta = 0$, of 11.5 ± 0.6 nm, which compares well with reported values in the literature for the critical thickness of YBCO on STO ranging from 8 to 13 nm [10, 19, 20].

The orthorhombicity for a thin film of 30 nm reported here is around $\eta = 0.005$. When taking the bulk data of Cava *et al.* [1] this would correspond to a T_c of 40 K and an accompanying oxygen content with $x \simeq 0.5$. However, T_c measurements on thin YBCO films by Zhai *et al.* [21] reveal for a 30 nm film a T_c of about 88 K, which relates to an oxygen content with $x \simeq 0.1$ and an orthorhombicity of 0.009. This indicates that the STO substrate strains the YBCO film, thereby lowering the orthorhombicity without affecting the oxygen content nor the ordering of oxygen, where the latter is believed to be the fingerprint of the superconducting phase [3].

Comparing the miscut angles with the relative orientation of the film with respect to the substrate it is shown in table 7.1 that up to a miscut angle of 1.2 degrees, the film has grown on the optical rather than the crystallographic surface of the substrate. It is to be noted that the standard deviation in the measurements on the 1.2 degrees

Sample	Miscut (deg)	ξ (deg)	$\sigma(\xi)$ (deg)
120 nm	0.49	0.49	-
60 nm	0.68	0.71	0.05
30 nm	0.69	0.61	0.07
15 nm	1.2	0.8	0.3

Table 7.1: Miscut angle and angle ξ between c-axes of film and substrate. The estimated standard deviations for the values obtained for ξ are denoted $\sigma(\xi)$.

miscut sample is relatively high.

Measurements by Maurice *et al.* [13] on a 200 nm YBCO film on a 0.53 degrees miscut (001) STO substrate, shows the same behaviour. Méchin *et al.* used vicinal (001) STO substrates with miscut angles of 2, 4 and 6 degrees and found that YBCO films grow on the crystallographic surfaces of these substrates.

7.5 Conclusion

It is shown that YBCO films undergo structural changes as function of thickness when grown on STO and that these structural changes can be measured using high energy XRD. Due to substrate-induced strain YBCO films thinner than 11.5 ± 0.6 nm have equal in-plane lattice parameters, whereas above this critical thickness they gradually evolve towards the bulk orthorhombicity of fully oxygenated YBCO. The thickness characteristic for this transition is 23 ± 1 nm.

Furthermore it is shown that thin YBCO films grow up to a miscut angle of about 1.2 degrees on the optical surface of the vicinal STO substrates.

References

[1] R. J. Cava, B. Batlogg, C. H. Chen, E. A. Rietman, S. M. Zahurak, D. Werder, Phys. Rev. **B36** (1987) 5719.

[2] J. D. Jorgenson, M. A. Beno, D. G. Hinks, L. Soderholm, K. J. Volin, R. L. Hitterman, J. D. Grace, I. K. Schuller, Phys. Rev. **B36** (1987) 3608.

[3] H. F. Poulsen, N. H. Andersen, J. V. Andersen, H. Bohr, O. G. Mouritsen, Nature **349** (1991) 321.

[4] J. Sapriel, Phys. Rev. **B12** (1975) 5128.

[5] F. Sandiumenge, C. Dubs, P. Görnert, S. Galí, J. Appl. Phys. **75** (1994) 5243.

[6] G. J. McIntyre, A. Renault, G. Collin, Phys. Rev. **B37** (1988) 5148.

[7] J. P. Contour, A. Défossez, D. Ravelosona, A. Abert, P. Ziemann, Z. Phys. B **100** (1996) 185.

[8] S. K. Streiffer, B. M. Lairson, C. B. Eom, B. M. Clemens, Phys. Rev. **B43** (1991) 13007.

[9] A. D. Vecchio, M. F. D. Riccardis, L. Tapfer, J. Vac. Sci. Technol. A **18(3)** (2000) 802.

[10] L. X. Cao, T. L. Lee, F. Renner, Y. X. Su, R. L. Johnson, J. Zegenhagen, Phys. Rev. **B65** (2002) 113402.

[11] T. Haage, J. Zegenhagen, H.-U. Habermaier, M. Cardona, Phys. Rev. Lett. **80** (1998) 4225.

[12] L. Méchin, P. Berghuis, J. E. Evetts, Physica C **302** (1998) 102.

[13] J.-L. Maurice, O. Durand, M. Drouet, J.-P. Contour, Thin Solid Films **319** (1998) 211.

[14] D. B. Chrisey, G. K. Hubler (Eds.), *Pulsed laser deposition of thin films*, John Wiley & Sons, New York, 1994.

[15] G. Koster, B. L. Kropman, A. J. H. M. Rijnders, D. H. A. Blank, H. Rogalla, Appl. Phys. Lett. **73** (1998) 2920.

[16] T. Tschentscher, P. Suortti, J. Synchrotron Rad. **5** (1998) 286.

[17] D. H. Bilderback, B. M. Lairson, T. W. Barbee, G. E. Ice, C. J. Sparks, Nucl. Instr. and Meth. **208** (1983) 251.

[18] W. R. Busing, H. A. Levy, Acta Cryst. **22** (1967) 457.

[19] K. Kamigaki, H. Terauchi, T. Terashima, K. Yamamoto, K. Hirata, K. Hayashi, I. Nakagawa, Y. Tomii, J. Appl. Phys. **69** (1991) 3653.

[20] J. Zegenhagen, T. Siegrist, E. Fontes, L. E. Berman, J. R. Patel, Solid State Comm. **98** (1995) 763.

[21] H. Y. Zhai, W. K. Chu, Appl. Phys. Lett. **76** (2000) 3469.

Chapter 8

High-Temperature Interface Structure of $SrTiO_3/LaAlO_3$

8.1 Introduction

Recently it has been shown in several publications, that by careful interface/strain engineering, the properties of perovskite thin films may be altered compared to the bulk. In the case of ferroelectric superlattice heterostructures made of $BaTiO_3/SrTiO_3/CaTiO_3$, a 50 % -enhancement of the polarization compared to BaTiO3 was found [1]. Besides strain effects, the different bond configuration at heterointerfaces may result in unexpected conduction phenomena. Since the general structure of the perovskites can be seen as a stack of alternating layers of AO and BO_2, a heterointerface will introduce polarity discontinuities when A and B have different valence states. The resulting properties of these kind of interfaces were discussed for the GaAs/Ge system already in the early days of heteroepitaxy [2]. Recently, Ohtomo and Hwang [3] found different behaviour for thin $LaAlO_3$ films on either SrO or TiO_2 terminated $SrTiO_3$ substrates, the former interface being insulating and the latter conducting. Here, using the formal valence states, the polarity discontinuties are formed by either the $(SrO)^0$-$(AlO_2)^-$ or $(TiO_2)^0$-$(LaO)^+$ sequence. Similar behaviour was found for the LaTiO3/SrTiO3 interface [4]. The intriguing phenomenon of conductivity at the interface between two *insulating* materials has become known as "electronic reconstruction", and progress is being made in a theoretical description [5]. It is well known that the atomic structure of surfaces and interfaces differs in general from the bulk. In order to better understand and model the novel properties of the aforementioned heterointerfaces, it is important to determine the atomic surface structure very accurately. Surface X-ray Diffraction (SXRD) is a well-established technique for the

structure determination of surfaces and interfaces [6]. In contrast to techniques like Transmission Electron Microscopy (TEM), SXRD provides the atomic structure averaged over typically several mm^2, which in general is the surface area illuminated by the X-ray beam. Obtaining structural information that includes microscopic length scales will provide valuable information for a better understanding of the physical properties.

Here we present SXRD studies on the STO/LAO heterointerface grown by Pulsed Laser Deposition (PLD)[7]. The measurements were performed in the same chamber as where the samples were deposited, which assures that the surface is kept in a controlled atmosphere. At the same time, in-situ studies enable to study the heterointerface structure during growth. Knowledge of the atomic stacking sequence at the interface can provide information concerning the nucleation and growth of thin films during PLD. The atomic interface structure and morphology depend strongly on several parameters, of which the difference in lattice parameters between the materials on either side of the interface is very important [1]. Therefore, it is expected that the interface structure and surface morphology may differ as a function of temperature. The aim of the present study is thus twofold: a more general case study of the atomic heterointerface structure of perovskites at high temperatures and, more specific, the atomic structure of an electronically reconstructed heterointerface.

8.2 Experimental

The experiments were carried out using a specially designed PLD chamber [8], which was mounted on a 2+3 type surface diffractometer with vertical scattering geometry at BM26 (DUBBLE) [9] at the European Synchrotron Radiation Facility (ESRF). The X-ray beam was monochromatized to a wavelength of 0.775(1) Å. Optically polished $SrTiO_3$ (001) (spacegroup $Pm\bar{3}m$ with a=3.901(1) Å at room temperature[10]) substrates were obtained from Surfacenet GmbH, Rheine, Germany. A special treatment of these substrates results in single TiO_2-terminated surfaces [11]. A single crystal of $LaAlO_3$ (LAO) was used as a target. The bulk crystal structure of LAO, having spacegroup $R\bar{3}c$ with a=5.36462(4) Å and c=13.1096(1) Å at room temperature [12], can be represented by a pseudo-cubic unit cell with $a_{cub} = \sqrt{\frac{1}{3}a_{hex}^2 + \frac{1}{36}c_{hex}^2}$ resulting in a_{cub}=3.790 Å. Two different substrates were used in two different experiments. In both case, during deposition the substrate temperature was kept at 1123K,

while the pressure in the chamber was around 10^{-4} mbar oxygen, which are close to the ideal conditions for LAO growth [4]. At a grazing angle of around 1° for the incoming X-ray beam, the intensity of a surface-sensitive reciprocal space point *00l* in STO lattice units was monitored while depositing. For both experiments, the deposition was stopped after a coverage less than one complete unit cell layer LAO. One sample was then cooled to 473K while the other sample was kept at the deposition temperature of 1123K. For both samples several Crystal Truncation Rods (CTR's) were measured. The reciprocal point *(2,0,1.9)* was recorded several times during data collection of the sample at 1123K, which provides some information about the stability of the surface. Over 6 hours the integrated intensity of this particular point fluctuated 4% around its average value, which is an indication that at least the crystal structure of the monolayer maintained stable. For the sample that was cooled to 473K, the reflectivity ridge scan before and after the data collection showed no significant differences, indicating that also this sample was stable.

8.3 Results

For both samples several CTR's were measured, the details of which are listed in table 8.1. The measured diffraction profiles were integrated and corrected in a standard way in order to obtain structure factors [13]. Due to limited access to reciprocal space, it was not possible to measure symmetry related reflections. In the absence of redundancy of the measured data, the systematic errors were estimated at 15 %, which seems realistic in view of previous data collections on bare STO substrates (see chapter 3).

Next the measured data were described by a structural model, in which a TiO_2-terminated STO substrate is partly covered by a unit cell layer of LAO. The fraction of the substrate that is covered by LAO, is a priori not known. Since it is conceivable that the surface atoms in the STO lattice in the part of the substrate that is covered by LAO will distort, a model is needed in which the total interference sum of both distorted and undistorted part is taken by:

	1123K	473K
no. points	60	45
CTR's (hk)	*10,11,20,21*	*10,11,20*
θ_1	0.38(2)	0.48(1)
θ_2	0.57(1)	0.50(1)
$\theta_1 + \theta_2$	0.95(2)	0.97(2)
χ^2 [a]	2.1	2.6

[a] $\chi^2 = \frac{1}{N-p-1} \sum_{hkl} \frac{(|F_{obs}(hkl)| - s|F_{calc}(hkl)|)^2}{\sigma^2(F_{obs}(hkl))}$, with N the number of observed structure factors, p the number of refined parameters and s the overall scalefactor.

Table 8.1: Details of the datasets obtained from two different samples at two different temperatures and the final results of the refinement of the model as described in the text and given in equation 8.1. The values for θ_1 and θ_2 are the fractions of the substrate that are uncovered and covered by the LAO layer respectively. The resulting refined atomic positions are listed in table 8.2.

$$F_{sum} = \frac{F_{\mathrm{STO}}}{1 - e^{-i2\pi l} e^{-\alpha}} + \theta_1 F_{\mathrm{STO}} + \theta_2 (F'_{\mathrm{STO}} + F_{\mathrm{LAO}}) \tag{8.1}$$

Here, F_{STO} is the structure factor of bulk STO, and the first term on the right-hand side renders the well-know CTR of the bulk STO substrate. The fraction θ_1 is the uncovered part of the substrate surface and θ_2 is the fraction of the substrate surface (F'_{STO}) that is covered by LAO (F_{LAO}). Since the covered part of the substrate surface relaxes, it follows that $F'_{\mathrm{STO}} \neq F_{\mathrm{STO}}$. In the model it is assumed that the uncovered part is bulk-terminated, which is based on the results presented in chapter 3. The program ROD [14] was used to refine the atomic positions against the experimental data. The results of the refined atomic positions are listed in table 8.2 and the measured and calculated CTR's are shown in figure 8.1.

Since the fractional occupancies were not constrained as $\theta_1 = 1 - \theta_2$, the two parameters were refined independently, and their values are listed in table 8.1. Finally, a schematic view of the atomic positions of the refined model at 473K is shown along one principal crystallographic direction in figure 8.2.

Layer	Atom	x	y	z_{1123K}	z_{473K}	B_{1123K} (Å^2)	B_{473K}(Å^2)
AlO_2\{	Al	$\frac{1}{2}$	$\frac{1}{2}$	1.99(1)	2.031(8)	2.0	1.0
	O1	$\frac{1}{2}$	0	1.99(2)	1.88(2)	3.0	2.0
LaO\{	La	0	0	1.536(4)	1.565(2)	2.0	1.0
	O2	$\frac{1}{2}$	$\frac{1}{2}$	1.58(5)	1.40(2)	3.0	2.0
TiO_2\{	Ti	$\frac{1}{2}$	$\frac{1}{2}$	1.01(1)	0.997(6)	1.6	0.7
	O3	$\frac{1}{2}$	0	1.04(2)	0.92(2)	2.6	1.5
SrO\{	Sr	0	0	0.513(5)	0.536(3)	2.2	1.2
	O4	$\frac{1}{2}$	$\frac{1}{2}$	0.57(3)	0.51(2)	2.6	1.5

Table 8.2: Refined fractional co-ordinates of the best fit model as described in the text for the two different samples at two temperatures as well as the isotropic thermal parameters B, used in the refinement procedures. The same labeling for the atoms is used as in the schematic view of the model shown in figure 8.2.

8.4 Discussion

Besides the model discussed in the previous section, other models, having different atomic interface stackings, were tested, such as: bulk-SrO-AlO_2-LaO, bulk-SrO-LaO-AlO_2 (Ruddlesden-Popper phase [15]), bulk-TiO_2-AlO-LaO_2 and bulk-TiO_2-AlO_2-LaO (where the AlO_2-LaO layer is displaced by the in-plane vector $(\frac{1}{2}, \frac{1}{2}, 0)$). None of these models describes the data very accurately. As a comparison with the best fit model, figure 8.1 shows CTR's that are calculated by using two bulk-like terminated models for a Sr and a Ti-terminated substrate. In those two cases, the interatomic distances across the STO-LAO interface are kept at the bulk STO lattice parameter, thereby simulating as if the STO lattice is continued only Ti is substituted by Al and Sr by La. Assuming interatomic distances across the interface given by the bulk lattice parameter of LAO, means an even larger difference with the obtained best fit and is therefore not shown.

Allowing more STO unit cell layers in the bulk to distort as well, resulted in negligible atomic displacements for these layers and in order to reduce the number of fit parameters only the first STO unit cell layer was allowed to distort in the final fit. Attempting to refine the thermal parameters resulted in very large estimated standard deviations (e.s.d.'s). In the final fits, the thermal parameters were kept at bulk-like values (see table 8.2) inferred from literature [10, 12].

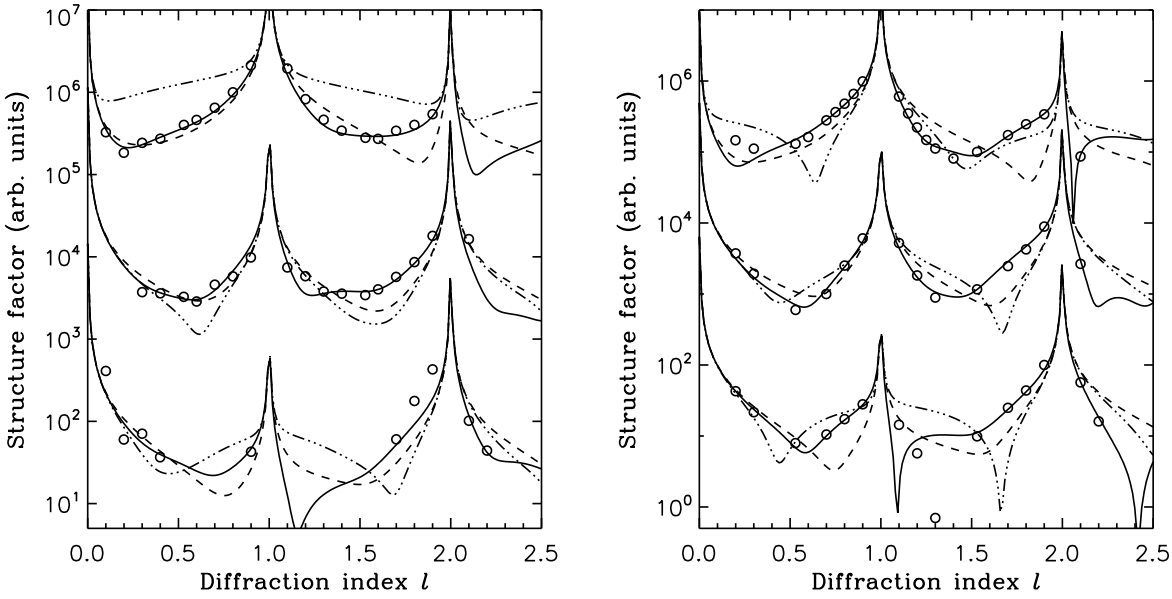

Figure 8.1: Measured data points and calculated CTR's using three different models as described in the text. Both the data and modeled CTR's are shown for the measurements taken at 1123K (left) and 473K (right). For both temperatures the 10 (top), 11 (middle) and 20 (bottom) rods are shown. The solid lines are the CTR's calculated using equation 8.1 and the atomic positions as listed in Table 8.2. For comparison, also a bulk-like termination is tested, by which is meant a continuation of the STO lattice only by substituting Sr by La and Ti by Al. For that model, calculated CTR's are shown for bulk-TiO_2-LaO-AlO_2 (dashed line) and bulk-SrO-AlO_2-LaO (dah-dotted) interface stackings.

In order to better understand the final refined model, some of the interatomic distances are listed in table 8.3. Clearly, almost all the atoms in the high-temperature interface (1123K) structure, are within two times the e.s.d. from a bulk STO lattice site. In contrast to the low-temperature (473K) interface structure, where the displacements from the bulk STO lattice sites are statistically relevant. Starting from the bulk underneath, the Ti are both at high and low temperature in a bulk position. The Al, that follows on top of the Ti in a crystallographically similar position, is at low temperature displaced away from the surface and bulk STO lattice site. The Sr and La, that are on the A-sites of the general ABO_3 structure, seem to behave differently. Again at high temperature both the Sr and La are practically on bulk lattice sites, whereas at low temperature the atoms displace away from the surface, resulting in quite large distances compared with the bulk lattice parameters of both

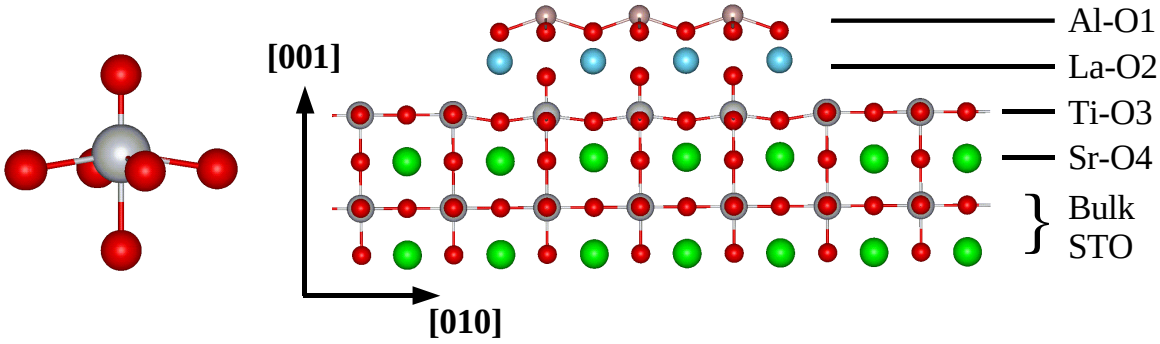

Figure 8.2: Schematic view of the model with the interface stacking bulk-TiO_2-LaO-AlO_2 after refinement against the dataset obtained at 473K. For clarity the projection along the [100] direction is shown. The part of the STO that is covered by the LAO is slightly distorted, wheras the uncovered part of the STO remains bulk terminated. The atomic fractional co-ordinates are listed in Table 8.2. On the left the distorted surface TiO_6 octahedron is enlarged for clarity.

LAO and STO. The oxygens show similar behaviour, i.e. the displacements are much larger at low temperature and at high temperature they reside practically at a bulk STO lattice site. However, the anions displace in the opposite direction from the cations and furthermore the displacements are much larger. Finally, the interatomic distances between the cations across the interface becoming as large as 4.09 Å is not expected, since the LAO unit cell is dilationally strained in-plane, which normally implies that the out-of-plane interatomic distances shorten. The results here seem to imply a negative Poisson ratio, a very rare phenomenon. It has to be mentioned that this result is obtained by using the bulk lattice parameter of LAO in the calculation, and therefore does not represent an independent observation.

	1123K (Å)	473K (Å)	1123K ($\frac{d}{a_{sto}}$)	473K ($\frac{d}{a_{sto}}$)
a_{STO}	3.935(5)	3.915(5)	-	-
a_{LAO} [a]	3.824	3.797	-	-
d_{Al-Ti}	3.86(4)	4.03(4)	0.98(1)	1.03(1)
d_{La-Sr}	4.03(2)	4.03(2)	1.023(6)	1.029(6)
d_{O1-O3}	3.7(1)	3.8(1)	0.95(3)	0.96(2)
d_{O2-O4}	4.0(2)	3.5(1)	1.01(6)	0.90(3)
$d_{bulk-Ti}$	3.97(4)	3.90(2)	1.01(1)	0.997(6)
$d_{bulk-Sr}$	3.99(2)	4.06(1)	1.013(5)	1.036(3)
$d_{bulk-O3}$	4.09(8)	3.60(8)	1.04(2)	0.92(2)
$d_{bulk-O4}$	4.2(1)	3.95(8)	1.07(3)	1.01(2)

[a] In pseudo-cubic notation estimated from values reported by ref. [12]

Table 8.3: Overview of the interatomic distances obtained from the refinement of the model as described in the text. Both the absolute and fractional distances, related through the bulk lattice parameter of STO, are listed. For both temperatures, the bulk lattice parameter of STO (a_{STO}) was obtained from the experiments and the bulk lattice parameter of LAO (a_{LAO}) was estimated from reference [12]. The values $d_{bulk-atom}$ indicate the distance from the particular atom to the nearest identical atom-type in the bulk. The same numbering for the atoms is used as in table 8.2 and figure 8.2.

The results of the low temperature interface structure here, compare very well with results obtained by Maurice *et al.*[16]. They studied thin LAO films of several nanometers on STO substrates by high resolution transmission electron microscopy (HRTEM). The measurements obtained in those studies revealed that on either side of the STO/LAO interface the atomic layers are dilated. Their results indicate that at room temperature the last three STO unit cell layers expand up to 4.05 Å and that the first three LAO unit cell layers distort in a similar fashion. Here, the studied interfaces consist of much thinner films, which might be the cause of the distortions to be found only in the last unit cell layer of STO. Nevertheless, the distances d_{Al-Ti} and d_{La-Sr} across the low temperature interface compare very well with the HRTEM results.

The atomic displacements found here and by HRTEM result in a distortion of the topmost TiO_6 octahedra (see fig. 8.2). In bulk STO, these octahedra are symmetric,

whereas for the low temperature interface they are distorted to become asymmetric. Furthermore, the Ti is displaced and not centred in the oxygen octahedron anymore. This seems to be a combination of two commonly observed distortions from the perfect cubic perovskite structure [17]: Jahn-Teller effect and ferro-electric-like. The term ferro-electric should not be taken strictly as being the ability to switch between two different polarization states. The term is used here only to address the similarity with for example $BaTiO_3$, where the Ti displaces off-centre in the oxygen octahedra in the ferro-electric state. The distorted oxygen octahedron originating from a Jahn-Teller effect was discussed by Maurice *et al.* and ascribed to the Ti changing its valence state from 4+ to 3+, which means that the extra electron occupies a previously unoccupied d-shell state. Indeed, in similar perovskite structures, like $FeCuO_3$, the octahedron distortion may become as large as 20 %, i.e. one axis becoming longer, making the current 10 % distortion not unrealistically large. However, these kind of distortions usually take place in bulk materials. The presence of a surface in this case will certainly influence the crystal field and implies dangling bonds. Furthermore, the fact that the high-temperature interface structure does not differ too much from having a STO bulk terminated crystal in which the topmost Ti and Sr atoms are replaced by Al and La respectively, seems to contradict a Jahn-Teller effect: why would at high temperatures the valence state of the Ti be unchanged? Understanding the interface structure and the differences between the high and low-temperature interface, might be complicated further by the temperature dependence of the structure of LAO. At room temperature, LAO has the rhombohedral structure, which differs from the perfect cubic structure by the rotation of the oxygen octahedra about its three-fold axis. At 821 K the structure transforms to become cubic ($Pm\bar{3}m$) [18]. Although the rhombohedral structure differs only little from cubic (less than the distortions found here), the driving force for the phase transition might be of importance to understand the current distortions.

8.5 Conclusion

High-temperature SXRD was employed just after the PLD growth on the LAO/STO interface. Two crystallographic data sets were obtained, one at the deposition temperature of 1123K and in another deposition run at 473K. The model that fits the experimental data best, is that of a fractionally covered TiO_2-terminated substrate.

The uncovered part of the substrate remains bulk terminated while the interface atoms of the covered part distort. At high temperatures, the atomic displacements in the interface region are comparable to the error bars. At the lower temperature of 473K, the distortions do become significant, whereby the anions displace towards and the cations away from the underlying substrate. The interatomic distances across the interface between STO and LAO of around 4.1 Å found here, compare very well with HRTEM measurements performed on similar interfaces by Maurice *et al.* [16].

The results obtained here suggest that at deposition temperature the atoms in the interface region occupy positions very close to bulk STO lattice sites. At the lower temperature of 473K however, the results indicate the interface atoms to be displaced from the ideal bulk STO lattice sites. The oxygen octahedron around the topmost Ti is strongly distorted in two ways. First the octahedron is not symmteric anymore and second the Ti is displaced off-centre. These distortions are common to other perovskite materials and might be the key to understand the conduction phenomena observed for this interface.

References

[1] H. N. Lee, H. M. Christen, M. F. Chisholm, C. M. Rouleau, D. H. Lowndes, Nature **433** (2005) 395–399; G. Rijnders, D. H. A. Blank, Nature **433** (2005) 369–370.

[2] G. A. Baraff, J. A. Appelbaum, D. R. Hamann, Phys. Rev. Lett. **38** (1977) 237; W. A. Harrison, E. A. Kraut, J. R. Waldrop, R. W. Grant, Phys. Rev. **B18** (1978) 4402.

[3] A. Ohtomo, H. Y. Hwang, Nature **427** (2004) 423–426.

[4] A. Ohtomo, D. A. Muller, J. L. Grazul, H. Y. Hwang, Nature **419** (2002) 378–380.

[5] S. Okamoto, A. J. Millis, Nature **428** (2004) 630–633; S. Okamoto, A. J. Millis, Phys. Rev. **B70** (2004) 075101; S. Okamoto, A. J. Millis, Phys. Rev. **B70** (2004) 241104.

[6] I. K. Robinson, Handbook on Synchrotron Radiation, Vol. **3**, North-Holland, Amsterdam, 1991, Ch. 7, pp. 221–266.

[7] D. B. Chrisey, G. K. Hubler, Pulsed Laser Deposition of Thin Films, John Wiley and Sons, New York, 1994.

[8] V. Vonk, S. Konings, L. Barthe, B. Gorges, H. Graafsma, J. Synchr. Rad. **12** (2005) 833.

[9] M. Borsboom, W. Bras, I. Cerjak, D. Detollenaere, D. G. van Loon, P. Goedtkindt, M. Konijnenberg, P. Lassing, Y. K. Levine, B. Munneke, M. Oversluizen, R. van Tol, E. Vlieg, J. Synchr. Rad. **5** (1998) 518.

[10] Y. A. Abramov, V. G. Tsirelson, V. E. Zavodnik, S. A. Ivanov, I. D. Brown, Acta Cryst. **B51** (1995) 942.

[11] G. Koster, B. L. Kropman, G. Rijnders, D. H. A. Blank, H. Rogalla, Mater. Sci. Eng. **B56** (1998) 209.

[12] B. Chakoumakos, D. Schlom, M. Urbanik, J. Luine, J. Appl. Phys. **83** (1998) 1979.

[13] E. Vlieg, J. Appl. Cryst. **31** (1998) 198.

[14] E. Vlieg, J. Appl. Cryst. **33** (2000) 401.

[15] S. N. Ruddlesden, P. Popper, Acta Cryst. **11** (1958) 54.

[16] J.-L. Maurice, C. Carretero, M.-J. Casanove, K. Bouzehouane, S. Guyard, E. Laquet, J.-P. Contour, Preprint **cond-mat/0511123**.

[17] H. Megaw, *Crystal Structures: A Working Approach*, W.B. Saunders Company, Philadelphia, 1973.

[18] C. Howard, B. Kennedy, B. Chakoumakos, J. Phys: Condens. Matter **12** (2000) 349–365.

Appendix A

Determination of Epitaxial relationships

The epitaxial relationship between film and substrate determines to a great extent the total scattering pattern of the bicrystal. Ideally, the two orientation matrices (OMs) of the bicrystal mounted on a diffractometer, are determined to define the orientations of the six lattice parameters in the laboratory frame. A well-defined OM requires the angular positions of several, say ten, reflections, preferably in different quadrants of reciprocal space. For in situ measurements, where due to temperature ramps the sample often moves, it is not very practical to define an OM at each different stage of the experiment. Furthermore, due to the sample chamber certain parts of reciprocal space are inaccessible and often only a limited time-window is available for measurements. A faster and therefore more convenient way of determining the epitaxial relationship between film and substrate, is by use of only two reflections. Though less accurate, it still may provide precise enough relative orientations. A prerequisite is a very well aligned instrument. First, the laboratory frame is defined. The X-ray beam travels in the y-direction, and the surface normal is well-aligned along the z-direction, which, by convention for the so-called vertical scattering geometry considered here, is horizontal [1]. In what follows, it is very important that the surface normal is accurately aligned, because the set of basis vectors that will be used in the calculations are defined with respect to the surface. A convenient way of accurate alignment is by use of a laser reflecting off the surface, where easily by using long lever arms an accuray of 0.005^{o} can be achieved. The direction of a certain scattering vector can be expressed in the surface frame, from the angular settings on a $2 + 2$-type diffractometer. Therefore, the incoming and outgoing wave vectors in the surface frame are expressed as:

$$\frac{\mathbf{k}_{i,surf}}{K} = \mathrm{M}\mathbf{y} \tag{A.1}$$

$$\frac{\mathbf{k}_{o,surf}}{K} = \mathrm{M}\Delta\Gamma\mathbf{y} \tag{A.2}$$

with,

$$K = \frac{2\pi}{\lambda} \tag{A.3}$$

the length of the wave vector and λ the wavelength. The angular settings for the sample (β_{in}) and for the detector (δ, γ) determine the orientation matrices by:

$$\mathrm{M} = \begin{pmatrix} 1 & 0 & 0 \\ 0 & \cos(\beta_{in}) & \sin(\beta_{in}) \\ 0 & -\sin(\beta_{in}) & \cos(\beta_{in}) \end{pmatrix} \tag{A.4}$$

$$\Delta = \begin{pmatrix} \cos(\delta) & \sin(\delta) & 0 \\ -\sin(\delta) & \cos(\delta) & 0 \\ 0 & 0 & 1 \end{pmatrix} \tag{A.5}$$

$$\Gamma = \begin{pmatrix} 1 & 0 & 0 \\ 0 & \cos(\gamma) & -\sin(\gamma) \\ 0 & \sin(\gamma) & \cos(\gamma) \end{pmatrix} \tag{A.6}$$

The scattering vector is then obtained in the usual way by:

$$\mathbf{H} = \mathbf{k}_{o,surf} - \mathbf{k}_{i,surf} \tag{A.7}$$

Given the angular positions of a reflection of the film and of the substrate, yields two different vectors $\mathbf{H}$, from which their relative orientation may be deduced. Furthermore, for the vicinal surfaces discussed here, the miscut angle is obtained in a straightforward way using equation A.7. Figure A.1 shows the vector construction of two positions in reciprocal space: a Bragg point and a point on the corresponding CTR.

In the case shown here, the miscut angle is obtained by calculating the vector product of the difference vector ($\mathbf{H}_{\mathrm{STO}} - \mathbf{H}_{\mathrm{CTR}}$) and the surface normal, which in the present case is is $\mathbf{z}$.

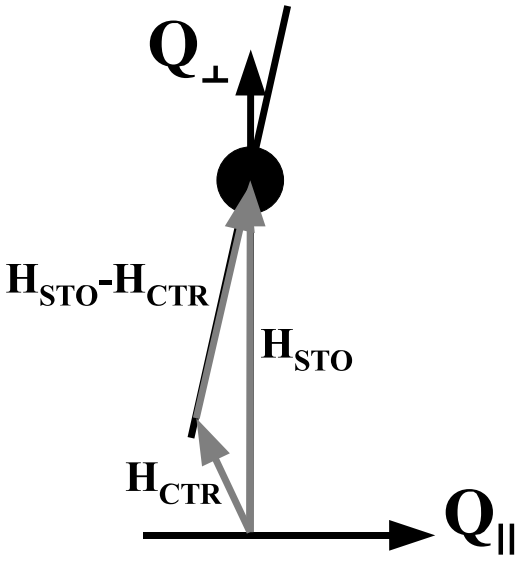

Figure A.1: Vector construction in reciprocal space of a vicinal surface. Shown are the Bragg point ($\mathbf{H}_{\mathrm{STO}}$) and a point on the corresponding CTR ($\mathbf{H}_{\mathrm{CTR}}$). The difference of the two vectors ($\mathbf{H}_{\mathrm{STO}} - \mathbf{H}_{\mathrm{CTR}}$) gives the direction of the miscut. The angle of the msicut is obtained by evaluating the vector product $(\mathbf{H}_{\mathrm{STO}} - \mathbf{H}_{\mathrm{CTR}}) \cdot \mathbf{z}$.

By use of the rotation matrices, as defined previously, the Bragg angle θ can be calculated very easily as well. Since the angle between the incoming and diffracted beams equals 2θ, the position of the detector defines the direction of the diffracted beam by:

$$\mathbf{k}_{\mathrm{o}} = \Gamma\Delta\mathbf{y} = \begin{pmatrix} \sin(\delta) \\ \cos(\gamma)\cos(\delta) \\ \sin(\gamma)\sin(\delta) \end{pmatrix} \tag{A.8}$$

It is not necessary to calculate the vectors in the surface frame, because only the angle between $\mathbf{k}_o$ and $\mathbf{k}_i = \mathbf{y}$ is of interest. The vector product leads to:

$$\cos(2\theta) = \cos(\gamma)\cos(\delta) \tag{A.9}$$

which together with $q = 4\pi\frac{\sin(\theta)}{\lambda}$ leads to

$$|\mathbf{q}| = \frac{4\pi}{\lambda}\sqrt{\frac{1}{2}\left(1 - \cos(\gamma)\cos(\delta)\right)} \tag{A.10}$$

for the magnitude of the momentum transfer.

References

[1] E. Vlieg, J. Appl. Cryst. 30 (1997) 532–543.

Summary

Complex oxide materials form a technologically promising class of materials due to the wealth of physical properties they comprise. Using these materials in heteroepitaxial thin film form, introduces challenging obstacles concerning the growth and results often in structures with unexpected physical properties. The structural discontinuity across the interface between the substrate and film has a large effect on the nucleation, growth and final atomic stacking. This thesis describes a study aiming at clearifying the atomic structure during and after growth of several complex oxide thin film heteroepitaxial systems. Growth is established by Pulsed Laser Deposition (PLD), which has proven to be an excellent technique for complex oxides. PLD makes use of a powerful laser to ablate target material, which is deposited via a plasma on a heated single crystal substrate. Because the laser is operated in a pulsed manner, growth can be controlled very accurately, since with each pulse only a fraction of a monolayer is deposited. On the substrate surface, kinetics plays an important role in the nucleation and growth mechanisms. In order to obtain a picture of the atomic structure evolution as a function of time, X-ray diffraction techniques are well suited. Since the technique is non-destructive and X-rays interact only weakly with matter, it is possible to follow the structural evolution of the films during growth and model the diffracted intensities. By special choice of the diffraction geometry, it is possible to obtain a high surface sensitivity. The technique of Surface X-ray Diffraction (SXRD) is extremely sensitive to surface roughness, and allows therefore also to study the surface morphology during growth.

Chapter 3 describes the atomic surface structure of $SrTiO_3(001)$, which is the commonly used substrate for the thin films studied in this thesis. A special treatment, consisting of chemical etching and annealing, renders high-quality surfaces. From atomic force microscopy measurements, it has been known already that this particular surface is single terminated and atomically flat on a macroscopic scale. In order to determine in more detail the atomic structure, SXRD experiments were

carried out. The main result of this study is that in air and at room temperature the surface has a TiO_2 termination, with slight rumpling and is covered by an oxygen overlayer. The origin of this oxygen layer is not clear at present, and unfortunately the used method of SXRD does not allow for verifying whether the oxygen atoms belong to (dissociated) water molecules.

In chapter 4 the design of a small sample chamber, to be used for studying the PLD process in situ by SXRD, is presented. The chamber was successfully tested concerning the heating of the walls while the oxygen pressure was at 1 bar inside the chamber. Furthermore, the chamber was implemented at a synchrotron beamline, where it was successfully used for the study of the homoepitaxial growth of $SrTiO_3$.

Chapter 5 is devoted to the study of the PLD growth of the high-T_c-superconductor $YBa_2Cu_3O_{7-x}$ (YBCO). Monitoring the intensity close to the reciprocal space point $(0, 0, \frac{1}{2})$ in YBCO lattice units during growth, results in an oscillatory pattern whose main feature consists of alternating high and low maxima. Each maximum corresponds to the completion of another unit cell layer YBCO, which is concluded from thickness and c-axis measurements. Quantitatively the intensity growth oscillations can be understood by considering that, at this particular point in reciprocal space, two consecutive unit cell layers scatter out of phase, thereby canceling each others contributions. Therefore, there are two possibilities for the total scattered intensity given by whether an odd or even number of YBCO unit cell layers contribute to the scattering. In the case that absorption is ignored, an odd number of layers is equivalent to the substrate scattering and *one* unit cell layer YBCO, while an even number of layers is equivalent to only the substrate scattering.

From the YBCO phase-diagram, it is known that at PLD growth conditions, the tetragonal, non-superconducting phase is stable. In order to obtain superconducting, orthorhombic thin YBCO films, it is necessary to cool down to room temperature in an oxygen environment close to 1 bar. The phase transformation is caused by the diffusion of oxygen into the lattice and preferentially occupying a site in the *bc*-plane. In order to obtain a better understanding of the oxygen diffusion and subsequent ordering, several experiments, described in chapter 6, have been performed where thin orthorhombic YBCO films were thermally cycled in different oxygen environments. In contrast to similar experiments performed on YBCO powders, the thin films show drastic irreversible structural changes around 250 °C, irrespective of the oxygen partial pressure. This can be understood by considering that YBCO is in a non-equilibrium state, and that by gently heating the crystals oxygen mobility is

activated within the crystal. Previous experiments on single crystals have found that even at lower temperatures, around 100 °C oxygen mobility becomes important and oxygen disordering takes place. The proposed mechanism, in which oxygen mobility is important is further enhanced by evaluating the temporal evolution of the diffraction patterns. It is shown that the widths of a reflection evolves faster than its position. Assuming that the position is related to the total oxygen content of the crystal and the width to the ordering, it may be assumed that oxygen disordering takes place before oxygen diffuses in or out of the crystal lattice. This could be caused by the presence of an extra diffusion barrier across the crystal/vaccum interface. This can explain why at a temperature of 250 °C, much lower than the known orthorhombic-to-tetragonal phase transition temperature of around 650°C, drastic changes in the microstructure can occur.

In chapter 7 the structural thickness dependence of thin YBCO films is studied. Since the in-plane lattice parameters of film and substrate are not identical, films are strained. The thicker the film, the more strain energy is stored, up to the point that it becomes favorable to introduce dislocations. The point indicating this phenomenon is the so-called critical thickness. Films thinner than the critical thickness are in the so-called pseudomorphic phase, meaning that their in-plane lattice parameters are equal to those of the substrate. As a consequence of unequal in-plane lattice parameters in bulk YBCO, twin domains are formed. The upper limit of the pseudomorphic phase was studied by determining the angle between twin domains as a function of thickness. It is expected that in the pseudomorphic phase twinning is absent, making it possible to determine the critical thickness. Several different films were used in the measurements, after which a value $t_c = 11.5(6)$ nm was found for the critical thickness, which agrees very well with values reported in literature. Furthermore it was found that above the pseudomorphic phase transition, the lattice parameters evolve gradually towards their bulk values, with a mid-way point of 23(1) nm. Comparing this gradual structural transition with reported values of the superconducting phase transition temperature of thin films, results in the conclusion that in this thickness range the well-established relation between T_c and bulk crystal structure does not hold.

Finally in chapter 8 the high-temperature interface structure of a $SrTiO_3(001)$ surface covered by a fractional unit cell layer of $LaAlO_3$ is presented. Recently it was reported that the interface between these two insulating materials becomes conducting. Also from the point of view of growth of complex oxides it is an interesting

system, because ultra-thin layers proved to be stable for many hours, enabling to measure extensive data sets. Two different samples were prepared, both at a deposition temperature of 850°C. Then one of the samples was kept at deposition temperature and several Crystal Truncation Rods (CTRs) were measured. The other sample was cooled to 200°C after which several CTRs were measured. The resulting model for the sample measured at 850°C shows atomic displacements that are in the same range as their error bars, making it not possible to clarify the structure. The resulting model for the structure measured at 200°C however, does show atomic displacements up to 10 % of their ideal positions that are significant. These atomic displacements introduce a large polarization, similar to that found in ferro-electrics. The origin of these lattice distortions remains unresolved for the moment.

Samenvatting

Complexe oxiden vormen een groep materialen, die technologisch gezien veelbelovend zijn, vanwege de enorme rijkdom aan fysische eigenschappen die omvat worden. Het toepassen van deze materialen in de vorm van een heteroepitaxiale dunne film, introduceert enkele uitdagende problemen wat betreft de groei en resulteert vaak in onverwachte fysische eigenschappen van het eindproduct. De discontinuïteit van de kristalstruktuur op het grensvlak tussen film en substraat, heeft een grote invloed op de nucleatie, groei en uiteindelijk atoomstapeling. In dit proefschrift wordt een studie beschreven, die tot doel heeft om de atomaire struktuur van heteroepitaxiale complexe oxiden te beschrijven tijdens en na afloop van de dunnefilmgroei. Deze groei wordt tot stand gebracht via zogenaamde Gepulste Laser Depositie (GLD), waarvan gebleken is dat het een uitstekende techniek is voor de groei van complexe oxiden. GLD maakt gebruik van een krachtige laser die het gewenste materiaal ableert, waarna dit materiaal via een plasma naar het verwarmde substraat getransporteerd wordt. De laser werkt met pulsen, wat resulteert in een zeer gecontroleerde groei, omdat met iedere laserpuls slechts een fractie van een eenheidscellaag gedeponeerd wordt. Op het substraatoppervlak speelt kinetiek een belangrijke rol voor de nucleatie en groei van het kristal. Om een beter beeld te krijgen van de kristalstruktuur op atomair niveau tijdens de groei, zijn Röntgen Diffractie (RD) technieken uitermate geschikt. Door een speciale diffractie geometrie te kiezen, bereikt men extreme oppervlaktegevoeligheid. Deze techniek wordt ook wel Oppervlakte Röntgen Diffractie (ORD) genoemd. ORD is gevoelig voor oppervlakteruwheid, wat het mogelijk maakt om de oppervlaktemorfologie te bestuderen tijdens de groei.

Hoofdstuk 3 beschrijft een studie naar de atomaire oppervlaktestruktuur van $SrTiO_3(001)$, hetgeen het gebruikte substraat is voor alle studies die in dit proefschrift beschreven worden. Door middel van een speciale behandeling, bestaande uit chemisch etsen en een warmtebehandeling in een zuurstofrijke omgeving, verkrijgt men oppervlakken van een zeer goede kwaliteit. Uit atomaire krachtmikroscopie

metingen is bekend dat deze oppervlakken enkel-getermineerd en op macroscopische lengteschalen atomair vlak zijn. Ter bepaling van de atomaire struktuur zijn verschillende ORD experimenten uitgevoerd. Het resultaat van deze metingen geeft aan dat het oppervlak, in lucht en bij kamertemperatuur, TiO_2-getermineerd is met slechts kleine atomaire verplaatsingen in deze atoomlaag. Bovenop het kristal bevindt zich een extra laag zuurstofatomen. De herkomst van deze zuurstoflaag blijft vooralsnog onzeker. De gebruikte methode ORD kan helaas geen antwoord geven op de vraag of deze zuurstofatomen tot (gesplitste) water molekulen behoren.

In hoofdstuk 4 wordt het ontwerp van een kamer gepresenteerd, die gebruikt wordt voor het in situ bestuderen van het GLD proces met behulp van ORD. De kamer is succesvol getest voor het opwarmen van de wanden bij een interne zuurstofdruk van 1 bar, alsook voor de homoepitaxiale groei van $SrTiO_3$.

In hoofdstuk 5 worden verschillende studies naar de groei van de hoge-T_c supergeleider $YBa_2Cu_3O_{7-x}$ (YBCO) beschreven. Het tijdens de groei volgen van de intensiteit van het punt $(0, 0, \frac{1}{2})$ in de reciproke ruimte van YBCO, resulteert in een oscillerend patroon bestaande uit elkaar afwisselende hogere en lagere intensiteitsmaxima. Elk van deze maxima correspondeert met de voltooiing van een eenheidscellaag YBCO. Het verloop van dit patroon kan kwantitatief worden verklaard door in ogenschouw te nemen, dat in dit punt in de reciproke ruimte, de Röntgenverstrooiingen van twee opeenvolgende eenheidscellagen YBCO elkaar uitdoven. Dit uitgangspunt geeft twee mogelijkheden voor de verstooide Röntgenintensiteit. De verstrooiing van een oneven aantal eenheidscellagen YBCO komt overeen met die van het substraat plus één eenheidscellaag YBCO, terwijl een even aantal lagen resulteert in een verstrooiing gelijk aan die van het onbedekte substraat.

Uit het YBCO fasediagram is reeds bekend dat bij de GLD groeicondities de tetragonale, niet-supergeleidende struktuur stabiel is. Om een orthorhombische, supergeleidende struktuur te verkrijgen, wordt de laag na afloop van de groei afgekoeld in een zuurstofomgeving van 1 bar. De hieropvolgende faseovergang wordt veroorzaakt door zuurstof die het kristal indiffundeert en vervolgens preferentieel een roosterpositie in het *bc*-vlak inneemt. Om een beter inzicht te verkrijgen in deze zuurstofdiffusie en uiteindelijke ordening, zijn verschillende experimenten uitgevoerd waarbij dunne orthorhombische YBCO films verschillende malen zijn opgewarmd bij verschillende partiële zuurstofdrukken. De resultaten van deze experimenten worden beschreven in hoofdstuk 6. Anders dan bij vergelijbare experimenten uitgevoerd met YBCO poeders, vertonen de dunne films drastische strukturele veranderingen bij een

temperatuur van 250°C, ongeacht de zuurstofdruk. Dit kan verklaard worden door aan te nemen dat YBCO zich niet in een stabiele fase bevindt en dat door enigszins te verhitten de zuurstof mobiel wordt in het kristal. Eerdere experimenten uitgevoerd aan éénkristallen, lieten een een aktiveringstemperatuur voor de zuurstofwanorde van ongeveer 100 °C zien. De veronderstelling dat zuurstofmobiliteit belangrijk is voor de waargenomen veranderingen in kristalstruktuur, wordt verder gestaafd door de evolutie van de diffractiepatronen als functie van de tijd. Het is aangetoond dat de breedtes van de diffractiepieken sneller veranderen dan de posities. Aannemende dat de posities gerelateerd zijn aan de totale zuurstofinhoud van het kristal en dat de breedte van de diffractiepiek iets zegt over de ordening van het zuurstof, kan worden geconcludeerd dat zuurstofwanorde plaatsvindt voordat zuurstof het kristal in- of uitdiffundeert. De verklaring kan worden gevonden in een extra diffusiebarrière tussen kristal en vacuum. Dit zou verklaren waarom bij een temperatuur van 250°C, veel lager dan de temperatuur van 650°C van de faseovergang van orthorhombisch naar tetragonaal, drastische veranderingen in de microstruktuur optreden.

In hoofdstuk 7 wordt de afhankelijkheid van de struktuur als functie van de filmdikte bestudeerd. Vanwege het feit dat de celparameters van substraat en film niet gelijk zijn, zal de film zich aanpassen aan het substraat. Dit heeft tot gevolg dat voor zeer dunne films de celparameters in de richting van het grensvlak gelijk zijn aan die van het substraat. Met toenemende filmdikte zal meer en meer spanningsenergie worden opgebouwd in de film, tot op het moment dat het voordeliger wordt om dislokaties in het kristalrooster te vormen. Het punt waar dit gebeurt is de zogenaamde kritische dikte. Films dunner dan de kritische dikte bevinden zich in de pseudomorfe fase. Als een gevolg van ongelijke celparameters a en b in de orthorhombische fase van bulk YBCO, vormt zich een tweelingstruktuur. De bovengrens van de dikte van de psudomorfe fase is bestudeerd door de hoek tussen de verschillende tweelingen te meten als functie van de filmdikte. In de pseudomorfe fase zijn geen tweelingen aanwezig. Films met verschillende dikte zijn gebruikt in de metingen, waarna een kritische dikte van 11.5(6) nm gevonden is, welke zeer goed overeenkomt met waarden in de literatuur. Daarnaast werd gevonden dat na de pseudomorfe fase de celparameters geleidelijk veranderen richting de waarden voor bulk YBCO, met een halfwaardedikte van 23(1) nm. Vergelijking van deze geleidelijke strukturele veranderingen als functie van de dikte met supergeleidende overgangstemperaturen voor dunne YBCO films, leidt tot de conclusie dat de bekende relatie tussen T_c en kristalstruktuur voor bulk YBCO niet opgaat voor dunne films in dit diktebereik.

Hoofdstuk 8 beschrijft een studie naar de grenslaagstruktuur van $SrTiO_3(001)$ bedekt met een fractionele eenheidscellaag $LaAlO_3$ bij hoge temperauur. Recentelijk werd ontdekt dat het grensvlak tussen deze twee isolerende materialen geleidend is. Daarnaast is dit systeem interessant vanuit het oogpunt van de groei van complexe oxides, omdat het extreem stabiel is gedurende een periode lang genoeg om uitgebreide metingen te verrichten. Twee verschillende monsters werden gegroeid, beide bij een temperatuur van 850 °C. Na de groei werd één monster op de depositietemperatuur gehouden waarna verschillende zogenaamde Crystal Truncation Rods (CTRs) gemeten zijn. Het andere monster werd na depositie afgekoeld tot 200°C, waarna verschillende CTRs gemeten zijn. Het resulterende model voor de kristalstruktuur bij 850°C, vertoont atomaire verschuivingen die ongeveer net zo groot zijn als de onzekerheden, zodat het niet mogelijk is uitspraken te doen over de grenslaagstruktuur. De resultaten voor de struktuur bij 200°C, laten wel significante atomaire verschuivingen zien, tot aan 10 % ten opzichte van de ideale posities. Deze atomaire verschuivingen introduceren een grote polarisatie, vergelijkbaar met die in ferro-electrische materialen. De oorsprong van deze roosterverstoring blijft op het moment nog onduidelijk.

Dankwoord

Nu het einde van het promotietraject nadert, is het moment aangebroken om nog eens terug te kijken op deze periode. Hoewel ik eigenhandig elke letter van dit boekje heb getypt, zou de totstandkoming van deze lange reeks letters niet mogelijk geweest zijn zonder de medewerking van velen.

Heinz, jouw bijdrage gaat verder dan alleen de inhoud van dit boekje. Ik zou je willen bedanken voor alles, reikend van de wetenschappelijke begeleiding tot aan het slepen van auto's of het helpen verhuizen. Ik kijk met plezier terug op mijn periode in Grenoble, en dat komt mede door jou.

Sybolt, de experimenten op het ESRF zijn onvergetelijk, en niet alleen wat resultaten betreft. Af en toe leek het qua meligheid een beetje op 'Debiteuren Crediteuren'. Het had weinig gescheeld of we waren om geld gaan gokken of de volgende oscillatie omhoog dan wel omlaag zou gaan en ik ben benieuwd of de term 'laserboys' de Van Dale ooit nog gaat halen. Ook in het 'normale' leven, d.w.z. op de UT, was het prettig samenwerken. Bedankt daarvoor.

Horst wil ik graag bedanken voor het scheppen van de mogelijkheid om binnen LT mijn promotie af te ronden en om als promotor op te treden.

Ook een speciaal woord van dank aan Elias Vlieg. Bij hem heb ik een soort van stage kunnen lopen om de fijne kneepjes van het SXRD-vak in de vingers te krijgen. Daarnaast kon ik altijd aankloppen voor discussie of om zaken nog wat helderder voor de geest te krijgen. Blijkbaar straalde er ook iets van ons PLD project op jou af, want sinds kort ben je er actief bij betrokken als de promotor van mijn opvolger Paul in Grenoble.

Florian, having been your office mate for a few years made me become aware that there is such a thing as the Bavarian culture. Thank you for the nice time we had and if we fail in our careers we can always start a 'Mercedes Werkstatt'. I am sure that we have gathered enough experience over the past years for such a project.

Stan, jij hebt als afstudeerder een zeer belangrijke bijdrage geleverd, zowel aan

de experimenten als het daaropvolgende verwerken van de STO data. Voor ons was de grootste beloning toch wel dat we het idee hadden van een chemicus een fysicus gemaakt te hebben.

Mark, Arjen, Paul en Kurt waren de mede-experimentalisten op menige PLD bundeltijd. Het was niet alleen erg gezellig bij de verschillende runs, maar we hebben ook nog heel belangrijke zaken gedaan, zoals het verkennen van de kroegen in Grenoble. Kurt jij was ook enkele maanden in Grenoble voor een stage, die het begin van de PLD experimenten betekende. Blijkbaar sprak het project je wel aan want nu studeer je op een soortgelijk onderwerp binnen LT af. Ik hoop dat je toch nog wat hebt opgestoken op natuurkundig gebied, en niet alleen maar waar je in Grenoble na tweeën nog naar toe moet.

Je voudrais aussi remercier Florentin et Marie-Ingrid pour leur aide durant les expériences de chauffage des couches minces d'YBCO. Ces expériences n'était pas évident, mais avec votre aide, nous avons réussi à obtenir des résultats.

Bernard et Laurent, votre connaissance et expérience des fours fût énormément importante afin d'assembler et tester la chambre PLD. Grâce à vous, nous avons pu réaliser les expériences sans aucun problème du côté de la chambre.

I have always enjoyed the contact with the staff of ID15: Veijo, Thomas, Marco, Mogens, Anthony and Thierry. The Port hutch is rather isolated from the others, but that was no reason for not having a beer together occasionally. The same accounts for the people from ID11, Larry, Guido and Ann. We all had a good time at the ESRF, but maybe even a better one outside, like at conferences.

Dave en Guus wil ik bedanken voor hun bijdrage aan het project en hun interesse en suggesties.

Het laatse jaar bij LT was ook een zeer plezierige periode. Daarvoor wil ik Joska, Kees, Alexander, Ariando, Dick, Frank, Maarten, Jeroen, Aico, Hans, Karthi, Martin, Johannes, Kristiaan en Harald bedanken. Er was ook uitstekend contact met AMK. Vaak was onze groep samen met Koray, Frank V., Paul, Dekkers en Molag nog te vinden bij borrels terwijl de tap allang dicht was. Dit werd waarschijnlijk veroorzaakt door het blaadje-halen-effect, waar sommigen erg bedreven in waren.

Gerrit wil ik bedanken voor de computerondersteuning die ik heb mogen ontvangen. Ik was erg blij dat ik me nooit zorgen hoefde te maken of alles wel op orde was. Bedankt daar voor. Ook wil ik Miek bedanken voor zijn hulp en suggesties aangaande LaTeXen UNIX.

My stay in Grenoble has been made even better by the company of (Welsh) Dave.

You tried to teach me some of the finest aspects of British culture, such as ManU, English English, ManU, beers and ManU, to name the most important ones. Thanks mate. Later on we even founded our own appartment together with Hanns. It almost became a German 'WG', where the parties were excellent.

I would also like to mention (Scottish) Dave, Isabelle, Julie and Ben for their company, either in their home, whenever there was a dinner party, or for some important football match, like Scotland vs. Holland, in the pub.

Van alle mensen die mij in de loop der jaren zijn komen opzoeken wil ik met name Robin noemen. Jij was eigenlijk de constante factor in het organiseren van korte uitstapjes naar Grenoble voor de jongens. Het is me nog steeds niet duidelijk of ik nu zo'n leuk programma kon aanbieden, of dat je meer geïnteresseerd was in de besneeuwde bergen. Ik wil je ook bedanken voor het feit dat je op wereldreis bent gegaan. Niet omdat je daardoor mijn promotie mist, maar omdat je zo, samen met Germaine in Bolivia, die prachtige foto hebt kunnen maken die de voorkant van dit boekje siert.

Met Diederik en Sido heb ik ook wat mooie en vooral sterke skiverhalen meegemaakt. Ik ben blij dat ik jullie als paranimf heb, zo weten we ook van deze happening een gedenkwaardig moment te maken, waar ongetwijfeld nog vele verhalen de ronde over zullen gaan doen.

Želim se zahvaliti mojim rođacima Nadi i Zoranu, i Ankici, Peru, Slađani i Vedranu što sam uvijek mogao doći preko lijeta da se malo odmorim.

I pogotovo se moram zahvaliti Goranu, Olji i Luki, kod kojih sam se u Stuttgartu osjećao kao kod kuće. Puno hvala. I Luka, svaki dan si pitao:'Šta radiš?' Sada vidiš, napisao sam knjižicu i kad budeš velik moći češ je pročitati.

Ook wil ik Margreet en Gerrit bedanken voor hun gastvrijheid in Olomouc en Boekel.

Ozren heeft zijn bijdrage geleverd door mij in contact te houden met salontafelfilosofie. Als wetenschapper is het belangrijk dat soort kwesties niet uit het oog te verliezen.

Maaike wil ik bedanken voor haar nimmer aflatende steun. Het is al eens gezegd, maar toch nog maar een keer: zonder jou was dit allemaal niet mogelijk geweest.

En tot slot wil ik Paulien bedanken voor alles. Hoewel we nu samen een hectische tijd achter de rug hebben, weet ik zeker dat dit alles een mooie basis vormt voor de toekomst.

Vedran